Chemically Reduced Graphene Oxide for Supercapacitor Applications

A Thesis

Submitted in Partial Fulfillment of the Requirements

for the Degree of

Doctor of Philosophy

by

Plawan Kumar Jha

ID: 20123204

INDIAN INSTITUTE OF SCIENCE EDUCATION AND RESEARCH, PUNE

2018

Dedicated to

My Parents and My Guru Dr. Purushottam Jha

भारतीय विज्ञान शिक्षा एवं अनुसंधान संस्थान, पुणे
INDIAN INSTITUTE OF SCIENCE EDUCATION AND RESEARCH (IISER), PUNE
(An Autonomous Institution, Ministry of Human Resource Development, Govt. of India)

Dr. NIRMALYA BALLAV
Associate Professor (Chemistry)
E-mail: nballav@iiserpune.ac.in
Web: http://www.iiserpune.ac.in/~nballav/

Dr. Homi Bhabha Road, Pashan
Pune 411 008, INDIA
Tel: +91 20 2590 8215
Fax: +91 20 2586 5315

CERTIFICATE

Certified that the work incorporated in the thesis entitled ***"Chemically Reduced Graphene Oxide for Supercapacitor Applications"*** submitted by ***Mr. Plawan Kumar Jha*** was carried out by the candidate, under my supervision. The work presented here or any part of it has not been included in any other thesis submitted previously for the award of any degree or diploma from any other university or institution.

Date: 30th Aug, 2018

Dr. Nirmalya Ballav
(Research Supervisor)

भारतीय विज्ञान शिक्षा एवं अनुसंधान संस्थान, पुणे
INDIAN INSTITUTE OF SCIENCE EDUCATION AND RESEARCH (IISER), PUNE
(An Autonomous Institution, Ministry of Human Resource Development, Govt. of India)

Declaration

I ***Mr. Plawan Kumar Jha*** declare that, this written submission represents my ideas in my own words and where others' ideas have been included; I have adequately cited and referenced the original sources. I also declare that I have adhered to all principles of academic honesty and integrity and have not misrepresented or fabricated or falsified any idea/data/fact/source in my submission. I understand that violation of the above will be cause for disciplinary action by the Institute and can also evoke penal action from the sources which have thus not been properly cited or from whom proper permission has not been taken when needed.

The work reported in this thesis is the original work done by me under the guidance of ***Dr. Nirmalya Ballav.***

Date: 30th Aug, 2018

Mr. Plawan Kumar Jha
(ID: 20123204)

nballav@iiserpune.ac.in Tel: +91 (020) 2590 8215 www.iiserpune.ac.in

Acknowledgment

First and foremost, I would express my deepest gratitude to my research supervisor Dr. Nirmalya Ballav for his continuous support, guidance, encouragements, and teaching me a good conduct of scientific research, not only in the terms of magnitude but also direction. His immense patience, faith, and enthusiasm has always encouraged me in my PhD and personal life to work harder. Although completely different research field or situation, his passion and dedication about research has energized me at every step of my PhD tenure. He has taught me, how to do an organized research and communicate it across the scientific community. I am very fortunate to have been his PhD student. Thank you very much sir for being an excellent mentor.

A sincere acknowledge to Indian Institute of Science Education and Research (IISER), Pune and its former and present directors Prof. K. N. Ganesh and Prof. J. B. Udgaonkar, for maintaining such excellent interdisciplinary research facilities and an outstanding research environment. I am extremely thankful to Chair Chemistry Prof. M. Jayakannan for his support and generosity. I also thank all faculties of IISER Pune.

I am really grateful to my present and former Research Advisory Committee (RAC) members Dr. Sujit K. Ghosh (IISER Pune), Dr. Dr. Pattayil A. Joy (NCL, Pune), and Dr. Amitava Das (CSMCRI, Bhavnagar) for their invaluable suggestions during RAC meetings which really helped me to improve my work. I am thankful to Dr. Sreekumar Kurungot (NCL Pune) and his former student Dr. Santosh K. Singh for giving me the opportunity to access his lab for electrochemical measurements during the initial stage of my PhD. I also thank Dr. Anil. K Debnath (BARC, Mumbai) for XPS measurements and Dr. Suresh Gatla (J & M) for their support through various measurements. I thank Dr. Surjeet Singh and his student Ms. Prachi Telang for providing data on Hall-effect measurements. I am also grateful to Dr. R. K. Sharma (SPEL) for showing high interest in our graphene based materials.

I am thankful to Mr. Mayuresh Kulkarni, Mr. Mahesh Jadhav, Mr. Nitin Dalvi, Mr. Anil Prathamshetti, Mr. Prabhakar Anagare, Mr. Tushar Kurulkar, Mr. Yatish, Mr. Nilesh Dumbre, Mrs. Megha Paygude, Mr. Praveen Nasa, Mr. Ganesh Dimber, Mr. Sandip Kanade for technical and administrative support. I thank Dr. Umeshareddy Kacherki and Ms. Anuradha for library support and Mr. Sachin Behra, Mr. Shailesh Patil and Mr. Abhijeet for IT support.

I am very much thankful to my senior lab mates Dr. Barun and Dr. Rajendra for helping me in my projects and teaching me the instrumentations at the initial stage of my PhD, I really learned many things from them. I am pleased to have my junior lab mates Shammi, Vikash, Kriti, Anupam, Debashree, Ashwini, Pooja, Jay, Gopi, Ishan, Pranay, Manish, and Vaibhav, I really enjoy working with them. A very special thank goes to Shammi, Vikash, and Kriti for their tremendous support and help in my projects. I am also thankful to Dr. Syed (Prof.), I always feel happy talking to him.

I would like to thank our former group members Hetal, Vimlesh, Shraddha, Srikant, Anita, Ateek, Pulak, Utkarsh, Sidhhart, Pranav and Mahendra for their direct/indirect contribution/help.

I am thankful to my friends/other lab mates Biplab Manna, Abhik, Soumya, Rejaul, Shyama, Rajkumar, Amit, Ashok, Anant sir, Sohini, Sneha, Bijoy Da, Soumendra, Ravi, Shishir, Bag, Kunal, Shanku, Kiran, Santosh, Aamod, Partha, Reddy Gaaru, Rakesh, Sandeep, Shiva, Jagadish, Indu, Mullangi, Gopal Anna, Kiran Anna, Alluri and more ….

I would like to thank all my friends without whom personal life, academic, and research could not be delightful and smooth, Malik Mandal, Kailash, Rohit, Govind, Mithoon, Vikash, Sunil, Sanjeet, Arjun, Alok, Nidhi Jha, Sandeep, Meena, Megha, Preeti Jha, Priya, Madhu, Khima, Prity Singh, Reman, Praveen, Veer, Pal, Souvanik, Marawi, Ranjeet, Piyush, Anil, Pashwan, Mrinimoy, Santosh, Mahesh, Bapu, Nilesh, Meghna, Rahul, Subbu, Nanda, Praveen, Dilip, Dinesh, Indrapal, Vartu, Neha, Roby and more….

I take this opportunity to thank madam (Dr. Tanushree Bhattacharjee) and Tani for their encouragement and support.

Now, I want to convey my deepest sense of gratitude and express my utmost feeling to my family members, specially my parents and elder brother whose unconditional trust, support, and struggle encouraged me to overcome extreme difficulties throughout my jagged and gentle pathways. My guru and inspiration, my elder brother shaped me from the scratch and really worked hard along with my parents to push me towards the right direction. I will be extremely delightful if ever I would be able to translate their dreams into reality. I would also like to thank my other family members, my sisters, brother-in-laws, nieces, nephews, sister-in-laws, and uncle Mr. Girija Nand Jha. I owe to Jyotsna didi, a very close family friend, who has given me the name Plawan and also saved my life during a mishap.

I would also like to thank American Chemical Society (ACS), Royal Society of Chemistry (RSC), John Wiley & Sons (Wiley-VCH) and Elsevier for publishing a number of my research articles produced during my PhD tenure at IISER, Pune.

I am thankful to IISER Pune, DAE-BRNS, DST-Nano Mission, DST-SERB, and Infosys for the financial support.

Plawan Kumar Jha

Table of Contents

The thesis entitled ***"Chemically Reduced Graphene Oxide for Supercapacitor Applications"*** includes 5 chapters.

Recent demands on energy storage opened up many challenges and opportunities in the domain of electrochemical devices such as batteries and supercapacitors. Supercapacitors are known for high power supply in short time, long life cycle and eco-friendly operation. Owing to its remarkable properties, graphene (single layer of graphite) – an allotrope of elemental Carbon and a 2D material discovered in 2004 – has emerged as a promising active-electrode material for developing high-performance supercapacitors. However, obtaining single layers of graphene in large scale by bottom-up approach is extremely difficult. Thus, top-down approach whereby graphite is first chemically oxidized to graphene oxide (GO) and subsequently reduced to reduced graphene oxide (rGO) which exhibits physicochemical properties in close resemblance to pristine graphene has emerged.

This thesis aimed at exploring unconventional transition metal salts-based reducing agents in the chemical reduction of GO to rGO and to use rGO as such (without further treatments) in the fabrication of all solid-state supercapacitors. The overall electrochemical performance of our rGO was found to be much superior in comparison to rGO obtained by conventional reducing agents such as $NaBH_4$, and N_2H_4. To further boost the capacitance values of rGO supercapacitor, successful usage of organic electrolytes, metal-ion additives, optimal concentration of gel polymer electrolyte and blending with conducting polymer (namely polyaniline) were demonstrated. Finally, our process of producing rGO by top-down chemical approach in large scale was realized to be highly economic and thereby promising for supercapacitor applications at industrial level.

Chapter 1. ***Introduction to Supercapacitors and Reduced Graphene Oxide***

This chapter consists of general introduction to energy storage devices and their electrode active materials, specifically, supercapacitors and rGO. Electrical double layer models and the formation of same in the graphene based materials during supercapacitive testing, commonly known as electrical double layer capacitors (EDLC), has been extensively discussed. Specific aspects of reduction of GO by conventional and un-conventional reducing agents and their application, such as, electronics and supercapacitor, were covered. Additionally, pseudocapacitors and its associated active materials as well as effect of electrolytes on supercapacitors were concisely discussed.

Chapter 2. ***Reduction of Graphene Oxide by $FeCl_2$/HCl for Supercapacitor Applications***

In this chapter, for the first time, we have explored an un-conventional and mild reducing agent $FeCl_2$/HCl for the one-pot chemical reduction of GO to high quality rGO with optimally balanced physicochemical properties (electrical conductivity ~ 500 S/m and BET surface area ~230 m^2/g), where reducing agent can be recycled. The fabricated all solid-state and flexible supercapacitors of as synthesized rGO (without any further treatment) exhibited remarkable supercapacitive performance. The high specific capacitance values (~170 F/g at 1 A/g), energy/power density, and long durability cycles (>100000 cycles with more than 80% C_S retention) of our rGO supercapacitor was realized to be highest in the domain of rGO materials, synthesized chemically by conventional reducing agents and used as such as an electrode active material. High capacitance value of rGO was attributed to the formation of optimally healed rGO via intramolecular cross-dehydrogenative coupling induced by Fe(III).

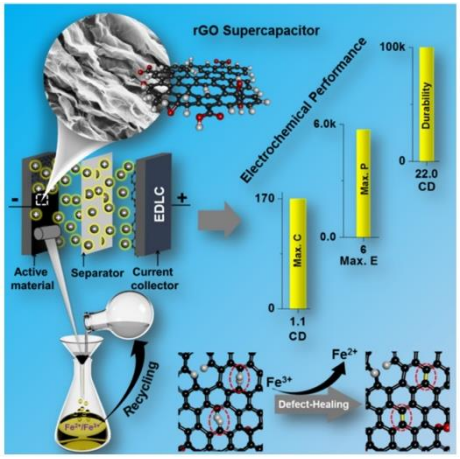

Scheme 1. *Schematic illustration of supercapacitive performance of rGO material and recycling aspect of reducing agent.*

Publication from this chapter

1. High-Level Supercapacitive Performance of Chemically Reduced Graphene Oxide

Plawan Kumar Jha, Santosh Kumar Singh, Vikash Kumar, Shammi Rana, Sreekumar Kurungot, and N. Ballav. *Chem* **2017**, *3*, 846-860.

Chapter 3. *Reduction of Graphene Oxide by $MnCl_2/NH_4OH$ for Supercapacitor Applications*

In this chapter, we have introduced another mild reducing agent $MnCl_2/NH_4OH$ for the wet-chemical reduction of GO to rGO. The supercapacitive performance of rGO in aqueous medium (C_S~265 F/g at 1 A/g) and 10 wt% PVA-H_2SO_4 gel polymer electrolyte (GPE) (C_S~145 F/g at 1 A/g) – a safer and eco-friendly electrolyte, was found to be impressive.

We have also systematically varied the amount of H_2SO_4 in PVA-H_2SO_4 from 5-50 wt% and realised remarkable capacitance value (C_S~310 F/g at 1 A/g) along with high durability cycles (~10000 cycles with 70% C_S retention), at a composition of 20 wt% H_2SO_4 in 10 wt% PVA. The fabricated all solid-state flexible supercapacitor showed high-flexibility and durability.

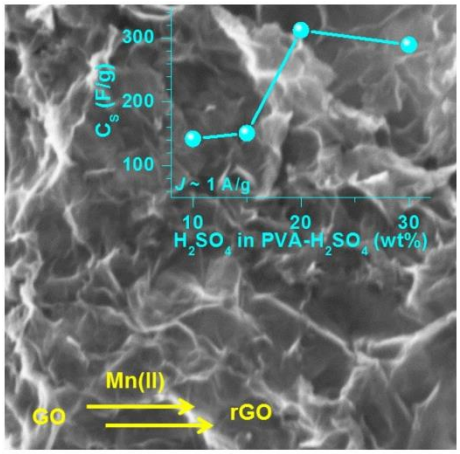

Scheme 2. *Schematic illustration of supercapacitive performance of rGO, produced from chemical reduction of GO by Mn(II).*

Publication from this chapter

1. Graphene-Based Supercapacitors: How Desirable is H_2SO_4 wt% in 10 wt% PVA?

Plawan Kumar Jha, Kriti Gupta, Vikash Kumar, Anil Krishna Debnath, Debashree Roy, Shammi Rana, and Nirmalya Ballav. 2018 (Submitted).

Chapter 4. ***Reduction of Graphene Oxide by CuCl for Supercapacitor Applications***

In this chapter, on the basis of standard electrode potential and thermodynamic stability, we have screened Cu(I)Cl salt – a mild reducing agent for the chemical reduction of GO to rGO. The high surface area (~360 m^2/g) and electrical conductivity (150 S/m) of rGO satisfies the criteria to be a supercapacitive material.

The fabricated all solid-state supercapacitor of rGO in 10 wt% PVA-H_2SO_4 as well as 20 wt% H_2SO_4 in 10 wt% PVA gel polymer electrolyte (GPE) showed remarkably high C_S values to be ~240 F/g and 310 F/g at a current density of 1 A/g, respectively. Sustainability and durability (>100000 cycles with >80% C_S retention) of rGO supercapacitors was realised to be outstanding. After switching the current density from 15→20→15 A/g, C_S retention was found to be 100% in each case.

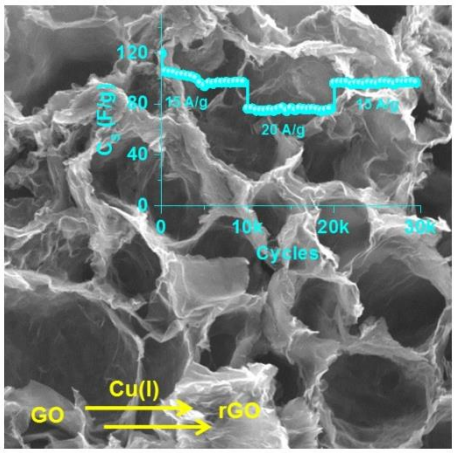

Scheme 3. *Schematic illustration of supercapacitive performance of rGO produced from chemical reduction of GO by Cu(I).*

Publication from this chapter

Supercapacitor of Reduced Graphene Oxide Derived from Chemical Reduction with Cu(I) Salt with Energy Density beyond 10 Wh/g in Aqueous Gel Electrolyte.

Plawan Kumar Jha, Kriti Gupta, Anil Krishna Debnath, Shammi Rana, and Nirmalya Ballav. 2018 (Submitted).

Chapter 5. ***Reduced Graphene Oxide-Polyaniline Nanocomposites for Supercapacitor Applications***

In this chapter, polyaniline salt was prepared through template mediated method and isolated emeraldine salt (ES) was employed as active material for high performance supercapacitor. Further, rGO – an EDLC material and polyaniline (PANI) – a pseudocapacitive material, were blended together in order to enhance the overall supercapacitive performance of rGO-PANI nanocomposites, synergistically. The fabricated all solid-state supercapacitors of acid doped rGO-PANI nanocomposites exhibited interesting capacitive and durability performance.

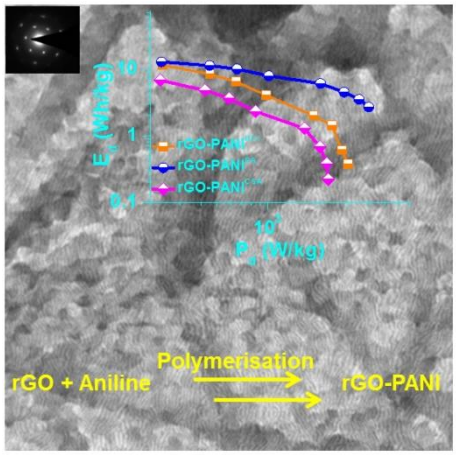

Scheme 4. *Schematic illustration of supercapacitive performance of rGO-PANI nanocomposites.*

Publication from this chapter

1. Nanofibers to Nanocuboids of Polyaniline by Lead Nitrate: Hierarchical Self-Assembly with Lead Ions.

   Plawan Kumar Jha, Barun Dhara, and Nirmalya Ballav.

   RSC Adv. **2014**, *4*, 9851–9855.

2. Pb^{2+}-N Bonding Chemistry: Recycling of Polyaniline−Pb Nanocrystals Waste for Generating High-Performance Supercapacitor Electrodes.

   Plawan Kumar Jha, Santosh Kumar Singh, Suresh Gatla, Olivier Mathon, Sreekumar Kurungot, and Nirmalya Ballav.

   J. Phys. Chem. C **2016**, *120*, 911–918.

3. Hierarchical Nanocomposites of Reduced Graphene Oxide and Polyaniline for Supercapacitor Applications.

   Plawan Kumar Jha, Kriti Gupta, Vikash Kumar, Shammi Rana, and Nirmalya Ballav. 2018 (Submitted).

C	Capacitance
V	Voltage
I	Current
Q	Charge
EDLC	Electrical double layer capacitor
CV	Cyclic voltammetry
CD	Galvanostatic charge-discharge
EIS	Electrochemical impedance spectroscopy
2D	Two dimensional
Γ	Time constant
ʃ	Frequency
J	Current density
Coul. efficiency	Coulombic efficiency
C_S	Specific capacitance
C_G	Gravimetric capacitance
C_A	Areal capacitance
E_d	Energy density
P_d	Power density
Re (Z) or Z’	Real impedance
Im (Z) or Z”	Imaginary impedance
R_S	Equivalent series resistance
R_{CT}	Charge transfer resistance
Ω	Ohm
cc	Cubic centimetre
Gr	Graphite
GO	Graphene Oxide
rGO	Reduced graphene oxide
PVA-H_2SO_4	Polyvinyl alcohol-Sulphuric acid
wt%	Weight percentage
PET	Polyethylene terephthalate
GPE	Gel polymer electrolyte
PANI	Polyaniline

EB	Emeraldine base
ES	Emeraldine salt
HCl	Hydrochloric acid
PA	Phytic acid
CSA	Camphorsulfonic acid
Å	Angstrom
AC	Alternative current
°C	Degree Celsius
AN	Acetonitrile
DC	Direct current
DMSO	Dimethyl sulfoxide
AFM	Atomic force microscopy
EDXS	Energy-dispersive X-ray spectroscopy
UV-vis	Ultraviolet-visible spectroscopy
FESEM	Field emission scanning electron microscopy
FTIR	Fourier transformed infrared-spectroscopy
MeOH	Methanol
PPy	Polypyrrole
PTh	Polythiophene
PXRD	Powder X-Ray diffraction
TGA	Thermogravimetric analysis
TEM	Transmission electron microscopy

A. Publications Included to Thesis

1. High-Level Supercapacitive Performance of Chemically Reduced Graphene Oxide.

   P. K. Jha, S. K. Singh, V. Kumar, S. Rana, S. Kurungot, and N. Ballav.

   Chem **2017**, *3*, 846-860.

2. Graphene-Based Supercapacitors: How Desirable is H_2SO_4 wt% in 10 wt% PVA?

   P. K. Jha, K. Gupta, V. Kumar, A. K. Debnath, D. Roy, S. Rana, and N. Ballav.

   2018 (Submitted).

3. Supercapacitor of Reduced Graphene Oxide Derived from Chemical Reduction with Cu(I) Salt with Energy Density beyond 10 Wh/g in Aqueous Gel Electrolyte.

   P. K. Jha, K. Gupta, A. K. Debnath, S. Rana, and N. Ballav. 2018 (Submitted)

4. Hierarchical Nanocomposites of Reduced Graphene Oxide and Polyaniline for Supercapacitor Applications.

   P. K. Jha, K. Gupta, V. Kumar, D. Roy, and N. Ballav.

   2018 (Submitted).

5. Nanofibers to Nanocuboids of Polyaniline by Lead Nitrate: Hierarchical Self-Assembly with Lead Ions.

   P. K. Jha, B. Dhara, N. Ballav.

   RSC Adv. **2014**, *4*, 9851-9855.

6. Pb^{2+}-N Bonding Chemistry: Recycling of Polyaniline−Pb Nanocrystals Waste for Generating High-Performance Supercapacitor Electrodes.

   P. K. Jha, S. K. Singh, S. Gatla, O. Mathon, S. Kurungot, and N. Ballav.

   J. Phys. Chem. C **2016**, *120*, 911–918

B. Other Publications

1. Thermally-Driven Resistive Switching in Solution Processable Thin Films of Coordination Polymers.

   S. Rana, A. Prasoon, **P. K. Jha**, A. P. Shetti, and N. Ballav.

   J. Phys. Chem. Lett. **2017**, *8*, 5008–5014.

2. Giant Enhancement of Carrier Mobility in Bimetallic Coordination Polymers.

   B. Dhara, V. Kumar, K. Gupta, **P. K. Jha**, and N. Ballav.

   ACS Omega **2017**, *2*, 4488−4493.

3. Diamagnetic Molecules Exhibiting Room-Temperature Ferromagnetism in Supramolecular Aggregates.

   B. Dhara, **P. K. Jha**, K. Gupta, V. K. Bind, and N. Ballav.

   J. Phys. Chem. C **2017**, *121*, 12159-12167. (Equally contributed)

4. Possible Room-Temperature Ferromagnetism in Self-Assembled Ensembles of Paramagnetic and Diamagnetic Molecular Semiconductors.

   B. Dhara, K. Tarafder, **P. K. Jha**, S. N. Panja, S. Nair, P. M. Oppeneer, and N. Ballav.

   J. Phys. Chem. Lett. **2016**, *7*, 4988–4995.

5. Increase in Electrical Conductivity of MOF to Billion-Fold Upon Filling the Nanochannels with Conducting Polymer.

   B. Dhara, S. S. Nagarkar, J. Kumar, V. Kumar, **P. K. Jha**, S. K. Ghosh, S. Nair and N. Ballav.

   J. Phys. Chem. Lett. **2016**, *7*, 2945–2950.

6. Highly Hydrophobic and Chemically Rectifiable Surface-Anchored Metal-Organic Framework Thin-Film Devices.

   S. Rana, R. Rajendra, B. Dhara, **P. K. Jha**, and N. Ballav.

   Adv. Mater. Interfaces **2016**, *3*, 1500738.

7. Redox-Induced Photoluminescence of Metal–Organic Coordination Polymer Gel.

   B. Dhara, P. P. Patra, **P. K. Jha**, S. V. Jadhav, G. V. Pavan Kumar and N. Ballav.

   J. Phys. Chem. C **2014**, *118*, 19287–19293.

Chapter 1

Introduction to Supercapacitors and Reduced Graphene Oxide

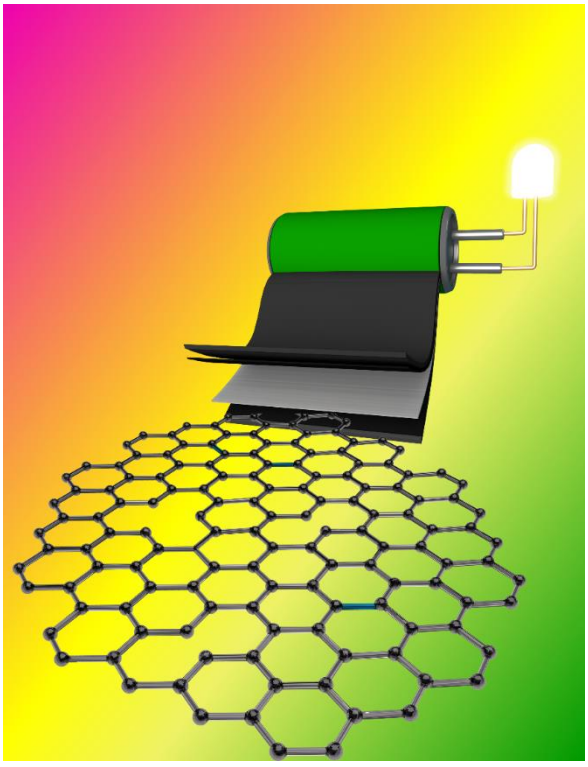

1.1. Introduction

Electrical energy is vital for the mankind[1-3] which depending on the resources and availability can be divided into two major categories: (1) non-renewable sources of energy and (2) renewable sources of energy.[1-5]

The non-renewable sources of energy – coal, petroleum products, hydrocarbon gas/liquids, natural gas, and nuclear energy, are not recyclable, therefore, estimate to be depleted over the time.[1,4-5] Before the stunning discovery of petroleum products, the major source of energy was coal. Since then, due to their immensely high specific energy, both coal and petroleum together supplying the energy worldwide. However, after 1970s, consecutive energy crisis sook the whole community which aroused mainly due to the extensive consumption of petroleum products all over the globe. These energy sources exhale greenhouse gases and impose negative impact on the earth's atmosphere. Thus, the alternative energy sources which could be recyclable and eco-friendly are known as renewable energy. The major renewable sources of energy – solar, wind, geothermal, biomass, hydropower, tidal energy, and others are long-lived and environmental friendly.[1-2,5]

The electricity which is generated from above mentioned energy sources can be supply directly to the giant machine in industries and mandatory equipment in households. However, for mobile objects, such as, transportations, communication devices, and spacecrafts, these energy has to be store and deliver when required, thus energy storage devices are paramount.[1,6-10] The most common and major electrical energy storage devices are capacitors, supercapacitors, batteries, and fuel cells which have different applications based on their mechanism of energy storage and delivery. Ragone plot extracted from energy and power densities of devices (Figure 1.1), evaluates the electrochemical performance of all energy storage devices.[6,11-12] The energy and power densities are parameters ultimately decides the applications of all energy storage devices. On the one end, batteries and fuel cells discharge for longer period of time (thanks to their high energy density), however, low power density limit its application in certain fields (Figure 1.1). On the other end, due to very high power density capacitors are able to deliver the energy very fast, yet the extremely low energy density dismiss the capacitors operation at high energy demanding situations (Figure 1.1).[10]

Supercapacitors bridges the gap between batteries/fuel cells and capacitors – possess high power and energy density at the same time (Figure 1.1).[11]

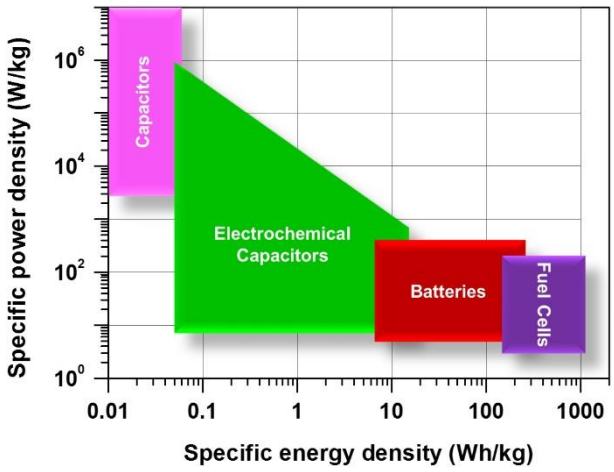

Figure 1.1. *Ragone plot, extracted from energy and power densities of energy storage devices (adopted from ref. 11 © Elsevier).*

1.2. Capacitors

A conventional capacitor is passive electrical device composed of two metal sheets separated by a dielectric material and connected externally by an electrical circuit element. The application of voltage to the capacitor generate electric field between the plates which empower the device to store the energy. Figure 1.2 is the schematic of capacitor which governed by the equation

$$C = {}^{Q}/_{V} \qquad (1)$$

Symbol C is the capacitance of the capacitor (in Farad), Q represents the charge stored on the capacitor (in Coulomb), and V is potential across the capacitor (in Volt).[6,11-13]

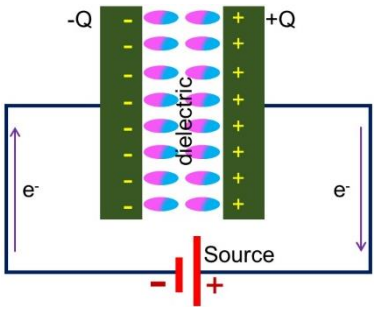

Figure 1.2. *Schematic of conventional capacitor.*

Based on performance and charge storage capability capacitor can be divided into three major categories:[3]

A. Electrostatic capacitor

B. Electrolytic capacitor

C. Electrochemical capacitor or supercapacitor or ultracapacitors.

In short table 1.1 evaluated the electrochemical performance of all three type of capacitors.

Table 1.1. *Electrochemical performance of capacitors.*[6,10]

Capacitors	Electrolytic	Electrostatic	Electrochemical
Charge-Discharge Time (sec)	$\sim 10^{-9}$	$\sim 10^{-4}$	10^{-2} - 10°
Durability (C_S retention >80%)	$\sim 10^{+15}$	$>10^{+10}$	10^{+2} - 10^{+6}
Specific Energy Density (Wh/kg)	$\sim 10^{-3}$	$\sim 10^{-2}$	5 - 40

1.3. Supercapacitor

Supercapacitor can store electrical energy much higher than conventional capacitors.[6] The dedicated research on supercapacitor accelerated after 1957 when Becker filed a U.S patent about the concept of an electrochemical capacitor made by highly porous carbon material and aqueous H_2SO_4 electrolyte solution.[11,14] In 1969, for the first time a Japan based energy company SOHIO commercialised the aqueous capacitor device. The real fame of supercapacitors was realised after 90s where numerous solid as well as liquid state supercapacitors has been developed. Since last decade, supercapacitors flourished in terms of advantageous discoveries of active materials, electrolytes, separators, additives, and current collectors. Such findings craved the industrial sectors to invest enormous amount of resources to establish various supercapacitors. Recently, supercapacitors showed its potentials in almost all electrical and electronic devices/machine, including mobile/stationary objects, cars, cranes, buses, trams, camera, telephones, television, industries etc.[6,8,10-11,15]

Supercapacitor can be generally divided into two categories:[6]

1. Electrical double layer capacitor (EDLC) and

2. Pseudocapacitor.

1.3.1. Electrical double layer capacitor or EDLC [6,13,16]

In 1853, Hermann von Helmholtz (physician) proposed a model about the electrical double layer formation between electrode-electrolyte interface (Figure 1.3a). According to the model once the charged conductive electrode dipped in the electrolytic solution, posed coulombic forces and forms two layers with opposite polarity at the electrode-electrolyte interface which are separated by a distance of molecular order. The stored charge density between the interface can be expressed as:

$$\sigma = \frac{\varepsilon_r\, \varepsilon_o\, V}{d} \; ; \frac{\delta\sigma}{\delta V} = C_d = \frac{\varepsilon_r\, \varepsilon_o}{d} \qquad (2)$$

Where, ε_r, ε_o, V, and *d* are the dielectric constant of medium, permittivity of free space, voltage drop across interface, and thickness of the double layer, respectively. In equation 2, C_d realised to be constant which is not the actuality. It has been observed that for a fixed potential, capacitance varies directly to the concentration of the electrolyte, therefore, for greater accuracy and understanding more refined model was required. After more than 50 years, Luois Georges Gouy (physicist; 1910) and David Leonard Chapman (physical chemist; 1913) modified the Helmholtz model where they have considered the diffuse layer of charges in the solution. Independently, Gouy and Chapman explored and involved the diffuse layer of electrolyte into account and derived various equations related to the potential in the diffuse layer and capacitance dependency on concentration and potential (Figure 1.3b). However, the model overestimated the capacitance value at electrode-electrolyte interface, due to the unconsidered finite ionic sizes of the electrolyte. In 1924, Otto Stern (physicist) combined Helmholtz and Gouy-Chapman model which considered compact layer also called Stern layer/Helmholtz layer and diffuse layer. The ions in electrolyte are solvated, therefore, could not approach the electrode surface closer than the ionic radius of the solvated system. At relatively higher concentration of the electrolyte the hydrated ions are more tightly compressed near to electrode surface and whole system resembles the Helmholtz model. On the basis of adsorbed ionic species (solvent or solvated ions) on the electrode surface the compact layers are divided into inner Helmholtz plane (IHP) and outer Helmholtz plane (OHP). The diffuse layer extends from OHP to the bulk electrolyte solution (Figure 1.3c).

Overall, the expression for electrical double layer capacitance (C_{dl}) can be realised into two individual capacitance, the compact double layer capacitance where charges held at OHP that is C_H and the diffuse region capacitance that is C_D. Both independent capacitors are appears to be connected in series, therefore equation can be written as:

$$\frac{1}{C_{dl}} = \frac{1}{C_H} + \frac{1}{C_D} \qquad (3)$$

The C_H is independent of potential whereas C_D varies with potential. For higher electrolyte concentration or higher polarization, the value of C_D become so large that it do not contribute to the overall capacitance, C_{dl}, thus only C_H contribution can be considered. Even though Stern model which is also known as Gouy-Chapman-Stern (GCS) model is most accepted, but there are still some pitfalls.[13]

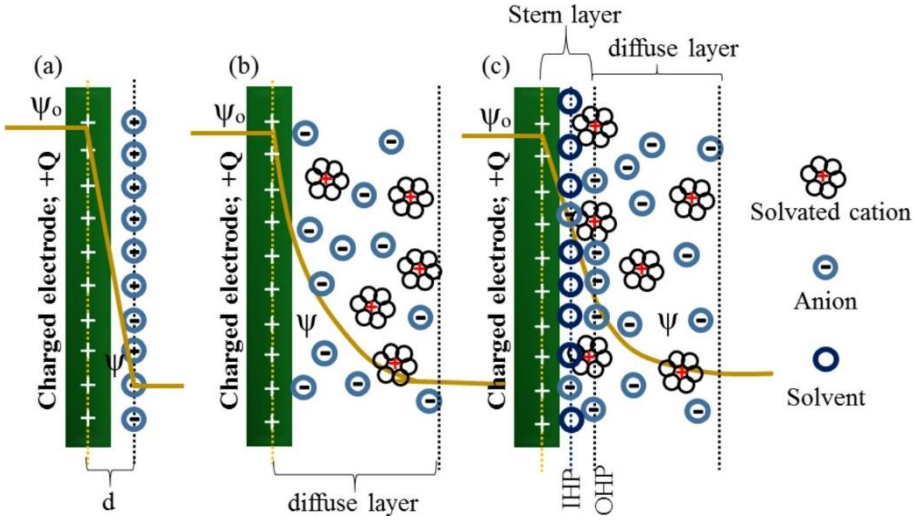

Figure 1.3. *Schematic model of electrical double layer at the charged electrode (a) the Helmholtz model, d is the double layer distance explained in Helmholtz model, (b) the Gouy-Chapman model, show diffuse layer, and (c) the Stern/GCS model. The GCS model show inner Helmholtz plane (IHP) and outer Helmholtz plane (OHP). The ψ_o and ψ_j are the potentials at the active electrode surface and the electrode-electrolyte interface, respectively (adopted from ref. 16 © Royal Society of Chemistry).*

The C_{dl} depend on numerous factors, such as, potential window, types of electrode active materials, electrolytes and associate ions, solvents, chemical affinity between the adsorbed ions and the active electrode surface.[6,11]

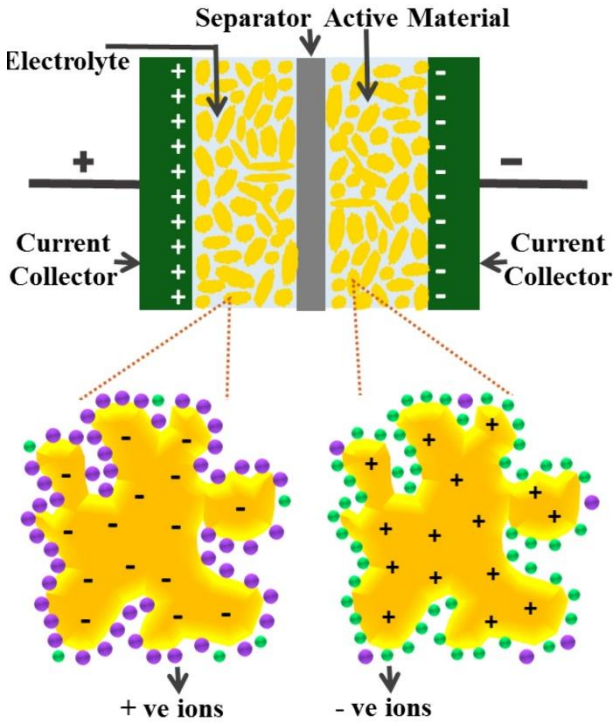

Figure 1.4. *Schematic presentation of an EDLC based on porous carbon electrode materials (adopted from 11 © Elsevier).*

In this thesis, we have tried to shed new light into the development of active materials for electrode, i.e. reduced graphene oxide (rGO) which exhibits EDL characteristic (Figure 1.4) and varied the composition in Gel polymer electrolyte (GPE), and blended rGO with conducting polymer (PANI) – a pseudocapacitive material, for supercapacitor applications.

1.4. Graphene, Graphene Oxide (GO), and Reduced Graphene Oxide (rGO)

The year 2004, witnessed the discovery of first two dimensional (2D) crystal, graphene – an allotrope of elemental carbon, made of a sp^2-bonded infinite extended 2D network.[17] Sir Andre Konstantin Geim (physicist) and Sir Konstantin Sergeevich Novoselov (physicist) together thought simple but yet potent approach to exfoliate single layer of HOPG (HOPG- highly oriented pyrolytic graphite) by ordinary scotch tape.[18] Since then graphene captivated entire scientific and technological province due to its extraordinary properties – high surface area, high carrier mobility, high thermal conductivity, high young modulus, high optical transmittance and others.[19] Finding of such distinguished material was recognized in terms of Nobel Prize in physics in 2010. Thus graphene become called as an origin of all graphitic forms – graphite, carbon nanotubes, and buckyballas (Figure 1.5).[17]

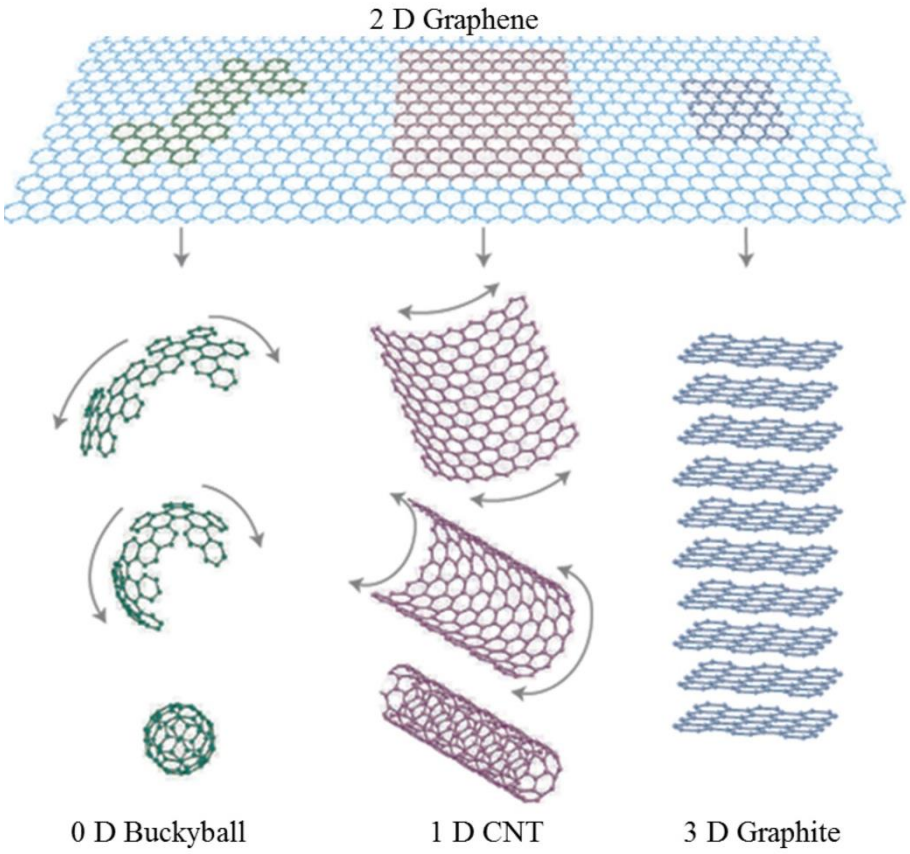

Figure 1.5. *Schematic presentation of graphene family (adopted from ref. 16 © Nature Publishing Group).*

Amongst numerous applications of graphene based materials – photovoltaics, gas storage, sensors, biomedical, light-emitting diodes (LEDs), batteries, supercapacitors, etc., energy conversion and storage becomes most appreciated and explored.[19-28] For instance, with single layer of graphene in principle specific capacitance can be achieved as high as ~21 mF/cm^2 and ~550 F/g (theoretically set) along with high energy density, high power density, and long-term stability.[29] Though talent of graphene pave the way towards developments of modern energy storage devices, the cost effective top-down or bottom-up production either by ordinary scotch tape or by other physical techniques, such as, chemical vapour deposition (CVD) restricted the practical application at industrial scale. Since two decade scientists have design plethora of process to synthesise graphene at larger scale, where top down approach includes – chemical oxidation and reduction, is easy and utmost accepted.[30-32] Impressively, from the mentioned method, rGO can be synthesised in large scale. The physicochemical properties of thin and highly reduced GO closely resembles graphene in terms of conductivity, porosity, stability, and others which are foremost criteria for any active materials to be supercapacitors.[30]

Figure 1.6. *Schematic of oxidation of Gr to GO and simultaneous reduction of GO to rGO (please note that schematic is only for the understanding the different functionality in Gr, GO, rGO; e.g. Gr is not a single but multilayers of graphene).*

Although chemical oxidation of natural graphite in different oxidizing condition has been attempted since 1850s, a successful and widely accepted chemical oxidation of graphite was established in 1958 by William S. Hummers and Richard E. Offeman.[30,33] Eventually, scientists have modified the Hummer's method according to the convenience and requirements of oxidation extent on single to few layers graphite sheets.[34-35]

The oxidation of graphite (first step) import plenty of oxygenated groups – -COOH, -CHO, -C-O-C-, -C=O, and -C-OH, on the carbon networks, convert around 50% sp^2 carbon into sp^3 carbon domain. Due to strong repulsion between the oxygenated groups, graphite sheets exfoliate into single to few layers. However, the sp^3 carbon highly disrupt the π-conjugation in the network, thus GO unable to facilitate the electron across the 2D sheets and behave as an insulator (Figure 1.6). In order to obtain single to few layers graphene network, next chemically smart step is the reduction of GO by appropriate reducing agent (second step) and removal of maximal number of oxygenated group (Figure 1.6). The reduction of GO controls all physicochemical properties of rGO, therefore, second step realised to be the decisive step. There are numerous reducing agents which were employed for the reduction of GO and can be categorised into two parts: (A) conventional reducing agents and (B) unconventional reducing agents. Conventional reducing agents such as, for example, hydrazine (N_2H_4), sodium borohydride ($NaBH_4$), ascorbic acid, hydroiodic acid (HI), and others are widely renowned among organic chemist with the well-established reducing mechanism. On the other hand unconventional reducing agents, such as, metal-acid (Sn/HCl, Fe/HCl, Zn/HCl), metal-alkaline (Zn-ammonia solution), amino acids, plant extracts, hormones, microorganisms, protein, and others are explored for the successful reduction of GO.[30] However, their mechanism is not clearly known, therefore, different groups have given proposed mechanism for the same.

Beside such chemical reducing agents, rGO can also be produced by, thermal method, microwave, ultraviolet-assisted methods, laser scribing techniques of GO and electrochemical exfoliation of graphite.[36-41]

A decade ago, large scale rGO was produced by the chemical reduction of GO in presence of hydroquinone (HQ).[42] GO also have treated with various concentration of $NaBH_4$ to obtain a conducting rGO material which was realised to be superior candidate for practical electronic applications.[43] In 2010, a novel and efficient reducing system HI–Acetic acid was reported for one-pot chemical reduction of GO to a high quality solution-phased rGO powder and vapour-phased rGO paper/thin film. The rGO showed extremely high conductivity thus claimed to be a novel materials for the flexible devices (Figure 1.7).[44]

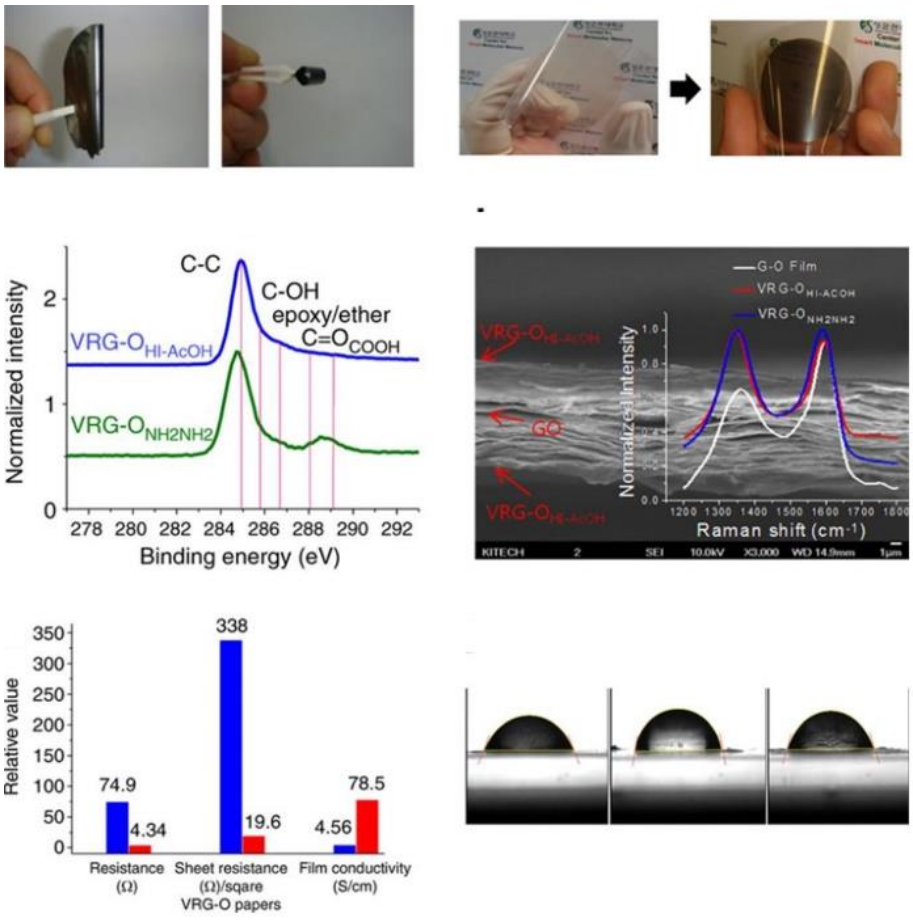

Figure 1.7. *Optical Photographs and graphs corresponding to Chemical reduction of GO to rGO and VrGO by HI-AcOH and their electrical conductivity analysis (adopted from ref. 44 © Nature Publishing Group).*

Conventional reducing agent, N_2H_4 was mostly used to obtain a high conducting rGO material.[45-46] The GO was vaporised with dimethylhydrazine and subsequently annealed the material and administered the rGO for thin-film transistors (TFT) device.[47] A water soluble graphene was produced by treating the GO consecutively with N_2H_4 and $NaBH_4$ which was realised to be highly conducting.[48] Later high electrical conducting water soluble graphene was synthesized by the reduction of GO with N_2H_4 and N_2H_4/NH_3 solution and asserted the valuable application of electronic applications such as field-effect transistors (Figure 1.8).[49]

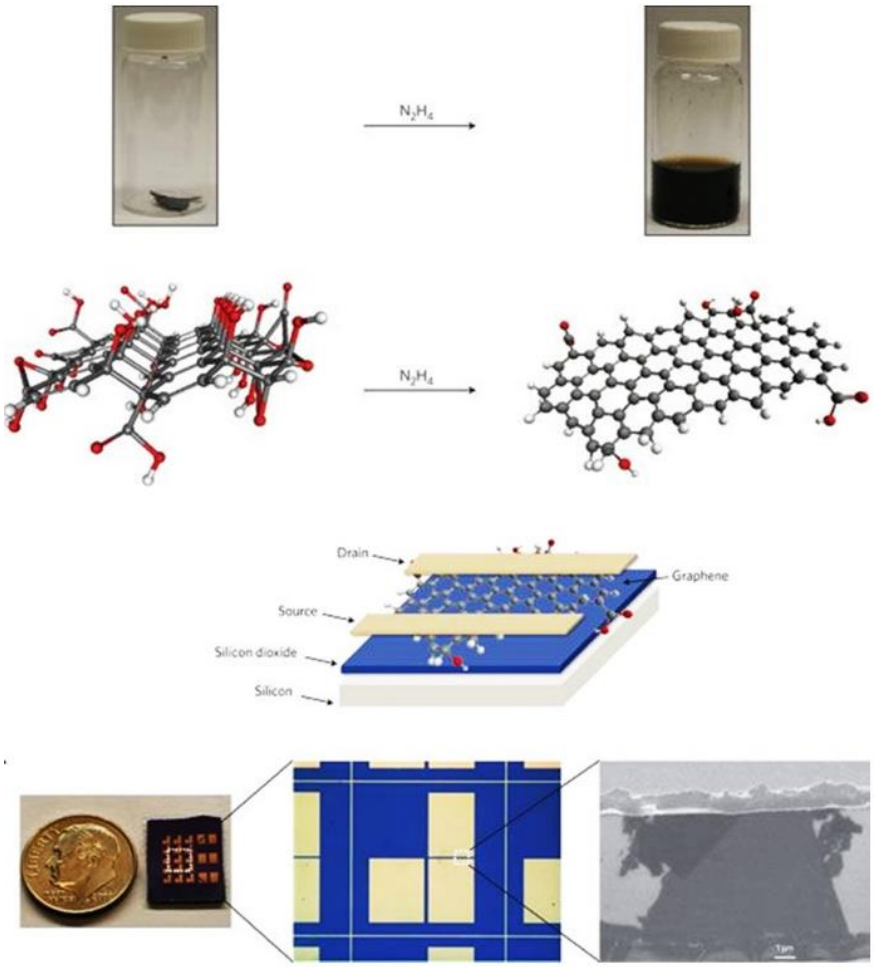

Figure 1.8. *Optical photographs and schematic of chemical reduction of GO to rGO by N_2H_4 for TFT application (adopted from ref. 49 © Nature Publishing Group).*

Eventually, to achieve large scale production of rGO, Fe-HCl reducing agent was employed (Figure 1.9).[50] Calcination of a mixture of Glucose and Fe(III) could produced high quality graphene.[51] The GO can also be successfully reduce by thiourea dioxide and substituted borohydrides – sodium borohydride, sodium cyanoborohydride, and sodium triacetoxyborohydrid.[52-54] There are numerous methods/reports of electrically conducting rGO with rich electronic properties.

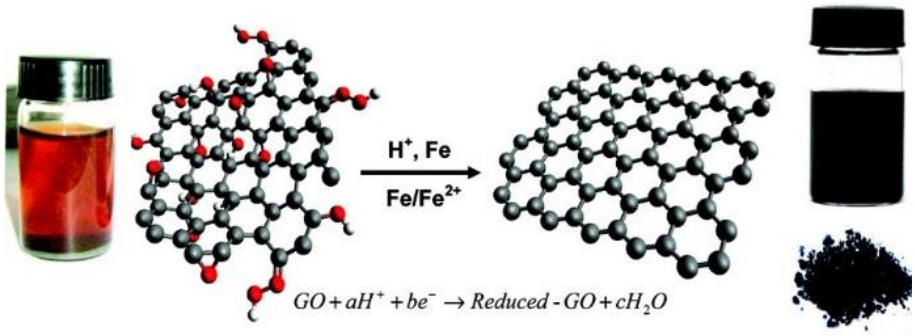

Figure 1.9. *Schematic presentation and optical photographs of chemical reduction of GO to rGO by Fe (powder)/H^+ (adopted from ref. 50 © American Chemical Society).*

Extensive varieties of reducing agents and ways of rGO production, certainly accelerated and lead the energy domains towards state-of-the-art technology, specifically, supercapacitors. However, there are several criteria for materials to be supercapacitors – accessible surface area to the ions of the electrolyte (porosity), electrical conductivity, presence of heteroatoms, defects, surface functional groups, texture of the materials, presence of redox ion species, low cost, and environment friendly nature. Each material must possess more than one of these criteria before trial for supercapacitor applications.[6,11] Conceptually, supercapacitors can store relatively higher amount of charge in small device which is only possible when intrinsic specific surface area of materials is optimally high (Figure 1.4).[11,16] The active ingredient for charge storage in commercial supercapacitors is activated carbon which is generally made by precursors, such as, coconut shells, wood, pitch/coal, polymers – grant high surface area and high electrical conductivity at the same time, therefore, exhibits EDLC around 100-120 F/g in organic electrolyte and can maintain 150-300 F/g in aqueous electrolytes.[6] However, average activated carbon particles shows microporosity (<2 nm pore size), mesoporosity (2‑50 nm) and macroporosity (>50 nm) altogether was realised to be disadvantage for a system, due to the restricted percolation of solvated ion of electrolyte into the very small channels.[6] On the other hand, rGOs could beat activated carbon in terms of charge storage, stability and electrical

conductivity. Besides, rGO sheets bear/could bear all the possible functional groups, can be doped with several hetero atoms, self-assembled in diverse morphology, thus, ultimately satisfies the criteria of high performance supercapacitors.[55]

Since a decade, scientists are synthesising rGO upon varying the reducing agents, as an active material for the supercapacitors application. A molten halide salt (Li in molten LiCl-KCl) at higher temperature can produce corrugated rGO with specific capacitance value to be around 203 F/g, however, performed only 2000 cycles (~97% capacitance retention).[56] A novel strategy of designing nano-architectures based on porous graphene frameworks (PGFs) via in situ covalent functionalization of reduced graphene oxide (rGO, reduced by $NaBH_4$) able to delivered 184 F/g capacitance value with ~97% capacitance retention after 5000 cycles.[57] Intercalated mesoporous carbon spheres between rGO (reduced by N_2H_4) sheets showed ~41 F/g capacitance value which was further thermally treated at 800 °C delivered ~29 F/g capacitance value with 94% capacitance preservation after 1000 cycles.[58] Reducing (by vitamin C) and depositing graphene hydrogel on Ni foam delivered ~ 45.6 mF/cm^2 capacitance value and after 10000 cycles capacitance retention was observed to be ~90%.[59] Despite such tremendous progress of chemically reduced GO based supercapacitors, the overall performance is not at par to the industrial applications, thus, revolved the scientific community to the other direction in terms of exploring techniques/method for high capacitive rGO materials.

Recently, simultaneous reduction and freeze drying method evolved dramatically for the synthesis of highly porous rGO materials. This method involved two-step process of reduction of GO to rGO gel and freeze drying of rGO gel to rGO with highly porous 3D morphology (Figure 1.10).[29] Sophisticated and highly effective laser scribing technique invented to make high performing binder free, mechanically robust, high electrically conducting, and porous graphene (LSG) supercapacitors, which quickly gained its fame for producing the high performance graphene supercapacitors (Figure 1.11).[36]

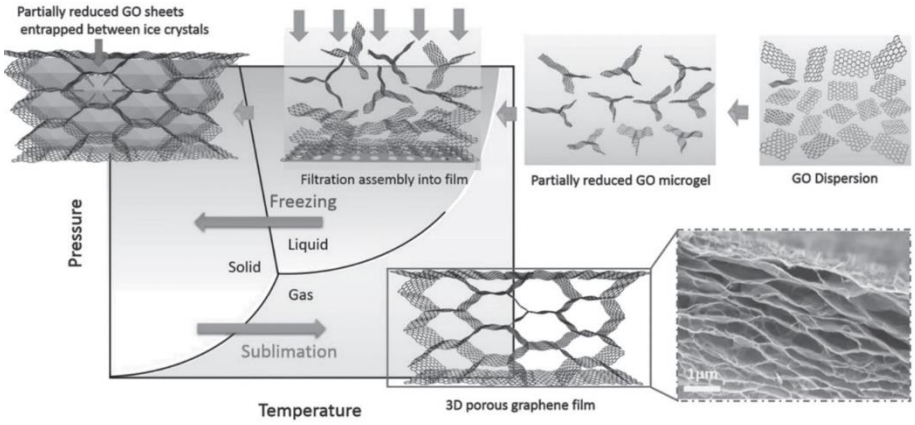

Figure 1.10. *Schematic presentation of freeze drying process of chemically reduced GO (adopted from ref. 29 © John Wiley & Sons, Inc.).*

Though application of all the approaches and techniques towards rGO production is viable, there are always some lacunae which worth to mention and pad to the further development process, that is, the low-cost mass production of rGO is still a major challenge.

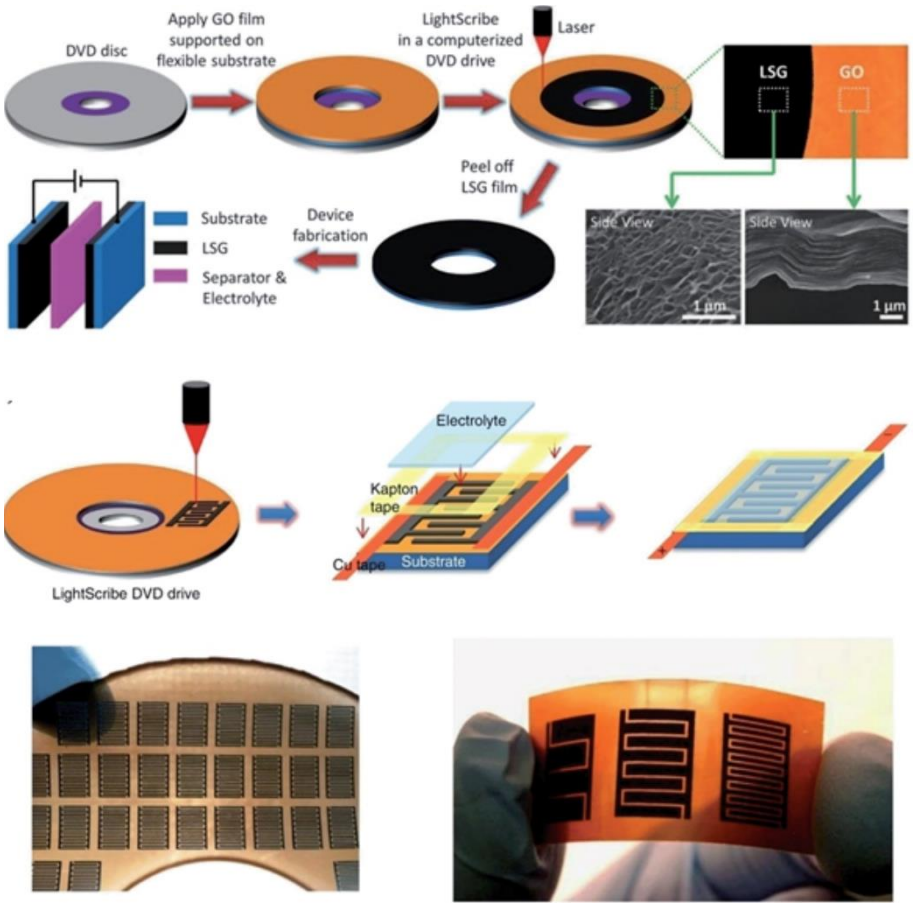

Figure 1.11. *Schematic presentation of the fabrication of LSG (adopted from ref. 36 © Science).*

1.3.2. Pseudocapacitor

Unlike EDLC, in pseudocapacitors, charge storage occurs due to Faradaic reaction at the electrode-electrolyte interface and the extents of delivered charge are a function of applied potential across the device. It is a fact that the materials with EDLC characteristics exhibits 1-5% of their capacitance as pseudocapacitance and on the other hand the pseudocapacitors also store 5-10% of its charges through EDLC.[6] The population of pseudocapacitive materials are vast, specifically – transition metal oxides, such as, RuO_2, Fe_2O_3, Mn_3O_4, CuO, Co_3O_4, and others and conducting polymers, such as, polyaniline, polypyrrole, poly(3,4-ethylenedioxythiophene) (PEDOT), and others.[6,11] Among conducting polymers, polyaniline (PANI) gained enormous attention due to its multiple redox forms (Figure 1.12) and highest theoretical pseudocapacitance value of ~2000 F/g. PANI based supercapacitors ruling since decades and scientists are trying to improve the overall capacitance performance – high capacitance and high stability. However, PANI supercapacitors, without any special treatments such as, for example, appropriate electrolytes and composites with carbon materials, were realised to be collapsed.[60-61]

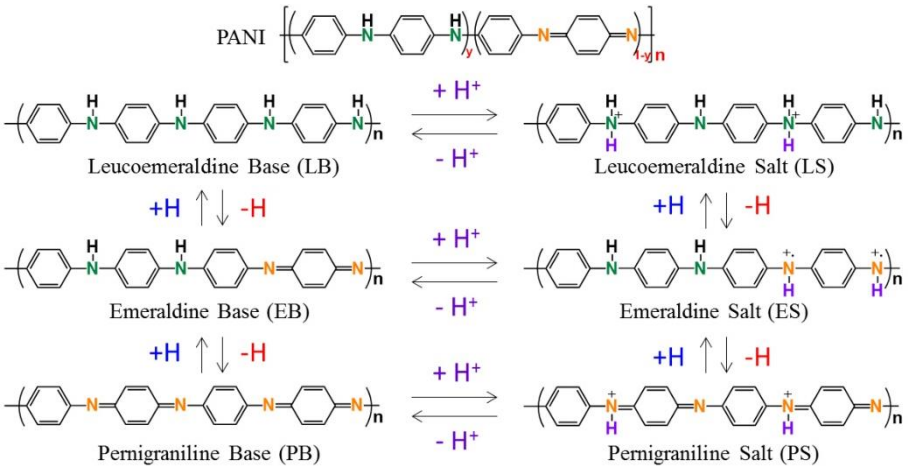

Figure 1.12. *Schematic presentation of all redox forms of polyaniline.*

1.5. Electrolytes

High energy and power densities of a supercapacitor is very much depends on the application of different electrolytes. Different variety of electrolytes as flow chart is depicted in Figure 1.13.[11,62] In order to enhance the performance of devices, scientists have employed various electrolytes formed mainly in aqueous or organic solvents. Due to the stability/instability of solvent within operating potential window and nature of the solvents, the capacitance could immensely varies for system to system. For example, aqueous based electrolyte systems operate below 1.3 V (thermodynamically water splits into O_2 and H_2 at 1.23 V), organic electrolyte operates around 2-3 V window, and ionic liquids (ILs) generally have potential window of 3-4 V. Besides electrolyte properties, matching ionic size of electrolyte to the pore of the active materials, and potential sustainability of active materials also plays an important role in deciding the overall performance within operating potential window. Unlike metal oxides and conducting polymers, carbon based material could sustain wide potential window.[6,12-13,47]

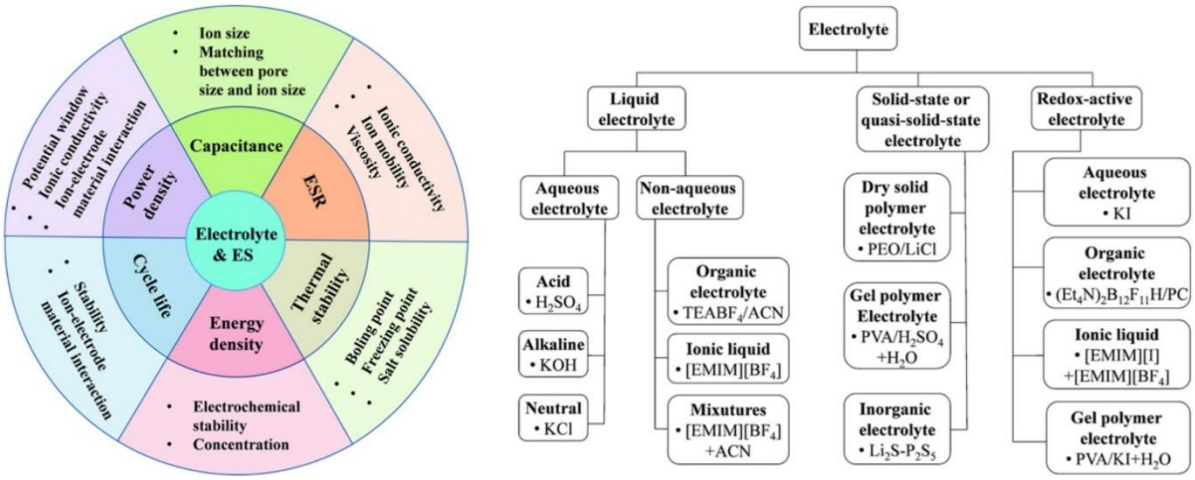

Figure 1.13. *Effect and classification of electrolytes for supercapacitors (adopted from ref. 62 © Royale Society of Chemistry).*

In this thesis, we have primarily focused on poly(vinylalcohol)-sulphuric acid (PVA-H_2SO_4) gel polymer electrolyte (GPE) where PVA act as a polymer host matrix and H^+ and SO_4^{2-} are solvated ions involved for electrochemical activities such as, EDL formation or Faradaic reaction. PVA-H_2SO_4 GPE is a subclass of solid state/quasi solid state electrolyte prepared in aqueous medium.

Due to the high cost and eco-unfriendly nature of organic based electrolyte, aqueous electrolytes are most explored (>80% particularly in the year 2014). Unlike organic or ionic liquids, GPEs are abundant, inexpensive, user friendly, and stable at ambient conditions.[62]

1.6. Final strategy for improving capacitance, energy density, power density, and durability of supercapacitors can be present in terms of flow chart (Figure 1.14).[63]

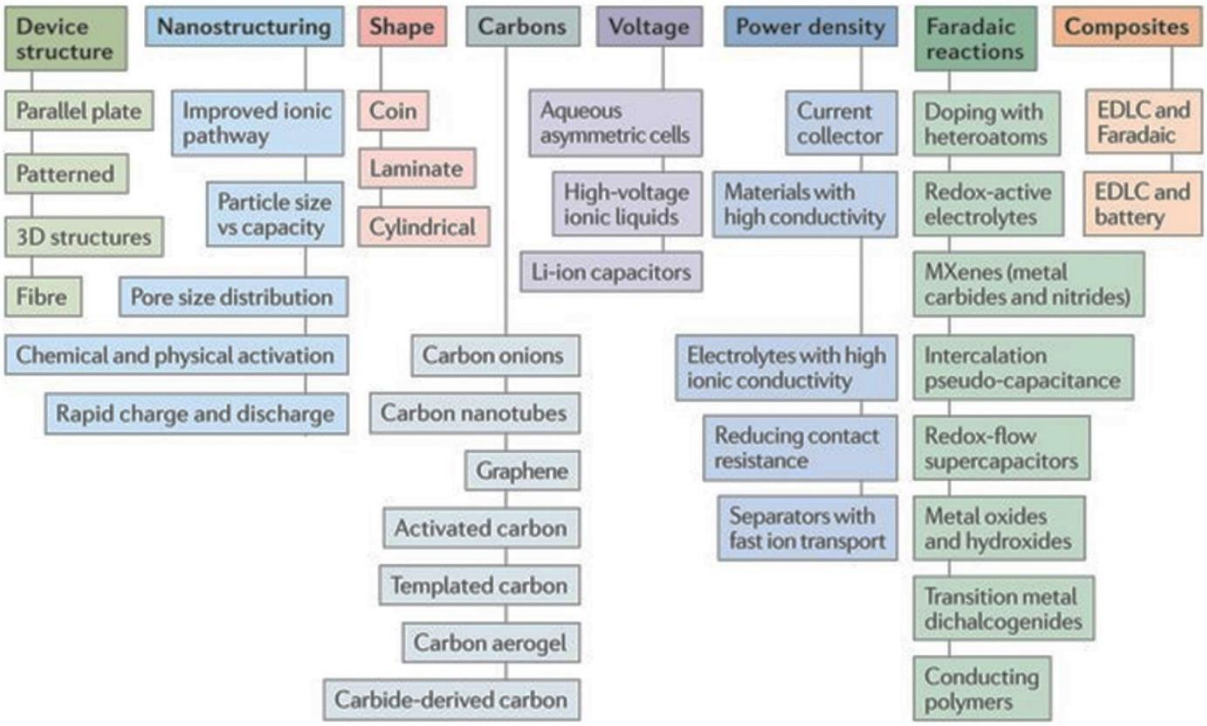

Figure 1.14. *Flow chart of strategy of improving overall capacitance performance (adopted from ref. 63 © Nature Publishing Group).*

1.7. Electrochemical Workstation and Techniques

In this thesis, all electrochemical characterisation of electroactive systems were completed through cyclic voltammetry (CV), galvanostatic charge-discharge (CD), and ac electrochemical impedance spectroscopy (EIS) techniques, partly, in BioLogic potentiostat (model A VMP-3) and PARSTAT MC, galvanostat/potentiostat PMC-2000 (Figure 1.15).

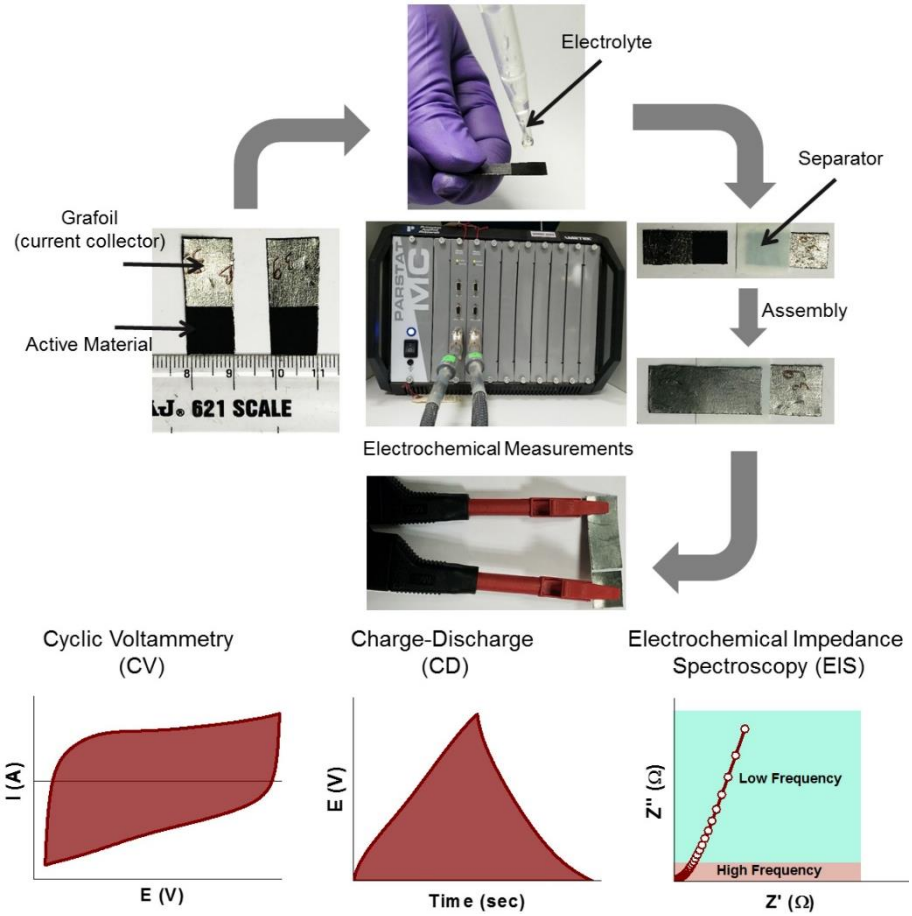

Figure 1.15. *Systematic optical photographs of all solid-state supercapacitors fabrication and the measurement techniques (CV, CD, and EIS).*

1.8. Specific capacitance, energy density (E_d) and power density (P_d) of all materials were calculated employing the following formulae

From CV, equation is,

$$C = \frac{\int_{V1}^{V2} I\,(V)\,dV}{V * \frac{dv}{dt}}$$

$$C_A = 2 * \frac{C}{A};\ C_G = 2 * \frac{C}{M}$$

Where,

$C_S = C_A$ and C_G → Areal and gravimetric capacitance (also called as specific capacitance) of electrode active material.

$\int_{V1}^{V2} I\,(V)\,dV$ → Average current from anodic or cathodic sweep extracted from CV.

V → potential window (in volt).

A → active area per electrode (in cm^2).

M → active mass per electrode (in gram).

$\frac{dv}{dt}$ → scan rate (mV/s).

From CD, equation is,

$$C = \frac{I_{discharge}}{\frac{dV}{dt}}$$

$$C_A = 2 * \frac{C}{A};\ C_G = 2 * \frac{C}{M}$$

Where,

$I_{discharge}$ → discharge current (in mA).

$dV/_{dt}$ → slope of the discharge curve excluding the voltage (IR) drop (in V/sec).

A → active area per electrode (in cm^2).

M → active mass per electrode (in gram).

Energy density (E_d) and power density (P_d) calculation,

$$\text{Gravimetric energy density } (E_{d,G}) = \frac{1}{8} * C_G * V^2 * \frac{1000}{3600}$$

$$\text{Areal energy density } (E_{d,A}) = \frac{1}{4} * C_A * V^2 * \frac{1}{3600}$$

$$\text{Areal power density } (P_{d,A}) = \frac{E_{d,A}}{t_{discharge}} * 3600$$

$$\text{Gravimetric power density } (P_{d,G}) = \frac{E_{d,G}}{t_{discharge}} * 3600$$

V → Potential window = V - V_{IR} (in volt)

$t_{discharge}$ → discharge time, excluding voltage (IR) drop.

1.9. References

(1) Chu, S.; Majumdar, A. Opportunities and Challenges for a Sustainable Energy Future. *Nature* **2012**, *488*, 294.

(2) Birol, F. Key World Energy Statistics. *Intenational Energy Agency* **2017**, p. 97.

(3) Yadav, S. K.; Mishra, G. C. Renewable Energy Potential in India. *International J. Eng. Res. Technol.* **2013**, *6*, 709-716.

(4) Ellabban, O.; Abu-Rub, H.; Blaabjerg, F. Renewable Energy Resources: Current Status, Future Prospects and Their Enabling Technology. *Renewable Sustainable Energy Rev.* **2014**, *39*, 748-764.

(5) Renewable Energy: Into the Mainstream. *International Energy Agency* **2002**, p. 54.

(6) Conway, B. E. *Electrochemical Supercapacitors: Scientific Fundamentals and Technological Applications*. Kluwer Academic/Plenum,: New York, USA, 1999; p p. 366.

(7) Gogotsi, Y.; Simon, P. True Performance Metrics in Electrochemical Energy Storage. *Science* **2011**, *334*, 917-918.

(8) Simon, P.; Gogotsi, Y.; Dunn, B. Where Do Batteries End and Supercapacitors Begin? *Science* **2014**, *343*, 1210-1211.

(9) Burke, A.; Zhao, H. In *Applications of Supercapacitors in Electric and Hybrid Vehicles*, 2015.

(10) Miller, J. R.; Burke, A. F. Electrochemical Capacitors: Challenges and Opportunities for Real-World Applications. *Electrochem. Soc. Interface* **2008**, *17*, 53.

(11) Kötz, R.; Carlen, M. Principles and Applications of Electrochemical Capacitors. *Electrochim. Acta* **2000**, *45*, 2483-2498.

(12) Simon, P.; Gogotsi, Y. Materials for Electrochemical Capacitors. *Nat. Mater.* **2008**, *7*, 845-854.

(13) Bard, A. J., Faulkner, Larry R. *Electrochemical Methods: Fundamentals and Applications*. Wiley: New York, 1980.

(14) H. E. Becker, Low Voltage Electrolytic Capactor U.S. Patent 2 800 616 (1957).

(15) Service, R. F. New 'Supercapacitor' Promises to Pack More Electrical Punch. *Science* **2006**, *313*, 902-902.

(16) Zhang, L. L.; Zhao, X. Carbon-Based Materials as Supercapacitor Electrodes. *Chem. Soc. Rev.* **2009**, *38*, 2520-2531.

(17) Geim, A. K.; Novoselov, K. S. The Rise of Graphene. *Nature materials* **2007**, *6*, 183.

(18) Novoselov, K. S.; Geim, A. K.; Morozov, S. V.; Jiang, D.; Zhang, Y.; Dubonos, S. V.; Grigorieva, I. V.; Firsov, A. A. Electric Field Effect in Atomically Thin Carbon Films. *Science* **2004**, *306*, 666-669.

(19) Ferrari, A. C.; Bonaccorso, F.; Fal'ko, V.; Novoselov, K. S.; Roche, S.; Bøggild, P.; Borini, S.; Koppens, F. H. L.; Palermo, V.; Pugno, N., *et al.* Science and Technology Roadmap for Graphene, Related Two-Dimensional Crystals, and Hybrid Systems. *Nanoscale* **2015**, *7*, 4598-4810.

(20) Bo, Z.; Mao, S.; Han, Z. J.; Cen, K.; Chen, J.; Ostrikov, K. K. Emerging Energy and Environmental Applications of Vertically-Oriented Graphenes. *Chem. Soc. Rev.* **2015**, *44*, 2108-21.

(21) Chen, K.; Song, S.; Liu, F.; Xue, D. Structural Design of Graphene for Use in Electrochemical Energy Storage Devices. *Chem. Soc. Rev.* **2015**, *44*, 6230-57.

(22) Shao, Y.; El-Kady, M. F.; Wang, L. J.; Zhang, Q.; Li, Y.; Wang, H.; Mousavi, M. F.; Kaner, R. B. Graphene-Based Materials for Flexible Supercapacitors. *Chem. Soc. Rev.* **2015**, *44*, 3639-65.

(23) Yang, H. Graphene-Based Supercapacitors for Energy Storage Applications. The Ohio State University, 2013.

(24) Liu, C.; Li, F.; Ma, L. P.; Cheng, H. M. Advanced Materials for Energy Storage. *Adv. Mater.* **2010**, *22*, E28-62.

(25) Ji, L.; Meduri, P.; Agubra, V.; Xiao, X.; Alcoutlabi, M. Graphene-Based Nanocomposites for Energy Storage. *Adv. Energy Mater.* **2016**, *6*, 1502159.

(26) Ke, Q.; Wang, J. Graphene-Based Materials for Supercapacitor Electrodes – a Review. *J. Materiomics* **2016**, *2*, 37-54.

(27) Bonaccorso, F.; Colombo, L.; Yu, G.; Stoller, M.; Tozzini, V.; Ferrari, A. C.; Ruoff, R. S.; Pellegrini, V. 2D Materials. Graphene, Related Two-Dimensional Crystals, and Hybrid Systems for Energy Conversion and Storage. *Science* **2015**, *347*, 1246501.

(28) Stoller, M. D.; Park, S.; Zhu, Y.; An, J.; Ruoff, R. S. Graphene-Based Ultracapacitors. *Nano Lett.* **2008**, *8*, 3498-3502.

(29) Shao, Y.; El-Kady, M. F.; Lin, C. W.; Zhu, G.; Marsh, K. L.; Hwang, J. Y.; Zhang, Q.; Li, Y.; Wang, H.; Kaner, R. B. 3d Freeze-Casting of Cellular Graphene Films for Ultrahigh-Power-Density Supercapacitors. *Adv. Mater.* **2016**, *28*, 6719-6726.

(30) Chua, C. K.; Pumera, M. Chemical Reduction of Graphene Oxide: A Synthetic Chemistry Viewpoint. *Chem. Soc. Rev.* **2014**, *43*, 291-312.

(31) Gao, W.; Alemany, L. B.; Ci, L.; Ajayan, P. M. New Insights into the Structure and Reduction of Graphite Oxide. *Nat. chem.* **2009**, *1*, 403.

(32) Park, S.; Ruoff, R. S. Chemical Methods for the Production of Graphenes. *Nat. Nanotechnol.* **2009**, *4*, 217-24.

(33) Hummers, W. S.; Offeman, R. E. Preparation of Graphitic Oxide. *J. Am. Chem. Soc.* **1958**, *80*, 1339-1339.

(34) Marcano, D. C.; Kosynkin, D. V.; Berlin, J. M.; Sinitskii, A.; Sun, Z.; Slesarev, A.; Alemany, L. B.; Lu, W.; Tour, J. M. Improved Synthesis of Graphene Oxide. *ACS Nano* **2010**, *4*, 4806-4814.

(35) Yu, H.; Zhang, B.; Bulin, C.; Li, R.; Xing, R. High-Efficient Synthesis of Graphene Oxide Based on Improved Hummers Method. *Sci. Rep.* **2016**, *6*, 36143.

(36) El-Kady, M. F.; Strong, V.; Dubin, S.; Kaner, R. B. Laser Scribing of High-Performance and Flexible Graphene-Based Electrochemical Capacitors. *Science* **2012**, *335*, 1326-1330.

(37) Chiu, P. L.; Mastrogiovanni, D. D. T.; Wei, D.; Louis, C.; Jeong, M.; Yu, G.; Saad, P.; Flach, C. R.; Mendelsohn, R.; Garfunkel, E., *et al.* Microwave- and Nitronium Ion-Enabled Rapid and Direct Production of Highly Conductive Low-Oxygen Graphene. *J. Am Chem. Soc.* **2012**, *134*, 5850-5856.

(38) Patel, M. A.; Yang, H.; Chiu, P. L.; Mastrogiovanni, D. D. T.; Flach, C. R.; Savaram, K.; Gomez, L.; Hemnarine, A.; Mendelsohn, R.; Garfunkel, E., *et al.* Direct Production of Graphene Nanosheets for near Infrared Photoacoustic Imaging. *ACS Nano* **2013**, *7*, 8147-8157.

(39) Yang, S.; Brüller, S.; Wu, Z.-S.; Liu, Z.; Parvez, K.; Dong, R.; Richard, F.; Samorì, P.; Feng, X.; Müllen, K. Organic Radical-Assisted Electrochemical Exfoliation for the Scalable Production of High-Quality Graphene. *J. Am. Chem. Soc.* **2015**, *137*, 13927-13932.

(40) Parvez, K.; Wu, Z.-S.; Li, R.; Liu, X.; Graf, R.; Feng, X.; Müllen, K. Exfoliation of Graphite into Graphene in Aqueous Solutions of Inorganic Salts. *J. Am. Chem. Soc.* **2014**, *136*, 6083-6091.

(41) Ryu, J.; Kim, Y.; Won, D.; Kim, N.; Park, J. S.; Lee, E.-K.; Cho, D.; Cho, S.-P.; Kim, S. J.; Ryu, G. H., *et al.* Fast Synthesis of High-Performance Graphene Films by Hydrogen-Free Rapid Thermal Chemical Vapor Deposition. *ACS Nano* **2014**, *8*, 950-956.

(42) Wang, G.; Yang, J.; Park, J.; Gou, X.; Wang, B.; Liu, H.; Yao, J. Facile Synthesis and Characterization of Graphene Nanosheets. *J. Phys. Chem. C* **2008**, *112*, 8192-8195.

(43) Shin, H. J.; Kim, K. K.; Benayad, A.; Yoon, S. M.; Park, H. K.; Jung, I. S.; Jin, M. H.; Jeong, H. K.; Kim, J. M.; Choi, J. Y. Efficient Reduction of Graphite Oxide by Sodium Borohydride and Its Effect on Electrical Conductance. *Adv. Funct. Mater.* **2009**, *19*, 1987-1992.

(44) Moon, I. K.; Lee, J.; Ruoff, R. S.; Lee, H. Reduced Graphene Oxide by Chemical Graphitization. *Nat. Commun.* **2010**, *1*, 73.

(45) Stankovich, S.; Dikin, D. A.; Piner, R. D.; Kohlhaas, K. A.; Kleinhammes, A.; Jia, Y.; Wu, Y.; Nguyen, S. T.; Ruoff, R. S. Synthesis of Graphene-Based Nanosheets Via Chemical Reduction of Exfoliated Graphite Oxide. *carbon* **2007**, *45*, 1558-1565.

(46) Park, S.; Hu, Y.; Hwang, J. O.; Lee, E.-S.; Casabianca, L. B.; Cai, W.; Potts, J. R.; Ha, H.-W.; Chen, S.; Oh, J. Chemical Structures of Hydrazine-Treated Graphene Oxide and Generation of Aromatic Nitrogen Doping. *Nat. Commun.* **2012**, *3*, 638.

(47) Eda, G.; Fanchini, G.; Chhowalla, M. Large-Area Ultrathin Films of Reduced Graphene Oxide as a Transparent and Flexible Electronic Material. *Nat. Nanotechnol.* **2008**, *3*, 270.

(48) Si, Y.; Samulski, E. T. Synthesis of Water Soluble Graphene. *Nano lett.* **2008**, *8*, 1679-1682.

(49) Tung, V. C.; Allen, M. J.; Yang, Y.; Kaner, R. B. High-Throughput Solution Processing of Large-Scale Graphene. *Nat. Nanotechnol.* **2009**, *4*, 25.

(50) Fan, Z.-J.; Kai, W.; Yan, J.; Wei, T.; Zhi, L.-J.; Feng, J.; Ren, Y.-m.; Song, L.-P.; Wei, F. Facile Synthesis of Graphene Nanosheets Via Fe Reduction of Exfoliated Graphite Oxide. *ACS Nano* **2011**, *5*, 191-198.

(51) Zhang, B.; Song, J.; Yang, G.; Han, B. Large-Scale Production of High-Quality Graphene Using Glucose and Ferric Chloride. *Chem. Sci.* **2014**, *5*, 4656-4660.

(52) Chua, C. K.; Pumera, M. The Reduction of Graphene Oxide with Hydrazine: Elucidating Its Reductive Capability Based on a Reaction-Model Approach. *Chem. Commun.* **2016**, *52*, 72-75.

(53) Chua, C. K.; Pumera, M. Reduction of Graphene Oxide with Substituted Borohydrides. *J. Mater. Chem. A* **2013**, *1*, 1892-1898.

(54) Chua, C. K.; Ambrosi, A.; Pumera, M. Graphene Oxide Reduction by Standard Industrial Reducing Agent: Thiourea Dioxide. *J. Mater. Chem.* **2012**, *22*, 11054-11061.

(55) Pumera, M. Heteroatom Modified Graphenes: Electronic and Electrochemical Applications. *J. Mater. Chem. C* **2014**, *2*, 6454-6461.

(56) Abdelkader, A. M.; Vallés, C.; Cooper, A. J.; Kinloch, I. A.; Dryfe, R. A. W. Alkali Reduction of Graphene Oxide in Molten Halide Salts: Production of Corrugated Graphene Derivatives for High-Performance Supercapacitors. *ACS Nano* **2014**, *8*, 11225-11233.

(57) Yuan, K.; Xu, Y.; Uihlein, J.; Brunklaus, G.; Shi, L.; Heiderhoff, R.; Que, M.; Forster, M.; Chassé, T.; Pichler, T., *et al.* Straightforward Generation of Pillared, Microporous Graphene Frameworks for Use in Supercapacitors. *Adv. Mater.* **2015**, *27*, 6714-6721.

(58) Lei, Z.; Christov, N.; Zhao, X. S. Intercalation of Mesoporous Carbon Spheres between Reduced Graphene Oxide Sheets for Preparing High-Rate Supercapacitor Electrodes. *Energy Environ. Sci.* **2011**, *4*, 1866-1873.

(59) Chen, J.; Sheng, K.; Luo, P.; Li, C.; Shi, G. Graphene Hydrogels Deposited in Nickel Foams for High-Rate Electrochemical Capacitors. *Adv. Mater.* **2012**, *24*, 4569-4573.

(60) Jha, P. K.; Singh, S. K.; Gatla, S.; Mathon, O.; Kurungot, S.; Ballav, N. Pb^{2+}—N Bonding Chemistry: Recycling of Polyaniline–Pb Nanocrystals Waste for Generating High-Performance Supercapacitor Electrodes. *J. Phys. Chem. C* **2016**, *120*, 911-918.

(61) Inzelt, G. *Conducting Polymers: A New Era in Electrochemistry*. Springer Science & Business Media: 2012.

(62) Zhong, C.; Deng, Y.; Hu, W.; Qiao, J.; Zhang, L.; Zhang, J. A Review of Electrolyte Materials and Compositions for Electrochemical Supercapacitors. *Chem. Soc. Rev.* **2015**, *44*, 7484-7539.

(63) El-Kady, M. F.; Shao, Y.; Kaner, R. B. Graphene for Batteries, Supercapacitors and Beyond. *Nat. Rev. Mater.* **2016**, *1*, 16033.

Chapter 2

Reduction of Graphene Oxide by $FeCl_2$/HCl for Supercapacitor Applications

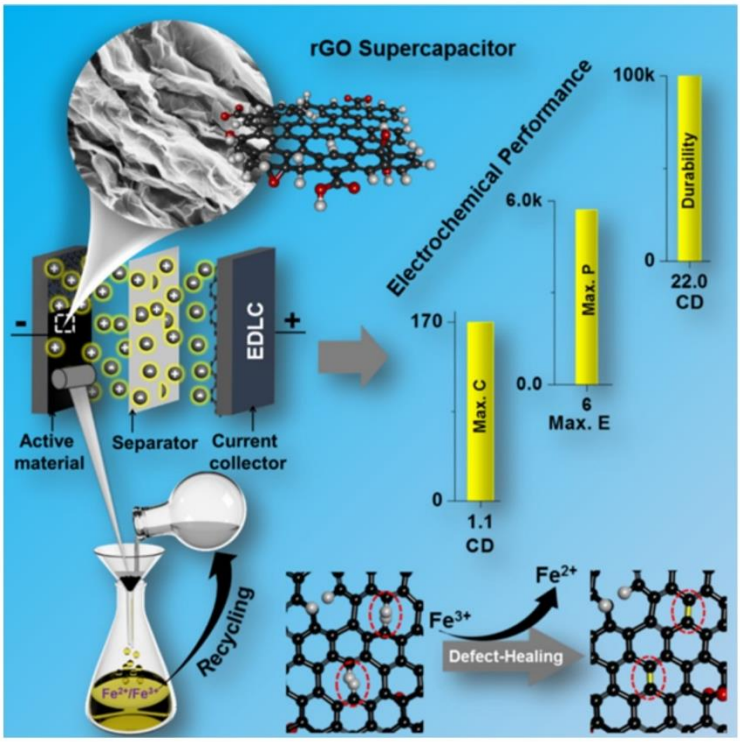

2.1. Introduction

The most common reducing agents for the reduction of graphene oxide (GO) are N_2H_4, $NaBH_4$, $SnCl_2$, and ascorbic acid.[1-2] The fast reduction kinetics associated with aforementioned reducing agents lead to an imbalance between the essential parameters such as electrical conductivity, surface area, and porosity, often failing to fulfil the theoretical energy demands and thus industrial attention.[1,3-10]

In this chapter, we have established a simple and scalable, one-step, cost-effective, chemical reduction of GO in aqueous medium in which $FeCl_2$/HCl was used for the first time as a mild reducing agent offering slow reduction kinetics for the generation of self-assembled reduced graphene oxide (rGO) material with optimally balanced physicochemical properties. The fabricated all solid-state supercapacitors of our as-synthesized rGO material (without further processing) exhibited (1) significantly higher specific capacitance than those of rGO materials derived from conventional reducing agents and (2) a remarkable charge-discharge cycling stability. We have also fabricated flexible supercapacitors by using our rGO as active material upon coating it on an Au-coated polyethylene-terephthalate (PET) sheet which showed high durability. Furthermore, the capacitance value as well as the energy and power density values were remarkably enhanced with the help of an organic electrolyte, namely, tetraethylammonium tetrafluoroborate/ acetonitrile ($TEABF_4$/AN). Finally, the reducing agent was simply recycled upon treating the filtrate with hydrochloric acid, thereby making our research industrially relevant.

2.2. Materials and Methods

Graphite flake (+100 mesh), iron(II) chloride ($FeCl_2.4H_2O$), potassium permanganate ($KMnO_4$), hydrogen peroxide (H_2O_2), tetraethylammonium tetrafluoroborate ($TEABF_4$), and hydrazine hydrate ($N_2H_4{\cdot}H_2O$) (50%–60%) were purchased from Sigma-Aldrich. Sulfuric acid (H_2SO_4), phosphoric acid (H_3PO_4), nitric acid (HNO_3), methanol (MeOH), N-methyl-2-pyrrolidone (NMP), acetonitrile (AN), and hydrochloric acid (HCl) were purchased from RANKEM. Poly(vinyl alcohol) PVA (M_w ~115,000; 98–99 mol% hydrolysed) was purchased from Loba Chemie, and iron(III) chloride anhydrous ($FeCl_3$) was purchased from CHEMLABS (India).

GO was chemically synthesised through modified Hummers' method as follows: ~6 g of powdered graphite flake was stirred at ~5 °C with 120 mL of concentrated H_2SO_4 for ~1 hr followed by addition of $KMnO_4$ (18 g) in parts taking ~30 min. The mixture was then allowed to stir at room temperature (RT) and after 24 hr, 240 mL of MQ (milli-Q) water was added slowly with continuous stirring. Further, the mixture was heated to 80 °C and brought back to RT after 3 hr of stirring. Finally, a solution of water and hydrogen-peroxide (720 mL H_2O + 60 mL H_2O_2) was added into the mixture and after a few hr, chocolate brown coloured material was extracted and washed with H_2O, 5% HCl solution, and acetone followed by vacuum drying at 70 °C for ~24 hr. The prepared graphite oxide was further exfoliated in MQ water (1 mg/mL GO solution) and multi layers were removed by centrifugation (5 min at 1000 rpm).

To reduce the GO, 150 mL of GO solution was added to another 180 mL of aqueous HCl solution of $FeCl_2.4H_2O$ (~1.8 g in 150 mL H_2O + 30 mL HCl). The mixture was then stirred for ~24 hr at 94 °C and the black precipitate thus formed, was filtered and washed with H_2O and methanol, and it was then vacuum dried for 12 hr.

To test the defect healing of rGO by Fe(III) ions, we subjected rGO to three different reaction conditions other than the abovementioned protocol, firstly, we isolated rGO after 12 hr and 72 hr (rGO1 and rGO2, respectively) of stirring at 94 °C. Secondly, after 24 hr, ~1.5 g of $FeCl_3$ (anhydrous) was deliberately added into the reaction mixture and stirred for the next 48 hr at 94 °C (rGO3). Other than this, we also reduced the GO by a conventional reducing agent, hydrazine hydrate ($N_2H_4.H_2O$), (rGO4), in a typical synthesis, 250 mL of GO (1 mg/mL) and 0.5 mL $N_2H_4.H_2O$ were mixed in a 500 mL round-bottom flask and stirred at 90 °C for 12 hr. Black precipitate thus obtained was filtered and washed with H_2O and methanol, and was vacuum dried.

To confirm the recycling of reducing agent, after the first reduction of GO to rGO, the filtrate (Fe(II)/Fe(III)) was collected and the volume was reduced so as to maintain the volume ratio of the reducing agent to GO. Concentrated HCl was added to the filtrate, and the same reduction process was performed on subsequent feeds of GO solutions (named rGO5).

To obtain a 10 wt %, 1:1 PVA:H_2SO_4 gel polymer electrolyte (GPE), 2 g of PVA powder was added to 20 mL of MQ water and stirred at 80 °C to get a clear solution. It was then cooled to RT, and 2 g of concentrated H_2SO_4 (98%) was added followed by additional stirring for next 30 min.

GO and rGO materials were characterized by Fourier transformed infrared spectroscopy (FTIR), UV-visible spectroscopy (UV-vis), thermogravimetric analysis (TGA), Raman spectroscopy (633 nm laser excitation wavelength, we have performed Lorentz fitting in each Raman curve to get I_D and I_G value), powder X-ray diffraction (PXRD), field-emission scanning electron microscopy (FESEM), atomic force microscopy (AFM), and transmission electron microscopy (TEM). X-ray photoelectron spectroscopy (XPS) measurements were carried out using Mg-Kα (1253.6 eV) source and DESA-150 electron analyzer (Staib Instruments, Germany). The binding-energy scale was calibrated to Au-$4f_{7/2}$ line of 84.0 eV. The analyzer was operated at 40 eV pass energy. Pressure in the chamber during analysis was ~ $5x10^{-9}$ Torr. Electrochemical measurements were performed using a BioLogic potentiostat (model A VMP-3) and PARSTAT MC, galvanostat/potentiostat, PMC-2000.

To fabricate all-solid-state supercapacitors, a slurry of 95% active material (various rGOs) and 5% Nafion with NMP solvent was coated onto the surface of a 1x1 cm^2 area of grafoil sheet. For electrode preparation, 1x3 cm^2 grafoil was measured where the excess area was used as the current collector during the measurements. The electrodes were dried under an infrared (IR) lamp overnight, they were then assembled into supercapacitor device by sandwiching 10 wt % of PVA-H_2SO_4 GPE between the electrodes along with a Celgard membrane (3501) as separator. For all-solid-state supercapacitor testing, respective loadings (per cm^2) of rGO, rGO', rGO1, rGO2, rGO3, rGO4, and rGO5 were ~0.9, ~1.3, ~1.1, ~1.1, ~1.1, ~1, and ~1.2 mg, respectively.

To make all-solid-state flexible supercapacitor device, the as-prepared slurry (mentioned above) was coated on Au sputtered (~60 nm) PET sheet and then dried under an IR lamp for ~12 hr. Finally, 10 wt % PVA-H_2SO_4 GPE along with the Celgard separator was used for the supercapacitor assembly. The loading of rGO was ~0.25 mg/cm^2. The Au-sputtered area on PET sheet was ~3.5 cm^2, out of which rGO was coated only on an area of ~2.5 cm^2, leaving an area of ~1 cm^2 of Au-sputtered PET for electrode contact. The all-solid-state flexible supercapacitor device was wrapped with tape to avoid any misplacement as the device had to undergo multiple bending cycles during the flexibility test and thus extra care was taken by applying the tape to avoid device movement.

To perform electrochemical measurements in organic electrolyte, the rGO slurry was made by mixing 95% active material with 5% Nafion in NMP solvent. Further, ~1.1 mg of material was loaded on grafoil sheet (1x1 cm^2), with 1x3 cm^2 extra area left as a current collector and

electrode contacts. The measurement was performed with 1 M $TEABF_4$/AN electrolyte in a two-electrode setup.

2.3. Results and Discussion

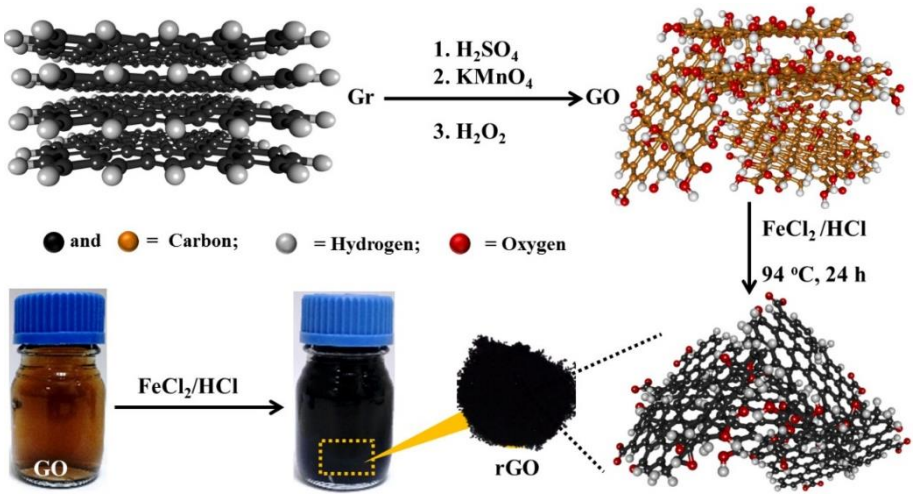

Figure 2.1. *Schematic presentation and optical photographs of graphite (Gr) oxidation to graphene oxide (GO) and subsequent reduction to reduced graphene oxide (rGO).*

Oxidation of graphite (Gr) powder to GO and subsequent reduction to rGO (Figure 2.1) was probed by various spectroscopic and microscopic techniques (Figures 2.2 and 2.3). The C1s XPS data for GO revealed the presence of various functional groups such as, C–C, C–O/C=O, and –COOH at the respective binding energy positions of 284.9, 286.9, and 288.4 eV, validating the reasonable oxidation of graphite (Figure 2.2a). In accordance with the reduction of rGO, the intensity ratio between the peaks at ~284.8 eV and ~286.3 eV decreased prominently as most of the oxide groups were removed in the process. Also, the intensity of the peak at ~288.1 eV decreased reasonably indicating substantial removal of –COOH functional group (Figure 2.2b).[11-13] Overall, from the C1s XPS data, ~20% reduction of the oxygenated C was estimated with respect to the C=C graphitic backbone in the course of GO to rGO reduction. In Raman spectra, broad bands: D band (defect peak from inter valley scattering) at 1,330 cm^{-1} and G band (graphene G peak) at 1,590 cm^{-1} appeared for both GO and rGO. However, the peak intensity ratios (I_D/I_G) were different for GO (2.71) and rGO (2.45). The decreased I_D/I_G intensity for rGO suggests the recovery of the sp^2 carbon networks in rGO (Figure 2.2c).[12,14-15]

A sharp PXRD peak (002) of graphite appeared at 2θ = 26.4° (d ~ 0.337 nm) which shifted to 10.7° after oxidation, as the highly decorated oxide groups (–COOH, –C=O/–C–O, –OH) increased the interlayer distance (d~ 0.825 nm) between the sheets (Figure 2.2d). The PXRD pattern of rGO showed broad peak at 2θ = ~22.5° with interlayer spacing of ~0.391 nm (Figure 2.2d) indicating optimal reduction of GO which prevented the stacking of the sheets and, simultaneously weakening of the π–π and van der Waals interactions among the layers.[11,15]

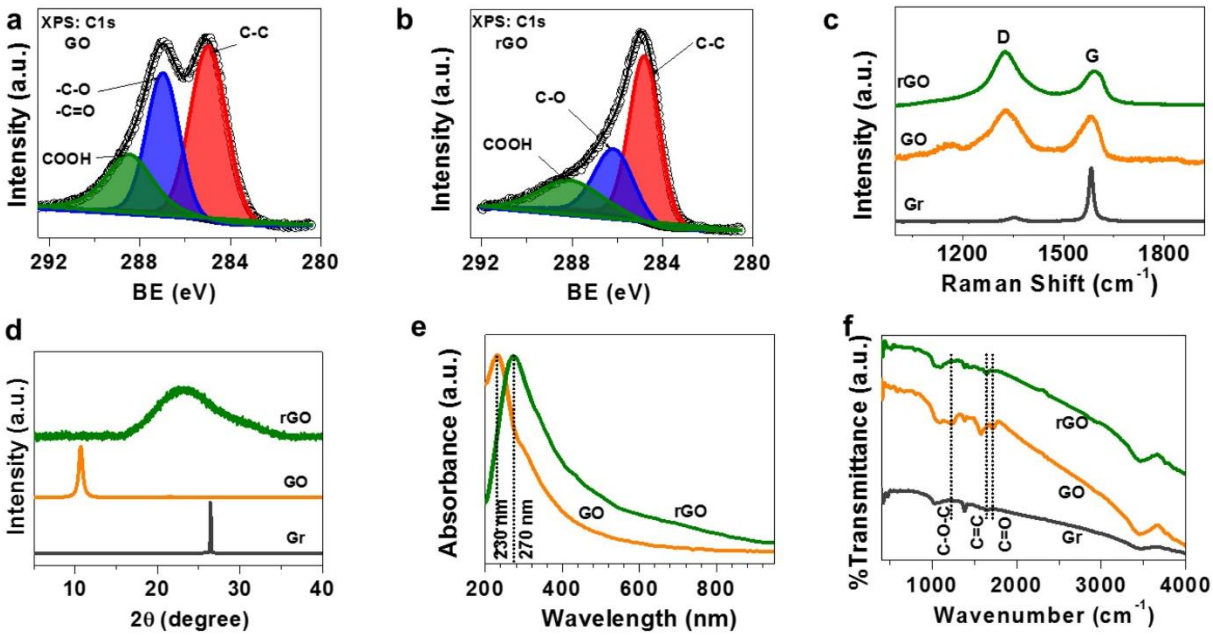

Figure 2.2. *(a) C1s XPS data of GO. (b) C1s XPS data of rGO. (c) Raman spectra of Gr, GO, and rGO. (d) Powder X-ray diffraction (PXRD) patterns of Gr, GO, and rGO. (e) UV-vis spectra of GO and rGO and (f) FTIR spectra of Gr, GO and rGO. Characteristic absorptions are marked by dotted lines.*

The above characterizations were also complimented by UV-vis, TGA (discussed later), and FTIR. In UV-vis spectra of GO (Figure 2.2e) absorption peaks at 230 and 302 nm are typical of π-π^* and n-π^* transition of C=C and C=O bonds respectively, validating the oxidation of graphite sheets, whereas in case of rGO, peak at 270 nm manifested the re-gaining of π-conjugation network after the reduction of GO.[11,16] The FTIR spectra of Gr, GO, and rGO recorded on pressed KBr pellets (Figure 2.2f). The C=C stretching peak at 1641 cm^{-1} found to be prominant in case of Gr, however, for GO it was almost disappeared. Peaks at 1720 cm^{-1}, 1386 cm^{-1}, 1224 cm^{-1} and 1093 cm^{-1}, referring to C=O stretching, C-OH, C-O-C, and C-O (alkoxy) vibrations respectively. After reduction of GO to rGO, the C=O stretching and C-O-C vibrations peaks almost disappeared suggesting the overall efficient reduction of GO (Figure 2.2f).[17]

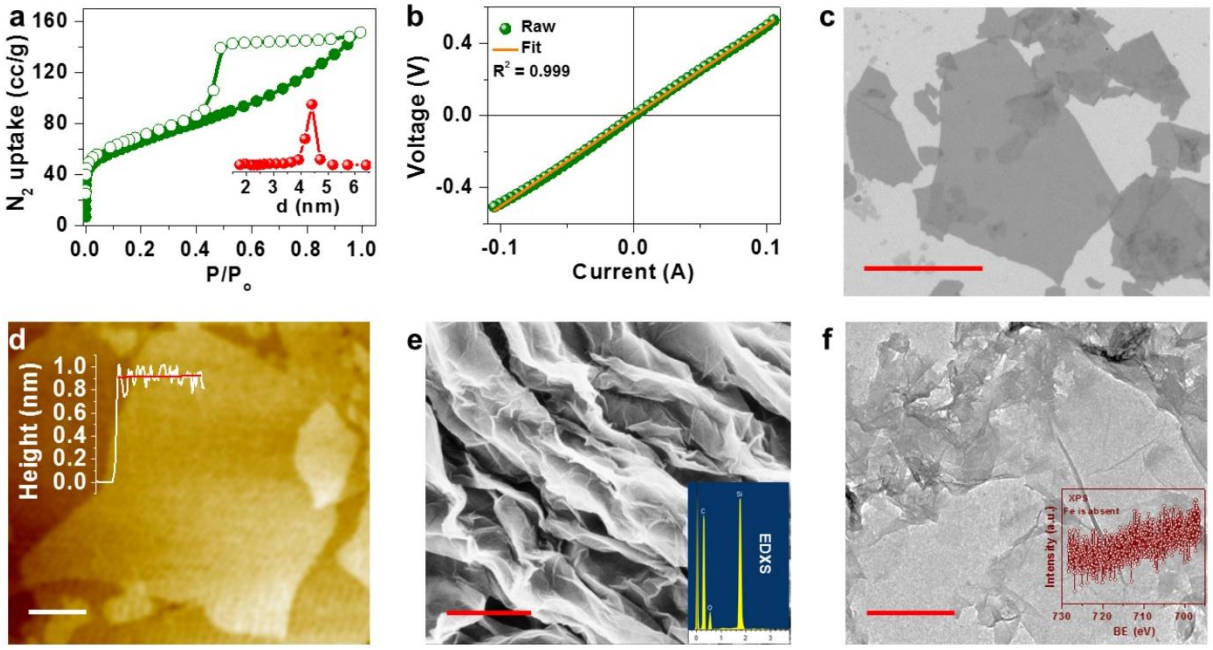

Figure 2.3. *(a) N_2 adsorption (filled circle) and desorption (open circle) profile of rGO at 77 K. Inset: pore diameter (~4.4 nm) of rGO. (b) Current-voltage (I–V) plot of rGO. (c-d) FESEM and AFM images of GO. Scale bars are 5 µm and 1 µm, respectively. (e) FESEM image of rGO. Scale bar, 500 nm. Inset: EDXS of rGO and (f) TEM image of rGO. Scale bar, 300 nm. Inset: Fe 2p XPS.*

To estimate the total surface area of rGO, N_2 gas adsorption-desorption isotherms were recorded at 77 K (Figure 3.3a) and the graph revealed a hysteresis loop from ~0.6 to ~0.9 relative pressure, characteristic of a type-IV isotherm (indicating the mesoporous nature of the material).[18] The calculated surface area of rGO was found to be ~229 m^2/g along with a pore diameter of ~4.4 nm (Figure 3.3a: inset). To calculate the pore size of rGO a non-local density functional theory on a carbon model was employed. The high surface area and pore diameter indicates the presence of bigger pores between the unstacked rGO sheets. Electrical conductivity measurements were done on a pressed (10 tons) rGO thin film. The direct current (DC) electrical conductivity was found to be ~500 S/m (Figure 3.3b), which is comparable with or better than the reported values for rGO chemically reduced using other reducing agents.[1] Altogether, rGO reasonably recouped π-conjugation and electrical conductivity. The FESEM and AFM images (Figures 3.3c, d) of GO depicted very thin layered sheets extending laterally to a few micro-meters length with layer thickness of ~0.9 to ~1.8 nm. Thin layers of GO sheets are crucial in the cases where after subsequent reduction to a few layers of rGO, employ for many applications such as charge transport and energy-storage. Our optimized reaction conditions indeed, produced a few layers of rGO as evident from the FESEM, TEM images

(Figures 3.3e, f). From XPS we anticipated that the quality of rGO produced by our method is very good. In the XPS analysis, we could not detect any impurity signals of Fe or Cl, and such impurity peaks were also absent in the EDXS analysis (inset: Figures 2.2e, f).

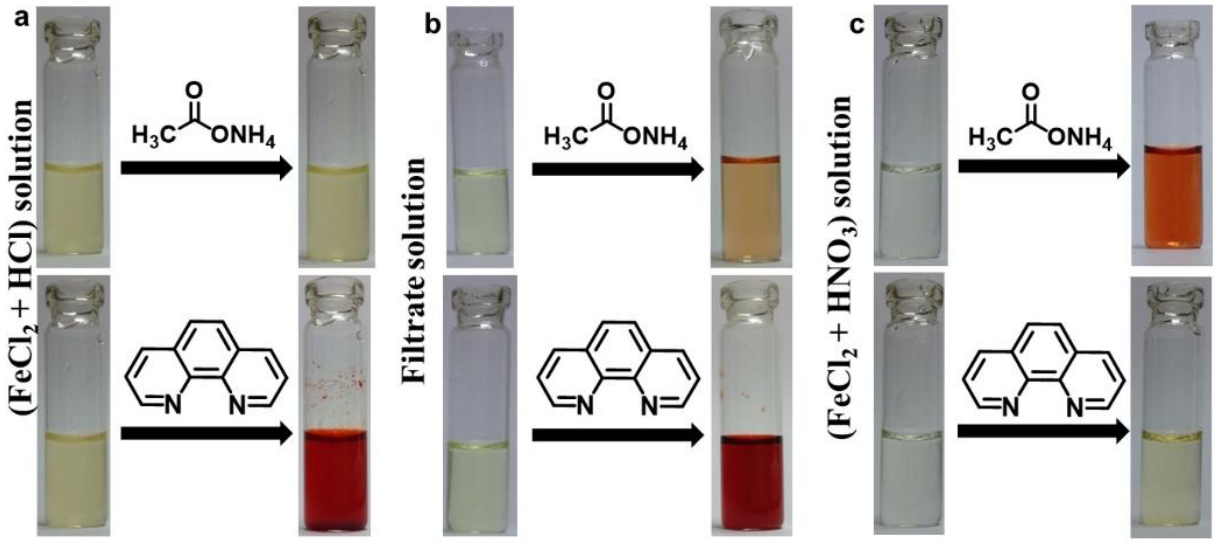

Figure 2.4. *Qualitative detections of Fe^{2+} and Fe^{3+} ions were done by using 1,10-phenanthroline and ammonium acetate, respectively: (a) $FeCl_2$+ HCl (indicating the presence of Fe^{2+} ion) (B) Filtrate (indicating the presence of both Fe^{2+} and Fe^{3+} ions) and (C) $FeCl_2$+HNO_3 (indicating the presence of only Fe^{3+} ion).*

Looking into the reaction scenario, a typical oxidation-reduction of Fe(II) to Fe(III) and simultaneous GO to rGO can be realized; therefore, the overall reaction is proposed to be,

$$GO + Fe^{2+} + H^+ + Cl^- \rightarrow rGO + Fe^{3+} + H^+ + Cl^-$$

Since GO to rGO conversion was discussed in detail we tried to probe the Fe(II) and Fe(III) in the reaction mixture. We thus performed a colour test of the filtrate solution (Figures 2.4a, b), which interestingly showed the presence of Fe(II) majorly and small amount of Fe(III) ions as well, possibly in dynamic equilibrium as,

$$Fe^{2+} + H^+ + Cl^- \leftrightarrow Fe^{3+} + e^- + H^+ + Cl^-$$

Thus, our approach of using a non-traditional reducing agent, Fe(II), apart from efficiently reduced GO to rGO, also provided the possibility of recycling the filtrate as the reducing agent, after adding HCl, for subsequent batches of GO (Figures 2.10a, b).

The reduction of GO to rGO was highly optimized in the terms of temperature, reaction time period, concentration of Fe(II) and HCl, and monitored by UV-vis spectroscopy as the tool.

To check the effect of temperature, reactions were performed at different temperatures (RT, 50 °C, and 80 °C) but in every case, reduction was incomplete (Figure 2.5a).

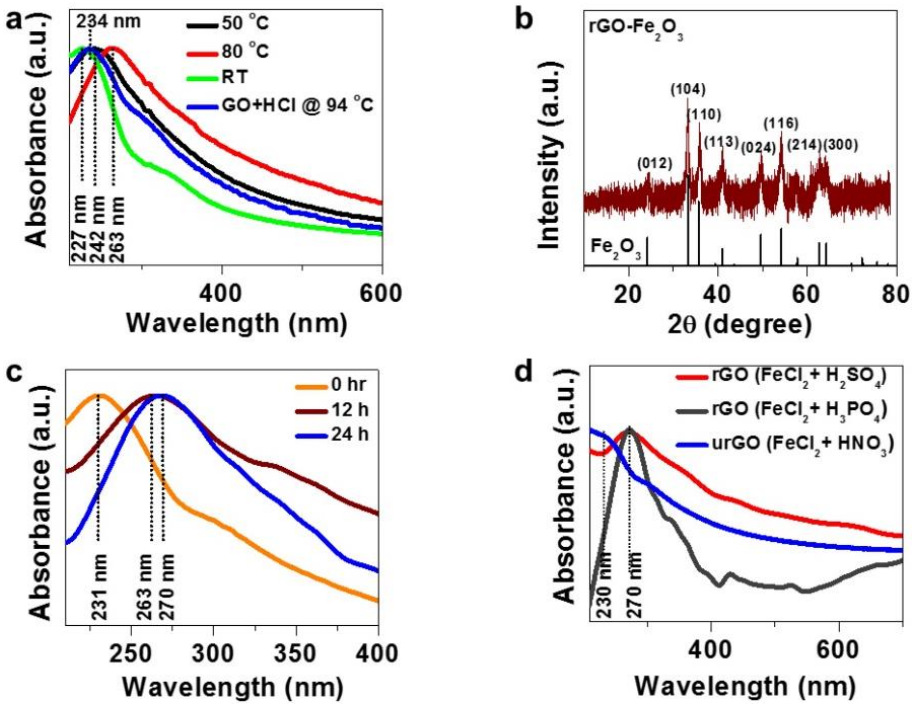

Figure 2.5. *(a) UV-vis spectra of GO at different reaction temperatures: RT, 50 ℃ and 80 ℃ and GO + HCl at 94 ℃ for 24 hr. (b) PXRD pattern of a composite obtained after reducing GO with $FeCl_2$ only i.e. without additional use of HCl (calculated PXRD pattern of Fe_2O_3 from JCPDS database No. 01-089-0597). (c) UV-vis spectra of GO at different reduction periods of 0 hr, 12hr, and 24hr and (d) UV-vis spectra of reduced GO and un-reduced GO (urGO).*

We have also tried to reduce GO with either HCl or Fe(II) alone: the former (Figure 2.5a) was unable to bring out the GO reduction, whereas the latter resulted in a mixture of partially reduced GO and small amount of Fe_2O_3 particles (Figure 2.5b).[19] In line with the principles of hard soft acid-base (HSAB), Fe(II) is a borderline acid, whereas Fe(III) is a hard acid, and hence Fe(III) will tend to associate with H_2O/OH^- (hard bases) and will lead to the formation of a mixture of partially reduced GO and Fe_2O_3 particles (Figure 2.5b).[19-20]

Further, reduction of GO was also performed only for 12 hr, where incomplete reduction was realized (Figure 2.5c). The amount of HCl used in the reduction process not only enhanced the reducing efficiency of Fe(II) but also prevented the formation of oxide particles from the (Fe(II)/Fe(III)) mixture. Apart from HCl, we have also explored other mineral acids such as H_2SO_4, HNO_3, and H_3PO_4 with $FeCl_2$ and reduction were realised only in the cases of H_2SO_4 and H_3PO_4 (Figure 2.5d), whereas, surprisingly, as soon we have incorporated HNO_3, GO was

found to be un-reduced which is because of the pre-conversion of Fe(II) to Fe(III) by HNO_3 acid (Figures 2.5d and 2.4c).[21] After successful characterisation, materials were tested for electrochemical performance.

We have fabricated all-solid-state supercapacitors of rGO in 10 wt% PVA-H_2SO_4 GPE[22] electrolyte and connected in series (4-electrodes) to illuminate a white light emitting diode (white LED) where rGO usually forms electric double-layer (EDL) interfaces with the electrolyte (Figure 2.6a).[10] Cyclic voltammetry (CV), charge-discharge (CD), and electrochemical impedance spectroscopy (EIS) measurements techniques were used to evaluate the overall performance of rGO. The CV measurements of the synthesized rGO at different scan rates from 10-1000 mV/s (Figure 2.6b) are nearly rectangular in shape which strongly suggests the formation of a fine EDL at the interface of active material (rGO) and ions at each scan rate via percolation through the pores of rGO. CD measurements showed a symmetric triangular curve (Figure 2.6c), again indicating the origin of capacitance to be EDL and high-charge mobility at the electrode's interface. Furthermore, at lower current densities, the potential drops (V = IR, where I is current and R is resistance) are extremely small, indicating that rGO possesses negligible internal resistance, an important factor for enhancing the capacitance. From EIS, electrolyte ion transport as well as the overall resistance in the material can be analysed (Figure 2.6d). The Nyquist plot of rGO is nearly vertical in the low frequency region, and a zoomed-in section (Figure 2.6d, inset) at high frequency shows a very small semicircle indicating an ideal capacitive behaviour, i.e., very low charge-transfer resistance with high electrolyte diffusion inside the active material (rGO). In Nyquist plot, the point of intersection with the real (Z) axis corresponds to the equivalent series resistance (Rs), which was found to be ~0.92 Ω, thereby suggesting material could possess high power in the rGO device (Figure 2.6d, inset).[10] The time constant ($\tau_o = 1/f_o$; f_o is the frequency at a phase angle of ~45°) of rGO was calculated from the Bode phase plot (Figure 2.6e) to be ~0.188 s (f_o = 5.32 Hz at ~45°) which in fact reveals a faster charge-discharge rate of the supercapacitor.[10,23] The specific capacitance (gravimetric capacitance, C_G; and areal capacitance, C_A) of rGO was calculated from the CD curves at different current densities (Figure 2.7a) implementing the formula mentioned in the chapter 1. Remarkably, the C_G of rGO found to be ~170 F/g at a current density of 1.1 A/g, whereas C_A was calculated to be ~155 mF/cm^2 at a current density of 1 mA/cm^2. Such high capacitance values, in fact, are the best values so far amongst rGO prepared by other chemical reduction methods (Table 2.1).

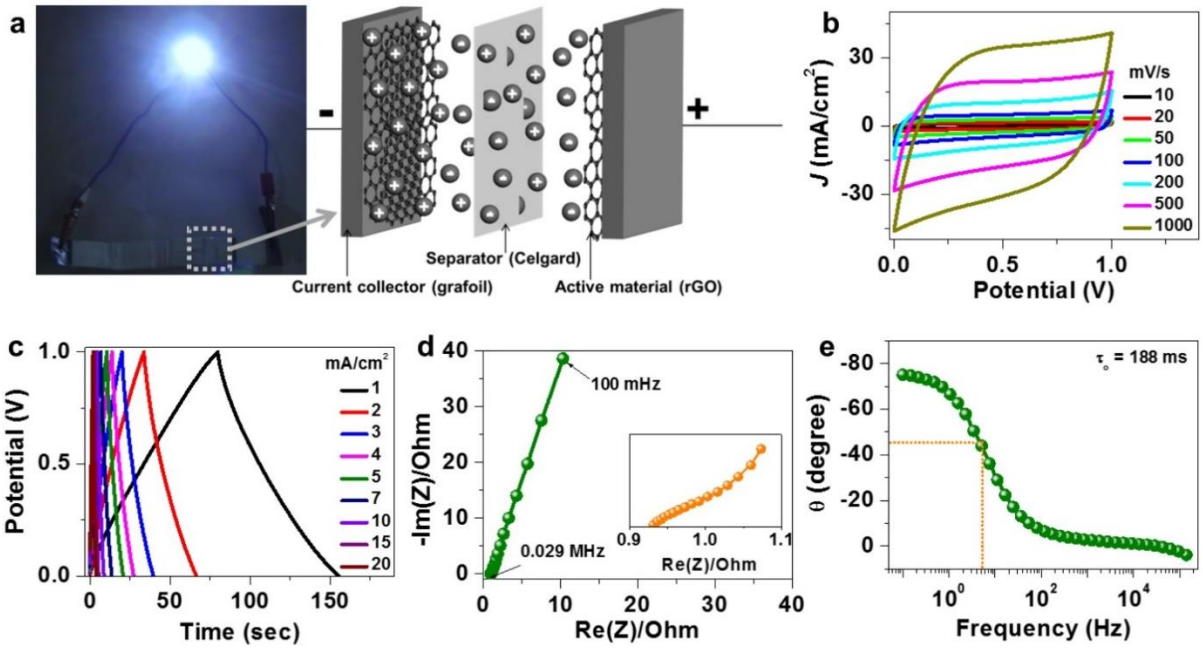

Figure 2.6. *(a) Optical photographs of lighting of a 4 V white-light-emitting diode by the four series connected rGO supercapacitor which has EDLC characteristics shown as a schematic presentation in all solid-state fashion. (b-c) CV and CD plots of rGO at different scan rates from 10 to 1000 mV/s and current densities from 1 to 20 mA/cm^2, respectively. (d) Nyquist plot of rGO. Inset: zoomed-in graph of the high-frequency region. (e) Bode phase plot of rGO.*

The capacitance (C_G and C_A) of rGO were plotted against current density (Figure 2.7a) where interestingly, both the gravimetric (C_G) and areal (C_A) capacitance values were retained more than 50% even at higher current densities. Also we have calculated the C_G at different scan rates (Figure 2.7b) which complemented the CD data. It has already been seen that active mass loading of rGO changes the capacitance values, therefore, to investigate the effect of active mass loading on supercapacitive performance, we varied the gravimetric mass of rGO from ~0.11 mg to ~1.8 mg per electrode and capacitance values at 10 mV/s varied from C_G ~ 357 F/g (C_A ~ 39.2 mF/cm^2) to C_G ~ 117 F/g (C_A ~ 175 mF/cm^2) (Figure 2.7c) which suggests our rGO material could be a promising candidate for developing micro-supercapacitors as well as macro-supercapacitors. Also, the rate-independent capacitance value of rGO estimated to be ~ 105 F/g which is impressive (Figure 2.7d).[24] The capacitance values of our rGO in the presence of conventional electrolytes such as 10 wt% PVA-H_2SO_4 also appeared to be comparable with those obtained with ionic-liquids as electrolytes. Thus, we also anticipate that the recently proposed concept of a bi-redox ionic liquid could further enhance the capacitance value of our rGO close to its theoretical limit.[25]

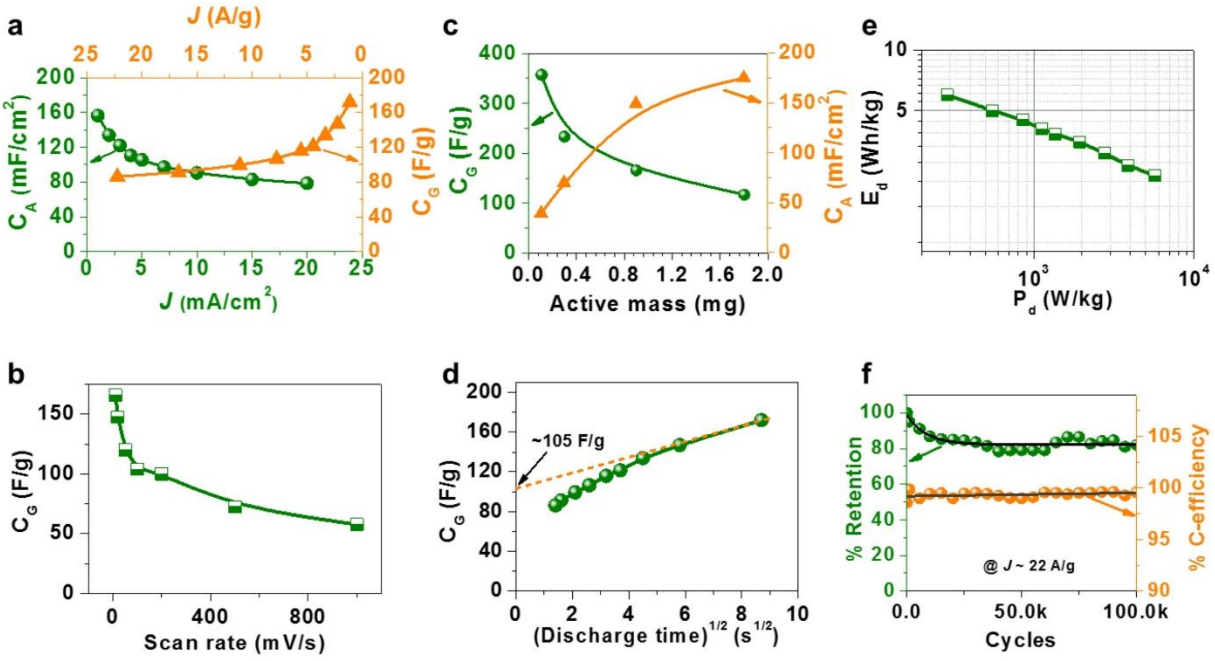

Figure 2.7. *(a) Current density versus specific capacitance (C_A and C_G) plots of rGO. (b) C_G versus scan rate plot of rGO. (c) Specific capacitance (at 10 mV/s) at different active mass loading of rGO. (d) C_G at different (discharge time)$^{1/2}$. (e) Ragone plot of rGO and (f) Durability performance of the rGO supercapacitor over 100,000 continued CD cycles at a current density of 22 A/g.*

To fulfil the current scenario of energy and power demands, very high power (P_d) and energy (E_d) densities of a supercapacitor are prerequisites, however, due to un-tuned synthetic strategies of rGO most of the rGO-based supercapacitors are unable to cope up with such high demands.[26] The re-stacking of rGO sheets due to strong π-π and van der Waals interaction could be the factors that limits the ion transport through the channels and restricts the accessibility of active surface area to the ions to form EDL. This significant decrease in the accessible active surface area of rGO reduces the overall capacitance lower than the expected value.[10] The maximum power density of our rGO was estimated to be ~5.7 kW/kg at an energy density of ~2.4 Wh/kg, which surpasses the previously reported values of rGO materials synthesized by chemical reduction of GO using different reducing agents (Figure 2.7e and Table 2.1). A cycling stability test of the rGO device was performed at a relatively high *J* of 22 A/g, giving more than 80% capacitance retention with 100% Coulombic efficiency even after 100,000 cycles of continued operation (Figure 2.7f). Interestingly, even at such high *J* of 22 A/g, the EDL feature of rGO was retained beyond 100k cycles (Figure is given in the reference relevant to this chapter). As the energy-storage devices in general go through repeated charging-discharging cycles, the long-term stability of the material is of critical

importance.

The initial decrease in the capacitance is attributed to the presence of some oxygen-containing groups which slowly get oxidized and evolved with possible collapsing of some pores.

Table 2.1. *Comparative assessments on C_A and C_G, number of cycles, % retention, and E_d and P_d.*

Materials	Reducing agents	Capacitance	Electrolyte	Cycles	Ret.	Max. E_d (Wh/kg)	Max. P_d (kW/kg)	Refs.
rGO	**$FeCl_2$/HCl**	**171 F/g @ 1.1 A/g**	**10 wt% PVA-H_2SO_4**	**100000 @ 22 A/g**	**>82%**	**6.2**	**5.7**	**Our work**
		282 F/g @ 1.8 A/g	**$TEABF_4$/AN**	**---**	**---**	**59.6**	**27**	
rGO	LiCl-KCl	203 F/g @ 0.2 A/g	6 M KOH	2000 @ 0.5 A/g	97%	---	---	17
PGFs	$NaBH_4$	186 F/g @ 1 A/g	6 M KOH	5000 @10 A/g	97%	3.4	4.6	27
rGO	N_2H_4	41.5 F/g @ 0.1 A/g	6 M KOH	---	---	1.3	2.8	28
G	N_2H_4	203~192 @ 0.1 A/g	---	---	---	7-9	---[12]	29
G-paper	N_2H_4	136 F/g @ 10 mV/s	6 M KOH	2000 @ 10 A/g	96%	4.8	5.1	16
G-carbon	N_2H_4	112 F/g @5 mV/s	PVA-H_2SO_4	5000	94%	---	---	8
G-gel	Vitamin C	~45 mF/cm^2 @ 0.67 mA/cm^2	5M KOH	10000 @10 mA/cm^2	90%	---	---	30
rGO	N_2H_4	110 F/g @ 0.5 A/g	1M $LiPF_6$	---	---	---	---	4
f-rGO	N_2H_4	118.5 F/g @ 1 A/g	H_2SO_4	1000 @ 1 A/g	89%	---	---	5
G- sheet	Zn powder	86 F/g @ 1 A/g	6 M KOH	5000 @ 5 A/g	112%	---	---	6
rGO	R-OH	35 F/g @ 5 mV/s	6M KOH	---	---	---	---	31
rGO	Fe/H^+	94 F/g @ 5 mV/s	6M KOH	1000 @ 10 mV/s	100%	---	---	32
G-sheet	N_2H_4	140 F/g @ 1 A/g	1M H_2SO_4	10000 @ 0.5 A/g	95 %	---	---	33
CMG	N_2H_4	135 F/g @ 10mA	5.5 M KOH	---	---	4.69	1.78	7

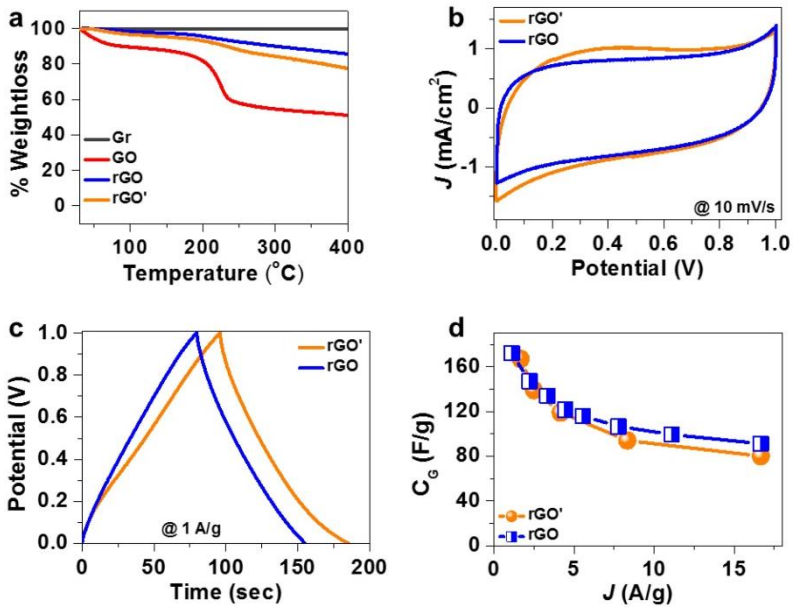

Figure 2.8. *(a) TGA plots of Gr, GO, rGO, and rGO'. (b-c) CV and CD plots of rGO and rGO' and (d) comparison of C_G of rGO and rGO' at different current densities.*

Our as-synthesized rGO material is highly stable at ambient conditions. To demonstrate the stability, we used ~one-year-old rGO sample (rGO') and firstly, compared the thermal stability of rGO' with that of a freshly prepared rGO sample. The TGA profiles of rGO and rGO' looked very similar and both the materials showed good thermal stability up to ~200 °C (with only ~5% weight loss for both the materials). No weight loss was observed for Gr due to stable stacked carbon network. For GO, the weight loss was occured at three different temperatures – ~35 °C, 190 °C, and at ~400 °C, because of the vaporisation of absorbed water, removal of oxygenated functional groups, and stable oxygenated groups, respectively (Figure 2.8a).[11,17] Also, the supercapacitive performance of rGO and rGO' were compared and the values of gravimetric capacitance were found to be in the range of ~170 F/g (Figures 2.8b-d), which clearly states the quality/stability of the material. We have also fabricated an all solid-state flexible supercapacitor device of rGO (Figure 2.9a) in order to demonstrate the stability as well as the performance in multiple bending cycles. CV was performed at bending angles of 0° and 180° leading to unchanged plots (Figure 2.9b). Remarkably, even after 500 bending cycles, the performance of the rGO supercapacitor remained almost unaltered (Figures 2.9c, d). The areal capacitance was calculated to be ~29 mF/cm^2 at a current density of 1 mA/cm^2 (Figure 2.9e).

Overall, our results strongly supports the rGO obtained with $FeCl_2$/HCl, as a reducing agent, to be a promising candidate for the fabrication of all-solid-state and flexible electrochemical energy-storage devices. The cost of the raw chemicals for production of 1 g of rGO in our laboratory is estimated to be less than $10.

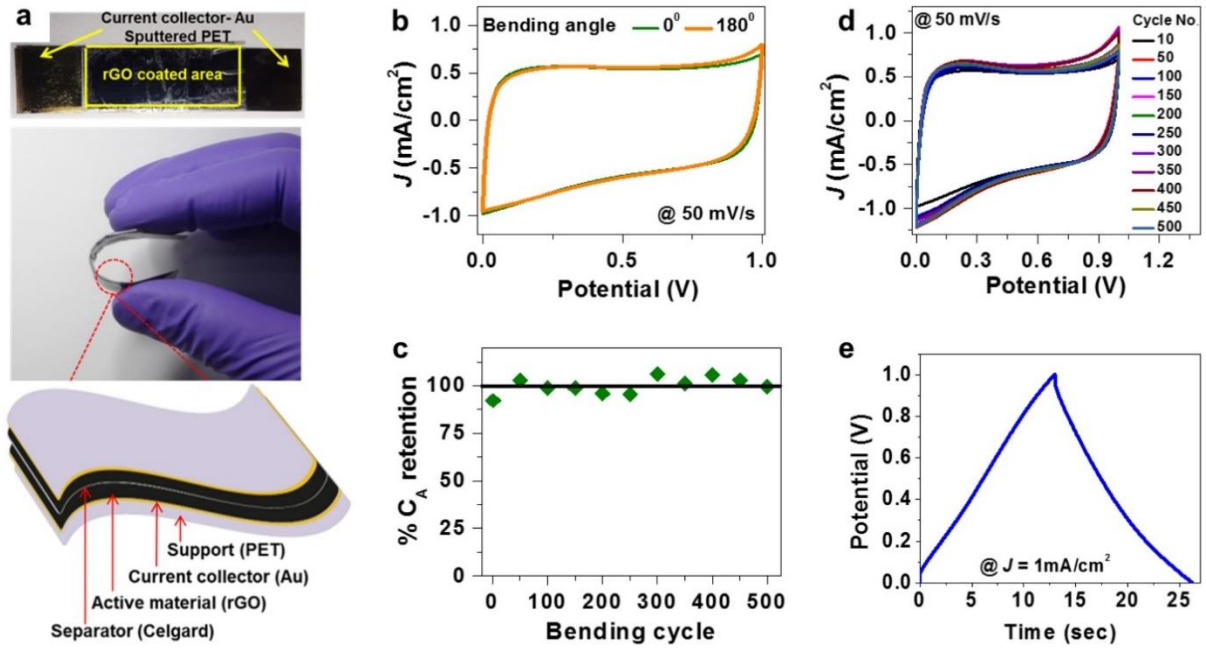

Figure 2.9. *(a) Optical photographs and schematic presentation of an all solid-state flexible rGO supercapacitor. (b) CV plots at two different bending angles of 0° and 180°. (c-d) 500 bending cycles and CV recorded at a scan rate of 50 mV/s and (e) CD of rGO all solid-state flexible supercapacitor at a current density of 1 mA/cm^2.*

Such a high value of capacitance exhibited by our synthesized rGO material now raises the question, why? For the superior supercapacitor performance of rGO produced using $FeCl_2$/HCl, healing of defects in the rGO by intramolecular cross-dehydrogenative coupling induced by $FeCl_3$, as shown in Figure 2.10c, could play a major role.[34] In our approach, GO reduction by $FeCl_2$/HCl is relatively slow, which allows the produced Fe(III) in the reaction mixture to heal the defects, up to a certain extent and thus, leading to a healed rGO with optimally balanced physicochemical properties. However, such healing process of rGO in the course of GO reduction does not appear to be feasible in the case of conventional (and stronger) reducing agents such as N_2H_4 owing to their faster reaction kinetics and irreversible side product

formation.[34] For further investigation of the formation of optimally healed rGO we have performed several control experiments, (1) the reduction process was terminated 12 hr before the optimum duration i.e., 24 hr (rGO -12 hr = rGO1), and (2) the reduction process was continued for 48 hr beyond the optimum duration of 24 hr (rGO + 48 hr = rGO2). Interestingly, the surface area was decreased in the following order: rGO1 > rGO > rGO2 (~263 > ~229 > ~209 m^2/g, respectively) (Figure 2.10d) and the trend in conductivity values was found to be rGO1 (~340 S/m) < rGO (~500 S/m) > rGO2 (~420 S/m) (Figure 2.10d). These values of porosity and conductivity, in turn, affected the capacitance values as follows: significant increase from rGO1 (~147 F/g) to rGO (~171 F/g) (Figure 2.10d), however, from rGO to rGO2 (176 F/g, Figure 2.10d), no appreciable increment was observed. In the beginning, only Fe(II) was present in the reaction mixture, which was oxidized to Fe(III) in the course of reaction with simultaneous GO reduction. This Fe(III) is thus anticipated to heal the defects in rGO with parallel reduction to Fe(II), resulting in a mixture of Fe(III) and Fe(II) in the filtrate (Figures 2.10a, b). Therefore, the reduction and healing processes are presumed to occur simultaneously. Since the reduction kinetics are slow, simultaneous reduction and healing took ~24 hr to produce optimally healed rGO. Also, after 24 hr of GO reduction, the Fe(III)/Fe(II) ratio was found to be low, suggesting that the amount of Fe(II) in the filtrate was adequate to reduce another feed of GO. To further support our evidence of the healing process, after 24 hr of GO reduction by $FeCl_2$/HCl, $FeCl_3$ was deliberately added extrinsically into the reaction mixture and it was left to react for the next 48 hr (rGO + $FeCl_3$ + 48 hr = rGO3). Surface area (~84 m^2/g) and capacitance value (~145 F/g) of rGO3 decreased noticeably, however, the conductivity increased significantly (625 S/m) (Figure 2.10d).[34]

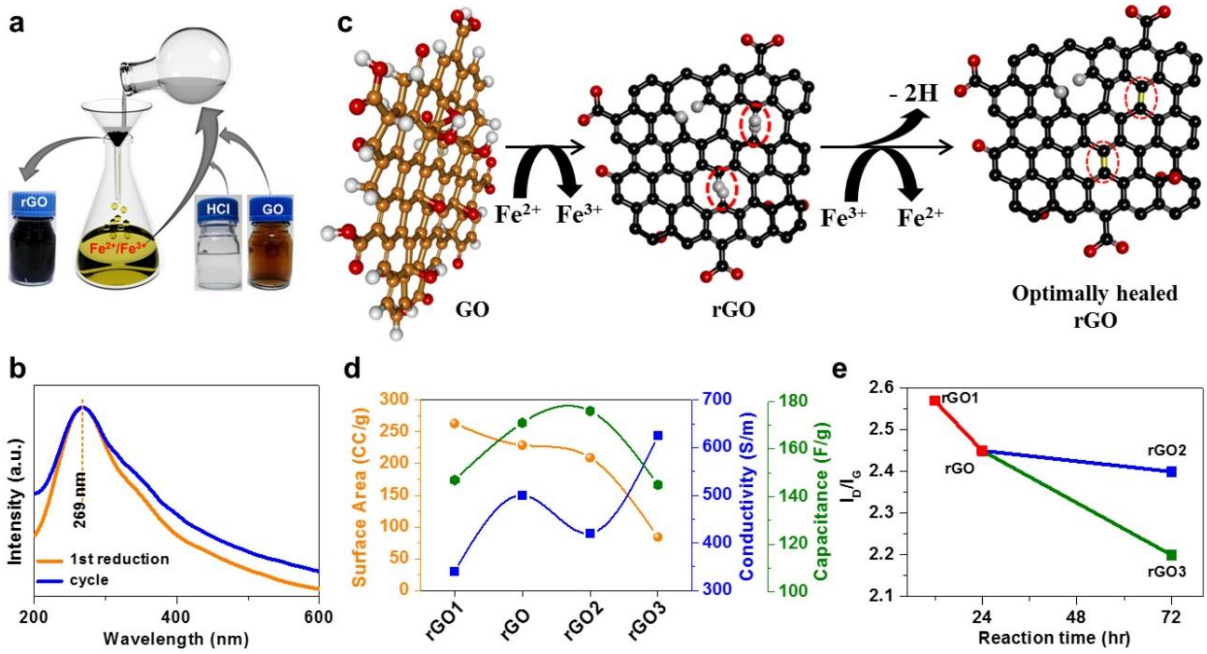

Figure 2.10. *(a) Recycling of the reducing agent for the subsequent reduction feeds of GO. (b)UV-vis spectra of rGO on 1st batch and recycled batch. (c) Reduction of GO to rGO and proposed defect healing mechanism of rGO (red dashed circles). (d) BET surface area, electrical conductivity, and C_G plots of rGO1, rGO, rGO2, and rGO3 and (e) I_D/I_G ratios of rGO1, rGO, rGO2, and rGO3 support the defect-healing mechanism (respective Raman spectra can be seen in reference relevant to this chapter).*

Apart from the BET surface area and electrical conductivity data analysis, Raman measurements of various rGO samples (rGO, rGO1, rGO2, and rGO3) were performed to reinforce the defect-healing mechanism (Figure 2.10e). Indeed, the I_D/I_G ratio decreased from rGO1 to rGO3 (Figure 2.10e) and the trend rGO1 < rGO < rGO2 < rGO3 is consistent with the healing process in rGO discussed earlier. Overall, the non-conventional reducing agent, $FeCl_2$/HCl seems to be a promising candidate for the production of optimally healed and high-quality rGO with striking supercapacitance performance in the domain of chemically reduced pure rGO.

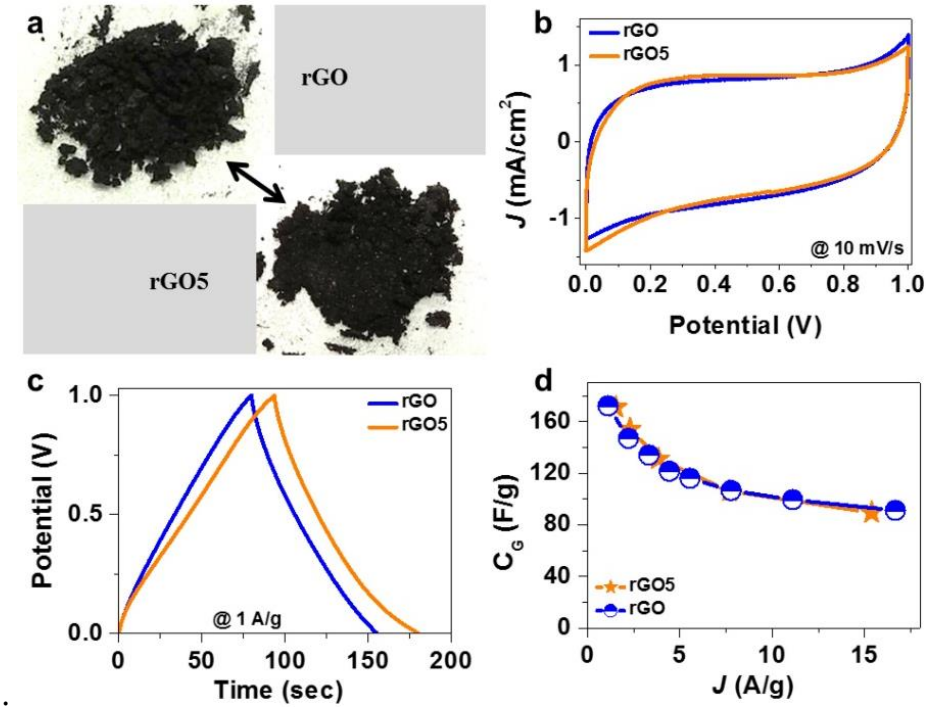

Figure 2.11. *(a) Optical photographs of rGO and rGO5. (b-c) CV and CD plots of rGO and rGO5 and (d) comparison of C_G of rGO and rGO5 at different current densities.*

Also, our experiments suggest that such defect healing of rGO is also possible with other transition metal salts, e.g., $MnCl_2$. Furthermore, to exemplify the efficacy of the recycling process, fresh rGO material (named as rGO5) was prepared using the recycled reducing agent and the supercapacitor performance of rGO5 was found to be similar to that of rGO (prepared from fresh reducing agent) (Figures 2.11a-d). Specifically, the gravimetric capacitance of rGO5 was found to be ~170 F/g at a current density of 1.5 A/g.

To further enhance the potential window in supercapacitor applications and the high energy and power densities values, we wanted to showcase the capacitive performance of our as-synthesized rGO material in the most common and commercially available organic electrolyte $TEABF_4$/AN. The CV plots were recorded at various scan rates ranging from 5 to 1,000 mV/s (Figures 2.12a) consistently showing partial rectangular features, which suggested EDLC characteristic of our rGO in the organic electrolyte. Also, the CD (Figure 2.12b) curves measured at different current densities (2-60 mA/cm^2) exhibited symmetrical triangular features complementing the CV data. Along with low IR drop in CD, the Nyquist plot showed R_S ~7.4 Ω with a nearly vertical spur in the low frequency regime resembling ideal capacitive behaviour (Figure 2.12c). From Bode phase plot time constant can be estimated to be ~ 2.5 sec which is noteworthy (Figure 2.12d). The areal and gravimetric capacitance values of rGO were

estimated to be ~310 mF/cm^2 and ~282 F/g at 2 mA/cm^2 and 1.8 A/g current densities, respectively (Figure 2.12e). The maximum energy and power densities of rGO was calculated to be ~59.6 Wh/kg (at J ~ 1.8 A/g) and ~2.7x10^4 W/kg (at J ~ 54 A/g), respectively (Figure 2.12f). Such numbers seem to be record values in the domain of rGO-only materials obtained by simple chemical reductions and clearly hold promise for ultrahigh performance all-organic all solid-state supercapacitor applications.[7,22,35]

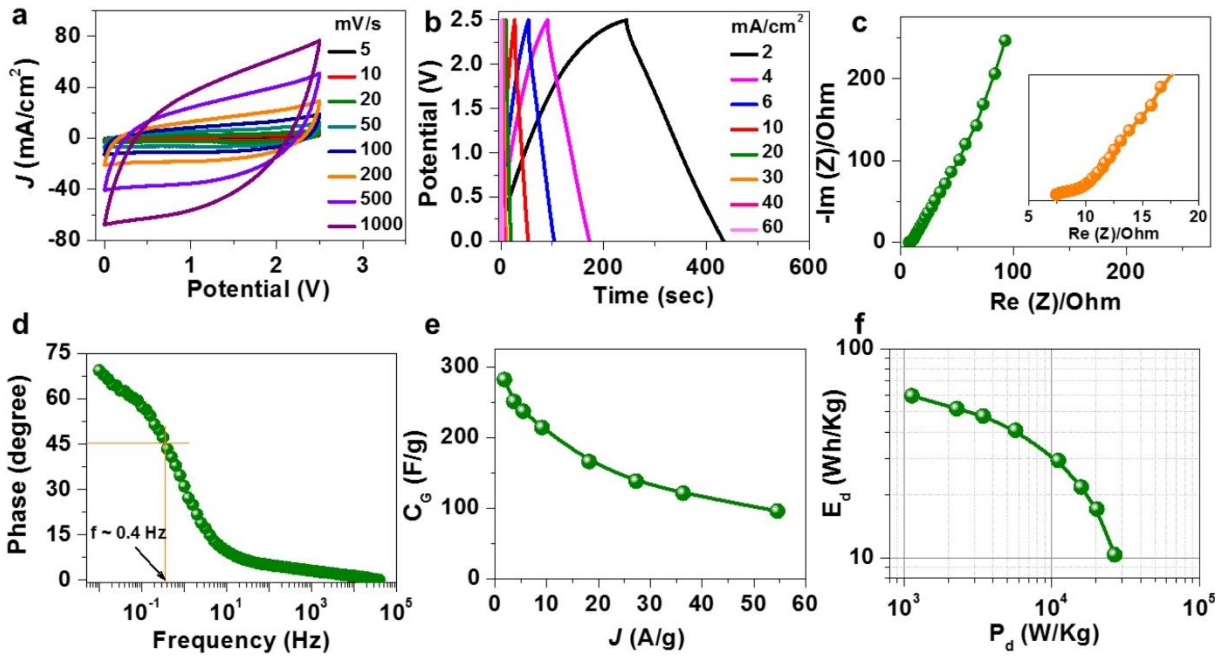

Figure 2.12. *(a-f) CV, CD, Nyquist, Bode phase, current density versus specific capacitance and Ragone plots of rGO in organic electrolyte TEABF$_4$/AN.*

2.4. Conclusions

An effective chemical reduction of rGO was realised with an electrical conductivity and surface area of ~500 S/m and ~229 m^2/g, respectively. Moreover, the reducing agent can be easily recycled and used for subsequent feeds of GO reduction. The fabricated all-solid-state supercapacitors of rGO exhibited high capacitance (C_A ~ 156 mF/cm^2 and C_G ~ 171 F/g), and high energy and power densities ~2.4 Wh/kg and ~5.7 kW/kg, respectively. The rGO sustained remarkable CD cycle over 100,000 cycles of continued operation (>80% retention of capacitance and ~100% retention of Coulombic efficiency). Also, fabricated flexible supercapacitor of the prepared rGO demonstrated the potential application. The obtained superior supercapacitor performance was attributed to optimally balanced porosity and conductivity in rGO as well as defect healing of rGO via intramolecular cross-dehydrogenative coupling induced by Fe(III). Supercapacitor of rGO in organic electrolyte performed remarkably where capacitance value (~282 F/g at ~1.8 A/g current density) as well as energy and power density values (~59.6 Wh/kg and ~$2.7x10^4$ W/kg, respectively) were boosted. The control synthesis of rGO with optimized physicochemical properties opens up new possibilities for the production of rGO on an industrial scale with satisfying the needs of high-performance energy-storage devices.

2.5. References

(1) Chua, C. K.; Pumera, M. Chemical Reduction of Graphene Oxide: A Synthetic Chemistry Viewpoint. *Chem. Soc. Rev.* **2014**, *43*, 291-312.

(2) Gao, W.; Alemany, L. B.; Ci, L.; Ajayan, P. M. New Insights into the Structure and Reduction of Graphite Oxide. *Nat. chem.* **2009**, *1*, 403.

(3) Lei, Z.; Zhang, J.; Zhang, L. L.; Kumar, N. A.; Zhao, X. S. Functionalization of Chemically Derived Graphene for Improving Its Electrocapacitive Energy Storage Properties. *Energy Environ. Sci.* **2016**, *9*, 1891-1930.

(4) Lee, J. H.; Park, N.; Kim, B. G.; Jung, D. S.; Im, K.; Hur, J.; Choi, J. W. Restacking-Inhibited 3D Reduced Graphene Oxide for High Performance Supercapacitor Electrodes. *ACS Nano* **2013**, *7*, 9366-9374.

(5) Choi, B. G.; Hong, J.; Hong, W. H.; Hammond, P. T.; Park, H. Facilitated Ion Transport in All-Solid-State Flexible Supercapacitors. *ACS Nano* **2011**, *5*, 7205-7213.

(6) Liu, Y.; Li, Y.; Zhong, M.; Yang, Y.; Yuefang, W.; Wang, M. A Green and Ultrafast Approach to the Synthesis of Scalable Graphene Nanosheets with Zn Powder for Electrochemical Energy Storage. *J. Mater. Chem.* **2011**, *21*, 15449-15455.

(7) Stoller, M. D.; Park, S.; Zhu, Y.; An, J.; Ruoff, R. S. Graphene-Based Ultracapacitors. *Nano Lett.* **2008**, *8*, 3498-3502.

(8) Wang, Y.; Chen, J.; Cao, J.; Liu, Y.; Zhou, Y.; Ouyang, J.-H.; Jia, D. Graphene/Carbon Black Hybrid Film for Flexible and High Rate Performance Supercapacitor. *J. Power Sources* **2014**, *271*, 269-277.

(9) Yao, X.; Zhao, Y. Three-Dimensional Porous Graphene Networks and Hybrids for Lithium-Ion Batteries and Supercapacitors. *Chem* **2017**, *2*, 171-200.

(10) Shao, Y.; El-Kady, M. F.; Lin, C. W.; Zhu, G.; Marsh, K. L.; Hwang, J. Y.; Zhang, Q.; Li, Y.; Wang, H.; Kaner, R. B. 3D Freeze-Casting of Cellular Graphene Films for Ultrahigh-Power-Density Supercapacitors. *Adv. Mater.* **2016**, *28*, 6719-6726.

(11) Fan, Z.-J.; Kai, W.; Yan, J.; Wei, T.; Zhi, L.-J.; Feng, J.; Ren, Y.-m.; Song, L.-P.; Wei, F. Facile Synthesis of Graphene Nanosheets Via Fe Reduction of Exfoliated Graphite Oxide. *ACS Nano* **2011**, *5*, 191-198.

(12) Chua, C. K.; Pumera, M. Reduction of Graphene Oxide with Substituted Borohydrides. *J. Mater. Chem. A* **2013**, *1*, 1892-1898.

(13) Chua, C. K.; Ambrosi, A.; Pumera, M. Graphene Oxide Reduction by Standard Industrial Reducing Agent: Thiourea Dioxide. *J. Mater. Chem.* **2012**, *22*, 11054-11061.

(14) Ferrari, A. C.; Robertson, J. Interpretation of Raman Spectra of Disordered and Amorphous Carbon. *Phys. Rev. B* **2000**, *61*, 14095-14107.

(15) Moon, I. K.; Lee, J.; Ruoff, R. S.; Lee, H. Reduced Graphene Oxide by Chemical Graphitization. *Nat. Commun.* **2010**, *1*, 73.

(16) Wang, G.; Sun, X.; Lu, F.; Sun, H.; Yu, M.; Jiang, W.; Liu, C.; Lian, J. Flexible Pillared Graphene-Paper Electrodes for High-Performance Electrochemical Supercapacitors. *Small* **2012**, *8*, 452-9.

(17) Abdelkader, A. M.; Vallés, C.; Cooper, A. J.; Kinloch, I. A.; Dryfe, R. A. W. Alkali Reduction of Graphene Oxide in Molten Halide Salts: Production of Corrugated Graphene Derivatives for High-Performance Supercapacitors. *ACS Nano* **2014**, *8*, 11225-11233.

(18) Groen, J. C.; Peffer, L. A. A.; Pérez-Ramírez, J. Pore Size Determination in Modified Micro- and Mesoporous Materials. Pitfalls and Limitations in Gas Adsorption Data Analysis. *Micropor. Mesopor. Mat.* **2003**, *60*, 1-17.

(19) Xue, Y.; Chen, H.; Yu, D.; Wang, S.; Yardeni, M.; Dai, Q.; Guo, M.; Liu, Y.; Lu, F.; Qu, J., *et al.* Oxidizing Metal Ions with Graphene Oxide: The in Situ Formation of Magnetic Nanoparticles on Self-Reduced Graphene Sheets for Multifunctional Applications. *Chem. Commun.* **2011**, *47*, 11689-91.

(20) Pearson, R. G. Hard and Soft Acids and Bases. *J. Am. Chem. Soc.* **1963**, *85*, 3533-3539.

(21) Bard, A. J., Faulkner, Larry R. *Electrochemical Methods : Fundamentals and Applications* Wiley: New York, 1980.

(22) Zhong, C.; Deng, Y.; Hu, W.; Qiao, J.; Zhang, L.; Zhang, J. A Review of Electrolyte Materials and Compositions for Electrochemical Supercapacitors. *Chem. Soc. Rev.* **2015**, *44*, 7484-7539.

(23) El-Kady, M. F.; Strong, V.; Dubin, S.; Kaner, R. B. Laser Scribing of High-Performance and Flexible Graphene-Based Electrochemical Capacitors. *Science* **2012**, *335*, 1326-1330.

(24) Augustyn, V.; Come, J.; Lowe, M. A.; Kim, J. W.; Taberna, P.-L.; Tolbert, S. H.; Abruña, H. D.; Simon, P.; Dunn, B. High-Rate Electrochemical Energy Storage through Li^+ Intercalation Pseudocapacitance. *Nat. Mater.* **2013**, *12*, 518-522.

(25) Mourad, E.; Coustan, L.; Lannelongue, P.; Zigah, D.; Mehdi, A.; Vioux, A.; Freunberger, S. A.; Favier, F.; Fontaine, O. Biredox Ionic Liquids with Solid-Like Redox Density in the Liquid State for High-Energy Supercapacitors. *Nat. Mater.* **2016**, *16*, 446-453.

(26) Gogotsi, Y.; Simon, P. True Performance Metrics in Electrochemical Energy Storage. *Science* **2011**, *334*, 917-918.

(27) Yuan, K.; Xu, Y.; Uihlein, J.; Brunklaus, G.; Shi, L.; Heiderhoff, R.; Que, M.; Forster, M.; Chassé, T.; Pichler, T., *et al.* Straightforward Generation of Pillared, Microporous Graphene Frameworks for Use in Supercapacitors. *Adv. Mater.* **2015**, *27*, 6714-6721.

(28) Lei, Z.; Christov, N.; Zhao, X. S. Intercalation of Mesoporous Carbon Spheres between Reduced Graphene Oxide Sheets for Preparing High-Rate Supercapacitor Electrodes. *Energy Environ. Sci.* **2011**, *4*, 1866-1873.

(29) Yang, X.; Cheng, C.; Wang, Y.; Qiu, L.; Li, D. Liquid-Mediated Dense Integration of Graphene Materials for Compact Capacitive Energy Storage. *Science* **2013**, *341*, 534-537.

(30) Chen, J.; Sheng, K.; Luo, P.; Li, C.; Shi, G. Graphene Hydrogels Deposited in Nickel Foams for High-Rate Electrochemical Capacitors. *Adv. Mater.* **2012**, *24*, 4569-4573.

(31) Dreyer, D. R.; Murali, S.; Zhu, Y.; Ruoff, R. S.; Bielawski, C. W. Reduction of Graphite Oxide Using Alcohols. *J. Mater. Chem.* **2011**, *21*, 3443-3447.

(32) Kumar, N. A.; Togami, M.; Oishi, Y.; Tominaga, M.; Takafuji, M.; Ihara, H. Iron Metal Induced Deoxygenation of Graphite Oxide Nanosheets-Insights on the Capacitive Properties of Binder-Free Electrodes. *RSC Adv.* **2015**, *5*, 23367-23373.

(33) Fan, L.-Z.; Liu, J.-L.; Ud-Din, R.; Yan, X.; Qu, X. The Effect of Reduction Time on the Surface Functional Groups and Supercapacitive Performance of Graphene Nanosheets. *Carbon* **2012**, *50*, 3724-3730.

(34) Park, O.-K.; Choi, Y.-M.; Hwang, J. Y.; Yang, C.-M.; Kim, T.-W.; You, N.-H.; Koo, H. Y.; Lee, J. H.; Ku, B.-C.; Goh, M. Defect Healing of Reduced Graphene Oxide Via Intramolecular Cross-Dehydrogenative Coupling. *Nanotechnology* **2013**, *24*, 185604.

(35) Kim, B. C.; Hong, J.-Y.; Wallace, G. G.; Park, H. S. Recent Progress in Flexible Electrochemical Capacitors: Electrode Materials, Device Configuration, and Functions. *Adv. Energy Mater.* **2015**, *5*, 1500959.

Chapter 3

Reduction of Graphene Oxide by $MnCl_2/NH_4OH$ for Supercapacitor Applications

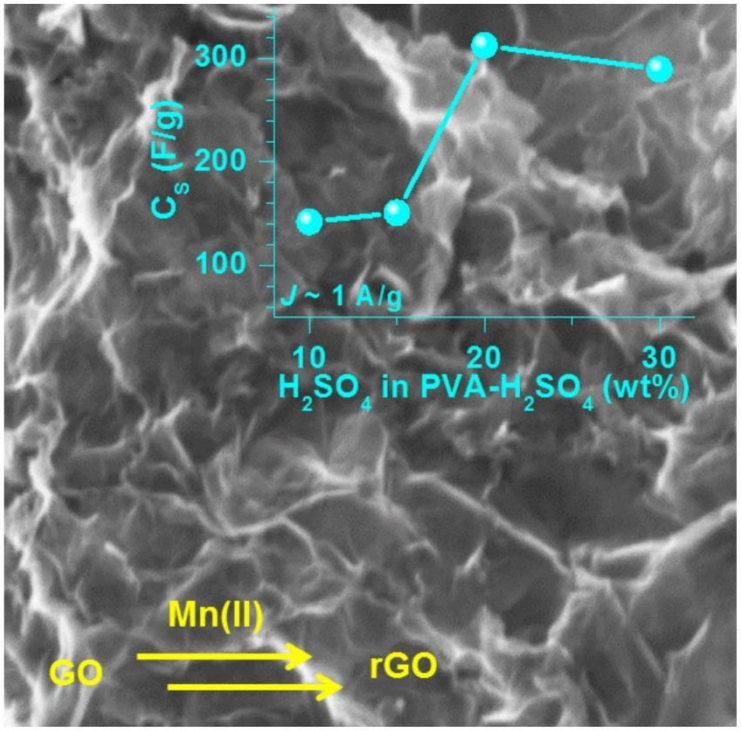

3.1. Introduction

All solid-state supercapacitors are in general comprised of mainly four necessary components: (i) current collector, (ii) active material, (iii) separator, and (iv) electrolyte (solid/quasi-solid, liquid) – deciding parameters on overall performance of the supercapacitor device.[1-5] In the fabrication of solid-state graphene-based supercapacitors, quasi-solid gel polymer electrolytes (GPEs) are extensively involved, due to their higher ionic conductivity compared to solid-polymer electrolytes.[6-7] Among various GPEs, poly(vinyl alcohol)-sulfuric acid (PVA-H_2SO_4) as a GPE is widely accepted in the domain of graphene-based solid-state supercapacitors.[6] Notably, most of the literatures, the concentration of PVA-H_2SO_4 GPE was observed to be 10 wt% (Table 3.2) and raised a question – why? Is such a concentration enough to deliver an optimal capacitance value or a variation of the electrolyte concentration could bring significant change in the overall performance of graphene-based supercapacitors. The capacitance value of rGO crucially depends on the synthetic strategy, specifically the choice of reducing agent in carrying out the graphene oxide (GO) to reduced graphene oxide (rGO) conversion. For example, in chapter-2, rGO produced by a non-conventional reducing agent ($FeCl_2$/HCl) exhibited significantly enhanced supercapacitive performance than rGO produced with conventional reducing agents ($NaBH_4$ and N_2H_4) and thus paving the path for exploration of other transition metal salts possessing variable oxidation states in establishing effective wet-chemical reduction of GO.[3]

In this chapter, for the first time, we have explored Mn(II) salt as the reducing agent for the reduction of GO to rGO and the isolated rGO material exhibited remarkable electrochemical characteristics, employing the aqueous H_2SO_4 as the electrolyte. Motivated by the abovementioned performance, all solid-state supercapacitor devices were fabricated by employing the isolated rGO as such as the active electrode material. Simply varying the concentration of H_2SO_4 in PVA-H_2SO_4 (wt%), significantly affected the capacitive performances of supercapacitors. Specifically, the importance of the safe and eco-friendly aqueous-based electrolytes in modulating the performance of carbonaceous materials including rGO supercapacitors – without involving commercially used flammable and eco-unfriendly organic electrolytes and/or ionic liquids was realised.[4]

3.2. Materials and Method

Manganese(II) chloride ($MnCl_2.4H_2O$) was purchased from Sigma-Aldrich. Hydrofluoric acid (HF) was purchased from RANKEM. Poly(vinyl alcohol) (PVA, n=1700-1800) was purchased from Loba Chemie.

GO synthesis is already explained in chapter 2. GO was centrifuged at 1000 rpm for 5 min to remove multilayers.

In this chapter, rGO was prepared from GO using $MnCl_2$ as the reducing agent in aqueous medium. In a typical synthesis, ~30 mL aqueous $MnCl_2$ (1.8 g) was mixed with ~150 mL GO (~1 mg/mL) in a 500 mL round bottom flask and stirred at 94 °C for ~24 hr. The black colored mixture thus obtained was allowed to cool to room temperature (RT) and then, ~15 mL ammonia solution (25%) was added to it followed by stirring for ~12 hr. The brown-black colored precipitate was filtered and washed with Millipore water (MQ H_2O)/methanol followed by vacuum drying at 150 °C for ~12 hr. In order to remove the excess Mn_3O_4 particles from the composite, first the material was sonicated in acetone and then centrifuged (1500 rpm). The filtrate was decanted and the residue was again sonicated and centrifuged until a colorless filtrate was obtained. The composite was dried under vacuum. To extract the pure rGO out of the rGO-Mn_3O_4 composite, it was soaked in 2 M HF and vigorously stirred for 12 hr at RT. Afterwards, the mixture was filtered, washed with H_2O, methanol, and vacuum dried for 12 hr at 70 °C.

Characterisation of all the materials is as described in chapter 2.

To prepare 5-50 wt% H_2SO_4 in PVA-H_2SO_4 GPE, ~2 g of PVA was mixed in 20 mL of MQ water and stirred at ~80 °C until the solution became clear followed by cooling down to RT. About 0.5, 1, 1.5, 2, 3, 4, and 5 mL concentrated H_2SO_4 was added into above PVA solution to make 5, 10, 15, 20, 30, 40, and 50 wt% of PVA-H_2SO_4, respectively which further continuously stirred at RT. All the hydrogels were air dried and sliced into shapes and connected between two current collectors (Figure 3.6a).

To examine the electrochemical performance in aqueous medium, symmetric rGO coated electrodes were dipped in 0.5 M H_2SO_4 electrolyte. The loading of active material on each electrode was ~1 mg/cm^2.

Fabrication of all solid-state supercapacitors is as described in chapter 2. Active material loading on each electrode was ~1 mg/cm^2.

Fabrication of all solid-state flexible supercapacitors is as described in chapter 2. Active material loading on each electrode was ~1 mg/cm^2 and electrodes were soaked in 20 wt% of H_2SO_4 in PVA-H_2SO_4 GPE.

3.3. Results and Discussion

Figure 3.1 schematically shows the synthesis of rGO by an unconventional reducing agent - $MnCl_2/NH_4OH$, producing rGO-Mn_3O_4 composite which was then treated with hydrofluoric acid (HF) to isolate rGO.

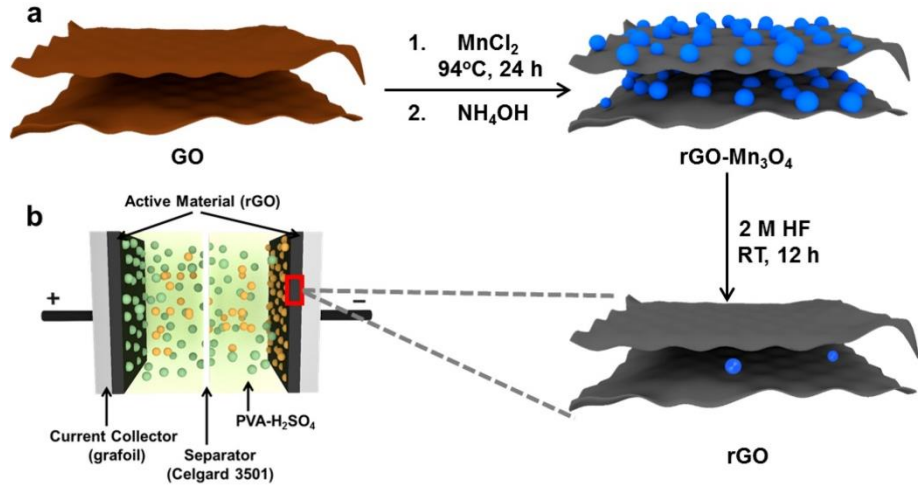

Figure 3.1. *Schematic presentation of (a) rGO synthesis by $MnCl_2/NH_4OH$ reducing agents and (b) All solid-state supercapacitors.*

In the Raman spectra, both D and G bands were observed at ~1352 cm^{-1} and ~1594 cm^{-1}, respectively (Figure 3.2a), for Gr, GO as well as rGO, however, the intensity ratio of D band to G band (I_D/I_G) is lower in the case of rGO, compared to that of GO, suggesting a successful chemical reduction.[8] In the C1s XPS spectrum of rGO, peaks appearing at ~284.8, ~286.3, and ~288.2 eV evinced the presence of C-C, –C-OH and –COO- functional groups while the intensity of peaks at ~286.3 eV and ~288.2 eV reduced significantly compared to that of GO indicating the partial removal of basal oxide/epoxy and peripheral –COOH groups during reduction process and bringing reasonable π-conjugation in the system (Figure 3.2b).[9]

In the FTIR spectra, peak corresponding to C=C was intensified while the C=O peak was suppressed in rGO compared to GO, thereby confirming the reduction and complimenting the Raman and XPS data (Figure 3.2c).[10] In the PXRD patterns, the (002) plane of Gr at $2\theta \approx 26.6°$ was shifted to $2\theta \approx 11.70°$ in GO and eventually decreased to $2\theta \approx 25.1°$ in rGO, however, unlike Gr, the diffraction peak was broad due to the stacking of rGO layer in disordered fashion (Figure 3.2d).[3,11] A small hump at ~18.1° is (101) plane depicts the presence of small amount of Mn ion as Mn_xO_y (discussed later). Further, UV-vis spectrum of rGO displayed the characteristic peak of π-conjugation network at ~270 nm supporting successful reduction of GO to rGO (Figure 3.2e).[12] TGA revealed an impressive thermal stability of rGO with ~10% weight loss (perhaps due to removal of water and other functional groups) upto 200 °C (Figure 3.2f). Beyond 200 °C weight loss is because of the expulsion of stable functional groups (already discussed in chapter 2).[3]

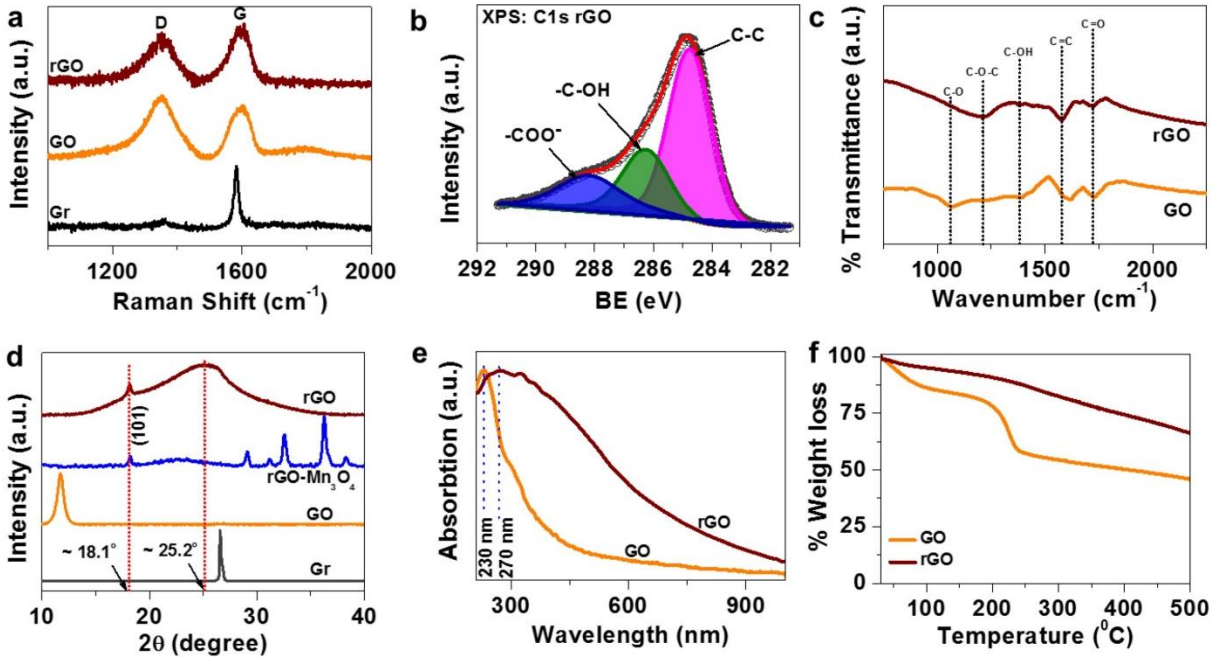

Figure 3.2. *(a) Raman spectra of Gr, GO and rGO show prominent D and G bands. (b) C1s XPS spectra of rGO indicates C-C, –C-OH and –COO^- functional groups. (c) FTIR spectra of GO and rGO depicted essential functional groups. (d) PXRD of Gr, GO, rGO-Mn_3O_4, and rGO. (e-f) UV-vis and TGA of GO and rGO.*

FESEM and TEM images of rGO showed crumbled sheets with larger lateral size depicts the self-assembly due to π-π interaction among sheets also partially validating the successful reduction (Figures 3.3a, b).

The essential properties of rGO for supercapacitor application, such as, porosity and electrical conductivity extracted from BET surface area (rGO powder) and four-probe electrical conductivity (pressed rGO film) were recorded (Figures 3.3c, d). The N_2 adsorption-desorption isotherms of rGO at 77 K reflected mesoporous characteristics (small hysteresis loop)[13] with estimated BET surface area of ~60 m^2/g (pore diameter (d) ranges from ~ 1.5 - 5 nm) (Figure 3.3c). The electrical conductivity of pressed rGO film was found to be ~0.5 S/cm which is comparable to the rGOs reported in literature which are synthesized chemically by conventional reducing agents (Figure 3.3d).[3,14]

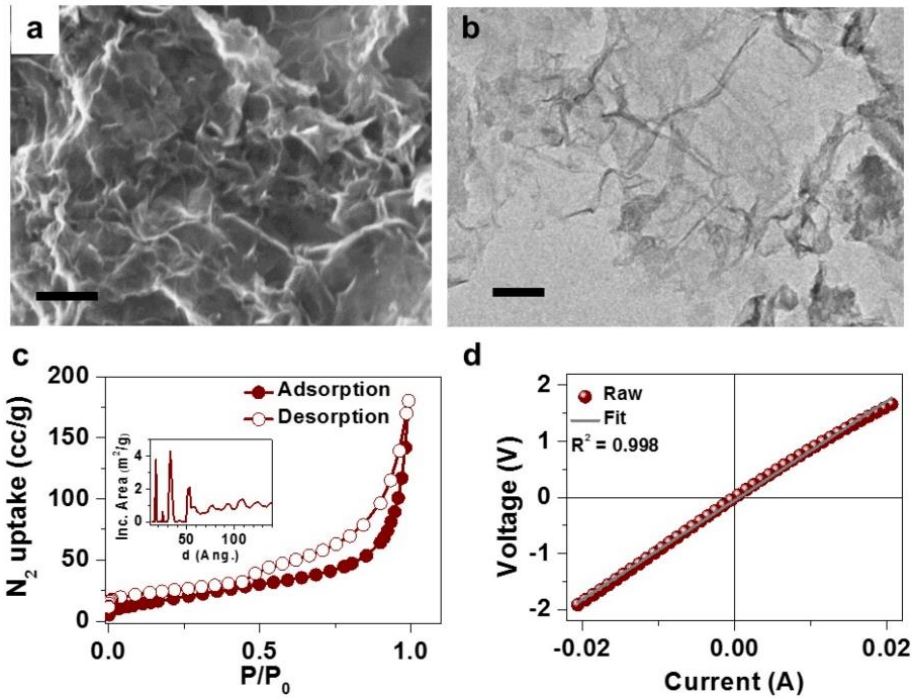

Figure 3.3. *(a-b) FESEM and TEM images of rGO. Scale bars are 500 nm and 100 nm, respectively. (c) N_2 adsorption-desorption isotherms of rGO at 77 K (Inset: curve depicting pore diameter of rGO). (d) Current-Voltage (I-V) characteristics of rGO.*

The electrochemical performance of rGO was evaluated by CV, CD, and EIS techniques. Electrodes were prepared by drop-casting rGO on grafoil sheet and tested in conventional two-electrode setup (Figure 3.4a, aqueous 0.5 M H_2SO_4). CV plots were recorded at scan rates ranging from 10-500 mV/s (Figure 3.4b), where the partial rectangular feature in the CV plots at lower as well as higher scan rates resemble ideal EDLC behavior of rGO. Also, the CD plots were recorded at varied current densities starting from 0.5 to 20 A/g (Figure 3.4c) exhibiting triangular nature, indicating the EDLC formation between rGO and electrolyte corroborating to the CV data.

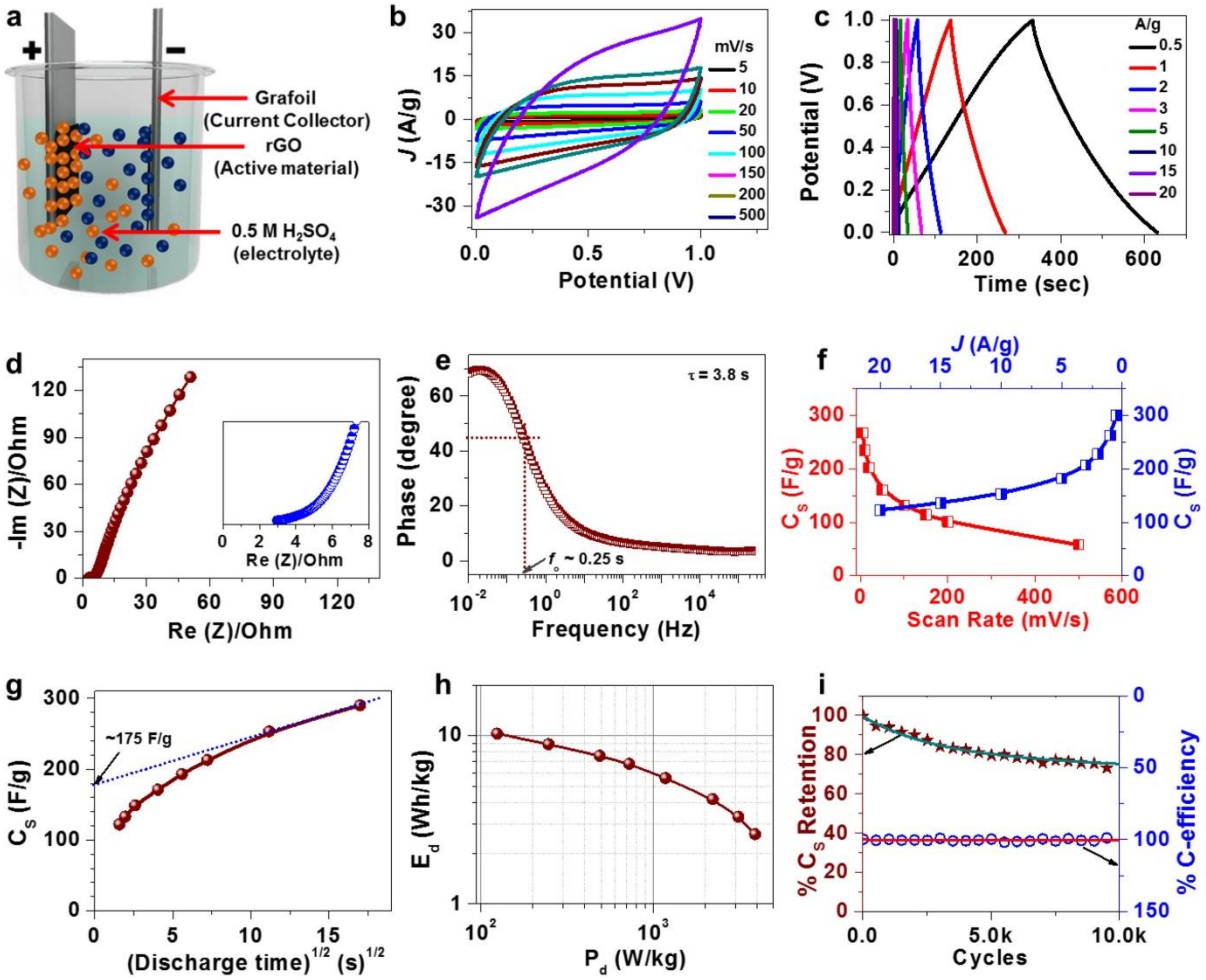

Figure 3.4. *(a) Schematic representation of two electrode setup in 0.5 M H_2SO_4 solution. (b-e) CV, CD, Nyquist, and Bode phase plot of rGO. (Figure c inset: zoomed-in plot of Nyquist at high frequency region). (f) C_S of rGO against current density and scan rate. (g) C_S versus (discharge time)$^{1/2}$ plot of rGO. (h-i) Ragone plot and durability test (at a current density of 15 A/g) of rGO.*

Further, Nyquist plot was recorded to estimate the R_S and R_{CT} behavior of rGO (Figure 3.4d). The R_S value of rGO was found to be ~2.95 Ω with a small semicircle at high frequency region indicating negligible R_{CT} with a plot nearly parallel to the y-axis implying the EDLC behavior at low frequency (Figure 3.4d). [3,15] From Bode phase plot the time constant value was found to be ~3.8 sec (Figure 3.4e). Specific capacitance (C_S) of rGO was calculated from CV as well as CD measurements and plotted against scan rates and current densities (Figure 3.4f) revealing the capacitance of rGO to be ~235 F/g at a scan rate of 10 mV/s and ~265 F/g at a current density of 1 A/g which are comparably higher than the rGOs produced by wet-chemical synthesis using conventional reducing agents (Table 3.1). An impressive C_S value ~120 F/g was also maintained at a higher current density of 20 A/g which is remarkable and showcase

the quality and stability of our rGO (Figure 3.4f). The rate independent capacitance value of rGO supercapacitor ~175 F/g is significantly high (Figure 3.4g). Ragone plot revealed the energy (E_d) and power (P_d) densities to be ~10 Wh/kg and ~125 W/kg respectively at a current density of 0.5 A/g. At higher current density (20 A/g) the E_d and P_d values were found to be ~2.6 Wh/kg and ~3.9 kW/kg, respectively (Figure 3.4h). Finally, in this configuration, rGO was subjected to 10,000 continued CD cycles at a relatively higher current density of 15 A/g and >70% retention of C_S along with 100% retention of coulombic efficiency was observed (Figure 3.4i). Overall performance of our rGO is comparable to other reported rGO (produced by conventional reducing agents) supercapacitors (Table 3.1).

Table 3.1. *Comparative assesment of rGO based supercapacitor in H_2SO_4 electrolyte.*

S.N	Materials (reduction)	Electrode (Aqu.)	H_2SO_4	Capacitance	Cycles	Stability	Ref.
1	**rGO**	**2-electrode**	**0.5 M**	**~265 F/g @ 1 A/g**	**10000 @ 15 A/g**	**>70%**	**Our Work**
2	3D-GFs	3-electrode	1 M	226 F/g @ 1 mV/s	5000 @ 2 A/g	100%	[16]
3	rGO by N_2H_4	3-electrode	1 M	116 F/g @ 1 A/g	---	---	[17]
4	rGO by HBr	3-electrode	1 M	348 F/g @ 0.2 A/g	3000 @ 10 mV/s	100%	[18]
5	rGO by Microwave	3-electrode	1 M	82 F/g @ 0.5 F/g	---	---	[19]
6	Graphene by Trigol	2-electrode	0.5	130 F/g @ 1 A/g	10000 @ 10 A/g	85%	[20]
7	Functionalized graphene	3-electrode	1 M	225 F/g @ 1 A/g	2000 @ 0.5 A/g	100%	[21]
8	Graphene hydrogels by N_2H_4	3-electrode	1 M	225 F/g @ 1 A/g	2000 @ 10 A/g	100%	[22]
9	Single-layer-porous graphene-	2-electrode	1 M	154 F/g @ 0.5 A/g	1000 @ 2 A/g	>75%	[23]

An impressive electrochemical performance of rGO produced by Mn(II) in 0.5 M H_2SO_4 solution motivated us to employ it for solid-state supercapacitor applications for which we fabricated all solid-state supercapacitor of rGO and used 10 wt% PVA-H_2SO_4 as GPE (Figure 3.5). The CV plots recorded at different scan rates starting from 5 to 500 mV/s possessed partial rectangular feature substantiating the EDLC involving rGO (Figure 3.5a). The consistency of this rectangular feature even at higher scan rate (500 mV/s) reflected the stability and presence of efficient percolation paths for ions in the active material. The CD plots were recorded at various current densities ranging from 0.5 to 25 A/g (Figure 3.5b), where, triangular feature and low potential drop (IR drop) at lower current density suggested efficient EDLC and low resistant percolation path for the ions in the system, respectively (Figure 3.5b).

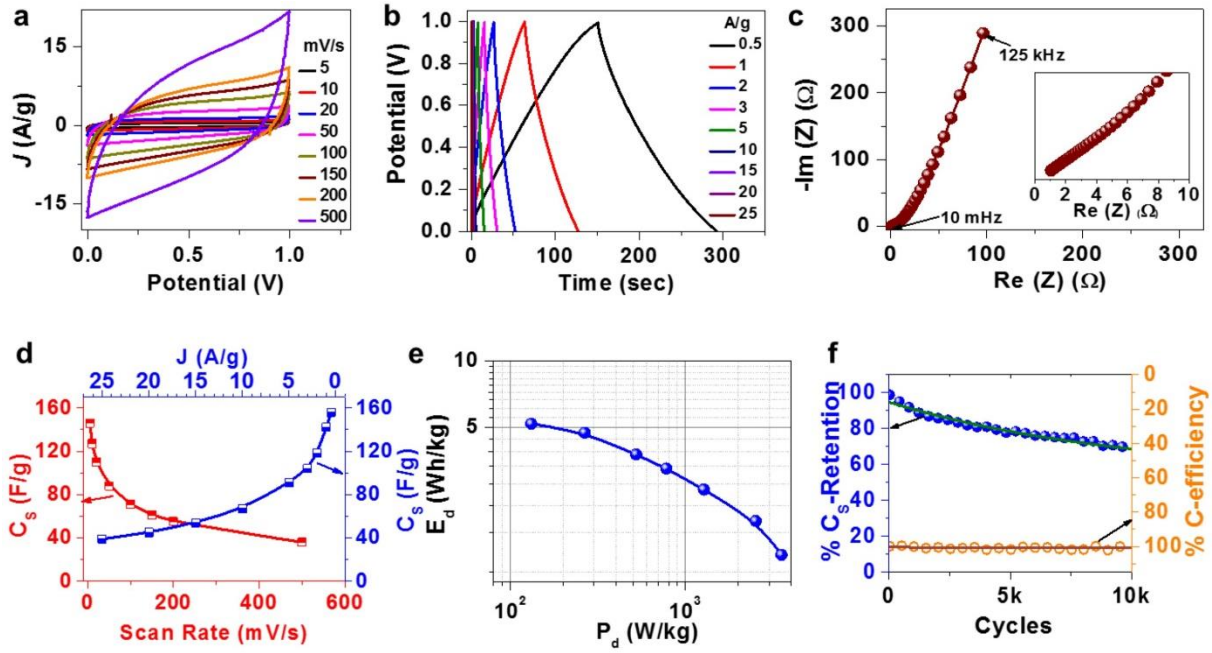

Figure 3.5. *(a-c) CV, CD, and Nyquist (inset: zoomed-in) plot, (d) C_S plotted against different scan rates and current densities, and (e-f) Ragone plot and durability plots (at a current density of 15 A/g) of rGO all solid-state supercapacitors in 10 wt% PVA-H_2SO_4 GPE.*

The CV and CD characteristics were complemented by Nyquist plots where ESR was found to be ~1 Ω and again low-frequency region of the Nyquist plot was almost parallel to y-axis likewise our previous measurements in 0.5 M H_2SO_4 supercapacitor configuration supporting EDLC formation (Figure 3.5c). The specific capacitance values of rGO from CV and CD plots were calculated to be ~130 F/g and ~140 F/g at a scan rate of 10 mV/s and current density of 1 A/g, respectively (Figure 3.5d). Even at very high current density of 25 A/g the capacitance

retention was up to 30% which is noteworthy (Figure 3.5d). From the Ragone plot the E_d and P_d values were estimated to be as high as ~5.2 Wh/kg and ~3.5 kW/kg, respectively (Figure 3.5e). Supercapacitor was finally subjected for 10,000 continued CD cycles at a high current density of 15 A/g. Notably, more than 70% retention of C_S was observed (Figure 3.5f). Thus, all solid-state supercapacitor performance of rGO obtained from Mn(II) salt, as the reducing agent, appears to be as good as those of rGO produced by conventional reducing agents as well as $FeCl_2$/HCl system recently developed by us.[3] A comparative assessment of the overall performance of various rGO-based (without composite formation) solid-state supercapacitors is presented in Table 3.2. Looking at the difference in electrochemical performance of rGO in aqueous as well as 10 wt% PVA-H_2SO_4 raises a question, how desirable is the 10 wt% PVA-H_2SO_4 in rGO based supercapacitor applications?

At this stage, we must address the compositional role of GPE in influencing the electrochemical performance, an attempt was made and all solid-state supercapacitor was assembled with varied wt% of PVA-H_2SO_4. Certainly, higher acid concentration impose two prime issues: (1) whether such concentrations of PVA-H_2SO_4 are acceptable to construct user-friendly all solid-state supercapacitors, and (2) if yes, then what about the material stability? It is well known that supercapacitors are environmental friendly due to its non-toxic and perishable ingredients. We therefore, carefully increased the concentration of H_2SO_4 from ~0.4 M to ~2.4 M. In fact, five batches of solid-state supercapacitors of rGO were successfully fabricated by varying the weight percentage of H_2SO_4 in PVA-H_2SO_4: 5 wt%, 10 wt%, 15 wt%, 20 wt%, and 30 wt%. The CV, CD, and Nyquist plots of all the above mentioned rGO supercapacitors were methodically recorded and compared (Figure 3.6). Interestingly, in CV, the area under the curve/current densities of rGO supercapacitors found to be different in different electrolyte followed the trend of 30 wt% ≈ 20 wt% >> 15 wt% ≈ 10 wt% >> 5 wt% of PVA-H_2SO_4 (Figure 3.6a). Similar trend was observed in CD plots as the discharge time was maximum in case of 20 wt% and minimum in 5 wt% of PVA-H_2SO_4 (Figure 3.6b).

Table 3.2. *Comparison of rGO all Solid-State supercapacitor in wt% PVA-H_2SO_4 GPE.*

S.N	Materials	Electrode setup	Electrolyte H_2SO_4 in PVA-H_2SO_4	Capacitance	Durability	Stability	Ref.
rGO		**Solid**	**10 wt%**	**140 F/g @ 1 A/g**	**10000 @ 15 A/g**	**>70%**	**Our Work**
			20 wt%	**310 F/g @ 1 A/g**			
		Solid and Flexible	**20 wt%**	**120 F/g @ 0.2 A/g**	**30000 @ 15 A/g**	**100%**	
1	rGO	Solid	10 wt%	~170 F/g @ 1.1 A/g	100k @ 22 A/g	>80%	[3]
2	G-gel films	Solid	10 wt%	186 F/g @ 1 A/g	10000 @ 10 A/g	92%	[24]
3	Holey-G frameworks	Solid	10 wt%	201 F/g @ 1 A/g	--	--	[25]
4	G/PPy	Solid	10 wt%	107 mF cm^{-2} @ 0.24 mA cm^{-2}	--	--	[26]
5	rGO/PANI/rGO	Solid	10 wt%	122 mF cm^{-2} @ 0.2 $mAcm^{-2}$	10k @ 10 A/g	85%	[27]
6	Cellulose nanofiber–G	Solid	10 wt%	203 F/g @ 0.7 mA cm^{-2}	5k @ 3.4 mA cm^{-2}	99%	[28]
7	Porous G on carbon cloth	Solid	10 wt%	184.36 F/g @5 mV s^{-1}	1000 @ 2 A/g	>95%	[29]
8	RuO_2–IL-CMG composite film	Solid	10 wt%	166 F/g @ 1 A/g	2000 @ 1 A/g	95%	[30]
12	rGO/CB	Solid	10 wt%	110 F/g @ 5 mV/s	5000 @ 0.58 A/g	96%	[31]
14	PVA-G	Solid	10 wt%	124 F/g @ 1 A/g	---	---	[32]

G → graphene; PPy → polypyrrole

In Nyquist plot, the R_S of all four supercapacitors was found to be in between 0.8-2 Ω, except for 5 wt% H_2SO_4 in PVA-H_2SO_4 where the value was relatively high (Figure 3.6c). Such high R_S value of rGO in 5 wt% GPE actually indicated the inferior capacitive behavior of the same rGO material in solid-state device. The 5 wt% H_2SO_4 in PVA-H_2SO_4 contains ~0.4 M H_2SO_4, which may not be adequate to form EDL with rGO. Therefore, the C_S, E_d, P_d, and durability were recorded and compared only for other four rGO supercapacitors (10, 15, 20 and 30 wt%) (Figures 3.6d-f). Capacitance obtained for 10 wt% and 15 wt% was comparable, however, as soon concentration increases to 20 wt%, the specific capacitance value become doubled compared to 10 wt% suggest significant effect of H^+ and SO_4^{2-} for enhancing the supercapacitance value (Figure 3.6d). Also, increment from 20 to 30 wt% of GPE concentration did not enhance the capacitance values much, instead realized to be saturated (Figure 3.6d). And at this point, if we compare the performance of rGO in aqueous 0.5 M H_2SO_4 and solid-state 20 wt% H_2SO_4 in PVA-H_2SO_4 GPE systems, the capacitance values are almost identical, altogether suggesting the importance of choosing an optimal concentration of GPE.

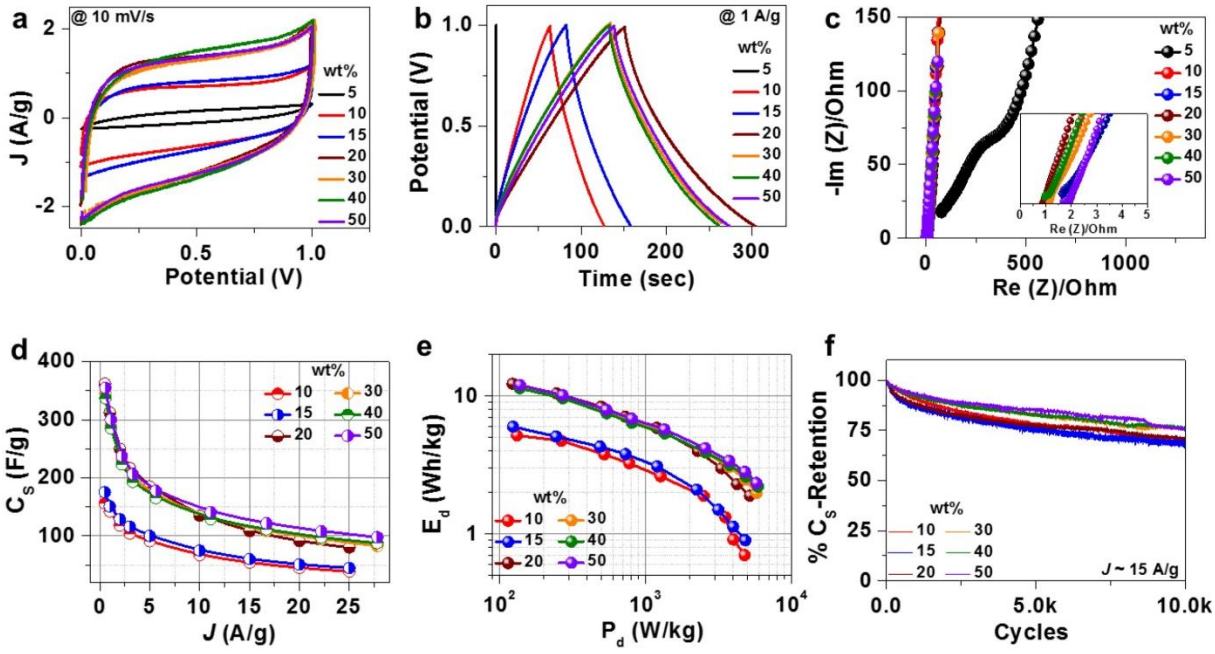

Figure 3.6. *Comparative assessment of rGO supercapacitor in 5, 10, 15, 20, 30, 40, and 50 wt% H_2SO_4 in PVA-H_2SO_4 GPE: (a) CV plots at 10 mV/s, (b) CD plots at 1 A/g, (c) Nyquist plots (inset: Zoomed in Nyquist plot), (d) Specific capacitance versus current density plots, (e) Ragone plot, and (f) Durability test.*

Finally, we have compared the E_d and P_d values of rGO supercapacitors and the trends were similar as above: 30 wt% ≈ 20 wt% >> 15 wt% ≈ 10 wt% H_2SO_4 in PVA-H_2SO_4 GPE (Figure 3.6f). Further, the robustness of the rGO material in different GPE concentrations was examined through durability test (Figure 3.6f) where all solid-state supercapacitors in various GPE were subjected to 10,000 continuous CD cycles at a high current density of 15 A/g. Interestingly, all solid-state supercapacitors showed similar retention of capacitance value (>70%), therefore ruling out any possibility of significant degradation of the rGO at higher concentrations of GPE. Thus, our demonstrations clearly recommend a precise selection of concentration of PVA-H_2SO_4 GPE for various rGO as well as carbon-based materials for achieving high-capacitance values. To establish the aforementioned recommendation, we have further increased the GPE concentration upto 50 wt% and analyzed the electrochemical performance (Figures 3.6d-f). Surprisingly, even at very high H_2SO_4 in PVA-H_2SO_4 wt% such as 40 and 50 wt%, capacitance values were found to be similar to 20 wt% (Figure 3.6d). Notably, the consistent increment of wt% of H_2SO_4 in PVA and H_2O solution the resulted un-solidified PVA-H_2SO_4 mixture at room temperature, possibly due to higher dilution. Here, from 5-30 wt%, we do see a reasonable solidification (Figure 3.7a).

The origin of such an interesting trend of rGO supercapacitors in various GPE, Nyquist measurements on dried PVA-H_2SO_4 GPE were performed and investigated their ionic conductivity and finally, correlate with the trend in supercapacitor performance, if any. Nyquist plots (Figure 3.7b) were fitted and calculated R_{CT} was plotted against wt% of respective PVA-H_2SO_4 GPE (not given here). Interestingly, R_{CT} value reduced upto 20 wt% and increased beyond (upto 30 wt%) (Figure 3.7c), clearly corroborating the respective C_S values (Figure 3.7d). Such a trend of R_{CT} could be due to the resistance created by the direct ions collisions when concentration is increased beyond 20 wt%.[33]

The flexible all solid-state supercapacitor of rGO was fabricated on gold (Au) sputtered polyethylene terephthalate (PET) sheet thin film and subsequently dried under IR lamp. Two symmetric electrodes were assembled using 20 wt% H_2SO_4 in PVA-H_2SO_4 GPE and Celgard separator. While recording CV, the scan rate was swept from 5 to 500 mV/s possessing partial rectangular curve in the support of EDLC formation which was retained even at high scan rate of 0.5 V/s indicating high stability of rGO (Figure 3.8a).

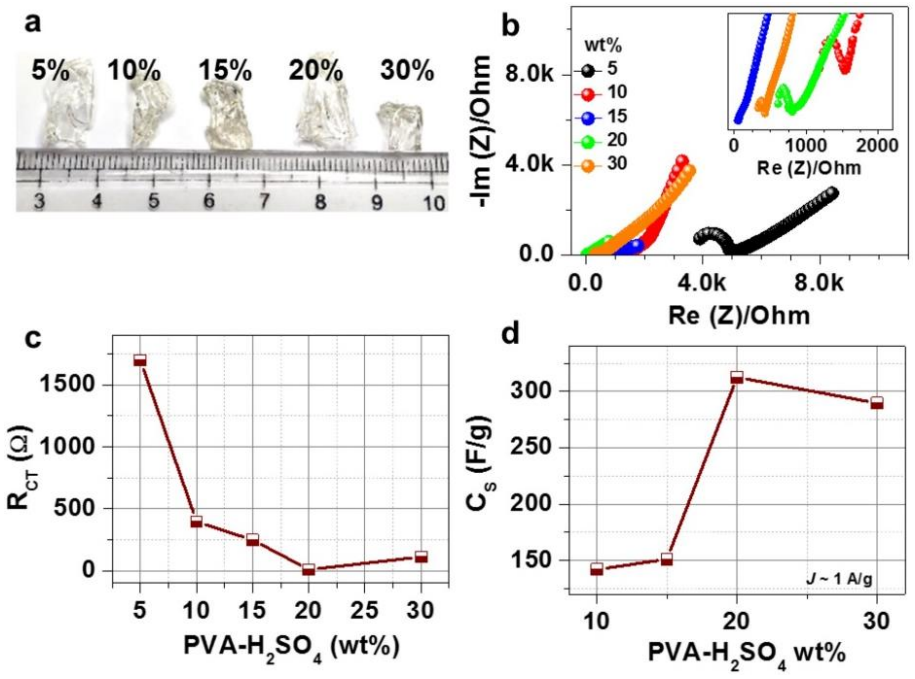

Figure 3.7. *(a) Dried PVA-H_2SO_4 GPE (5-30 wt%). (b) Nyquist plots of various (5-30 wt%) GPE. (c) R_{CT} of various GPE and (d) C_S of rGO in different PVA-H_2SO_4 GPE.*

The CD plots were recorded at different current densities from 0.2 A/g to 10 A/g to reveal the triangular curve with negligible IR drop at lower current density indicating the facile electrolytic ions percolation in the rGO (Figure 3.8b). We have also performed the Nyquist measurements of the rGO supercapacitor to extract the value of R_S to be ~2.4 Ω with negligible R_{CT}, altogether supporting the CV and CD characteristics (Figure 3.8c). The C_S values of rGO flexible supercapacitor was found to be ~120 F/g and ~40 F/g at current densities of 0.2 A/g and 10 A/g, respectively (Figure 3.8d). Energy and power densities of rGO all solid-state flexible device unveiled the values as high as ~4.1 Wh/kg (at 0.2 A/g) and ~1.8 kW/kg (at 10 A/g) (Figure 3.8e), respectively. In order to observe the mechanical stress sustainability of rGO, capacitance was calculated at different bending modes (Figures 3.8f, g). In order to probe the tolerability of the rGO, the assembled supercapacitor was subjected to repeated bending cycles (0°↔ 180°) and capacitance was measured at 0° after each cycle. After 10 bending cycles the capacitance of rGO degraded by 20% from initial value, which could be due to the initial strain/stress, somewhat, agitating the internal texture of the rGO supercapacitor. However, after 10 bending cycles the capacitance value was stabilized and intact up to 1000 bending cycles which is remarkable (Figures 3.8f, g).

The above results of rGO was strengthen via durability test at 180° and 0° (straight/normal mode (Figure 3.8h). First, the assembled supercapacitor was bent to 180° and subjected to 10000 continuous CD cycles at a high current density of 10 A/g, in the bent mode. Surprisingly, after 10000 continuous CD cycles, the rGO supercapacitor showed 100% capacitance retention. We then brought the capacitor to normal (0°) mode and tested the same for next 10000 CD cycles at same current density in normal mode. Again the capacitance retention was found to be 100%, instead very minute deviation in capacitance was witnessed. Further bending of rGO supercapacitor did not alter the capacitance and retention was found to be 100% even after, further, 10000 continuous CD cycles at 10 A/g current density in the bent mode (Figure 3.8h).

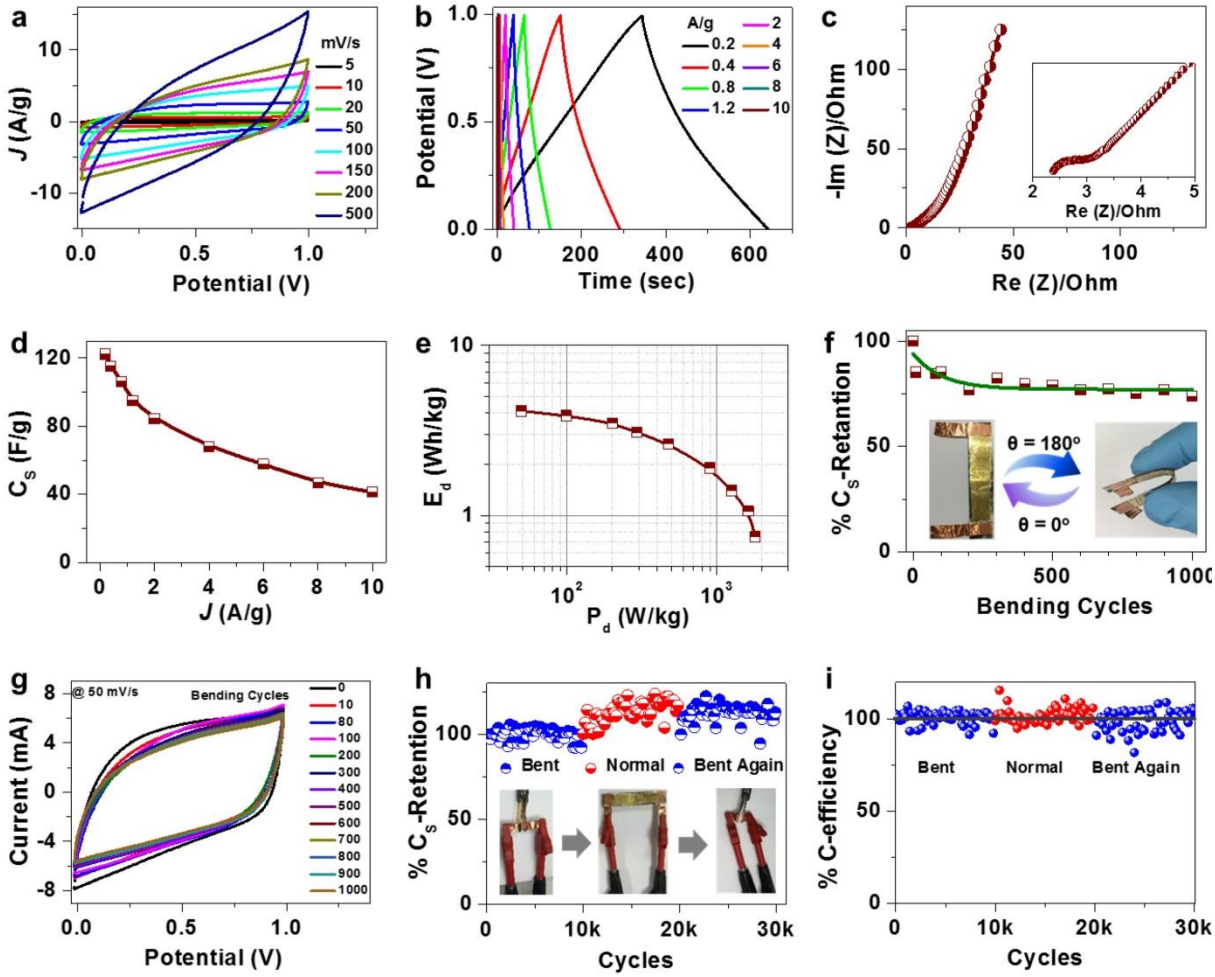

Figure 3.8. *(a-c) CV, CD, and Nyquist plots (inset: zoomed in Nyquist plot), (d) C_S versus current density, (e) Ragone plot, (f-g) Repeated bending cycles (inset: photographs) at a scan rate of 50 mV/s (CV), (h-i) Durability cycles (inset: photographs) and Coulombic efficiency at a current density of 10 A/g, of rGO all solid-state flexible supercapacitor.*

Overall, 100% C_S retention and Coulombic efficiency (Figures 3.8h, i), was realized after a total of 30000 durability cycles which is not frequently observed. Thus, flexibility and durability performance of rGO all solid-state flexible supercapacitor is outstanding.

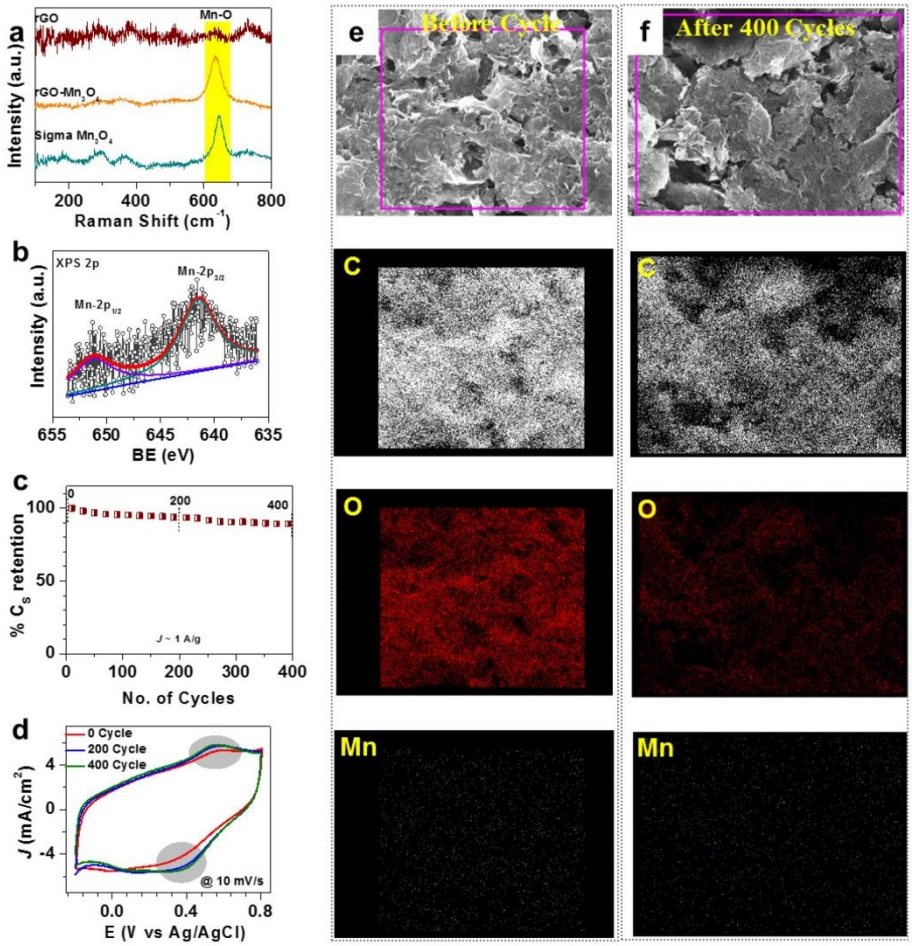

Figure 3.9. *(a) Raman spectra of rGO, rGO-Mn_3O_4, and Mn_3O_4 (from Sigma). (b) Mn 2p XPS of rGO. (c) Durability of rGO at a current density of 1 A/g. (d) CV of rGO at 0^{th}, 200^{th}, and 400^{th} cycles. (e-f) EDXS mapping of rGO electrode before and after durability cycles.*

Now the question is why the capacitance of our rGO is high? Recently, it has been discussed that high capacitance value of the carbon based materials depends on many parameters – accessible surface area to the ions of the electrolyte, presence of heteroatoms, defects, surface groups, texture of the materials, and presence of redox ion species.[34] Our rGO exhibits BET surface area of around 60 m^2/g which is high for a micrometer sized layered material with mesoporous characteristics (d > 2 nm) (Figure 3.3c).[35] Also, it is important to note that the BET surface area calculation only deals with pores of the materials whereas in capacitor, ions of electrolyte access all active surface of the materials.[34]

The crumbled morphology of thin rGO could make it more exposed to the electrolyte. Furthermore, the rGO material was examined thorough Raman, PXRD, and XPS where we found ~5% Mn additive may be present as Mn_xO_y (Figures 3.2d, 3.9a, b). The CV of rGO coated electrode (working) was recorded in 3-electrode setup using Ag/AgCl and Pt-wire as reference and counter electrodes, respectively, dipped in 0.5 M H_2SO_4 electrolyte. The redox features of CV (Figure 3.9d) clearly revealed the presence of pseudocapacitance, possibly originating from the Mn_xO_y additives and synergistically contributing to the high capacitance value along with the EDLC.[34] To strengthen the aforementioned plausible mechanism, the stability test of rGO coated electrode in two electrode set-up, at 1 A/g current density was performed and also examined the robustness of Mn_xO_y additives (Figure 3.9c). CV in 3-electrode set-up was recorded at 0^{th}, 200^{th}, and 400^{th} CD cycles and remarkably, redox features were consistently retained (Figure 3.9d). The EDXS mapping of rGO electrode before and after CD cycles unveiled the presence of Mn corroborating CV results (Figures 3.9e, f).

3.3. Conclusions

In conclusion, $MnCl_2/NH_4OH$ system is successfully used for an effective reduction of GO producing high-quality and ambient stable rGO. Introduction of 20 wt% PVA-H_2SO_4 GPE drastically elevated the overall performance of the rGO – well-beyond the adequate supercapacitor performance in aqueous 0.5 M H_2SO_4 and solid-state (10 wt% PVA-H_2SO_4) configurations. The fabricated solid-state flexible rGO supercapacitors exhibited remarkable sustainability towards bending as well as durability cycles. Improvisation of GPE is sought after by employing the supportive additives in rGO supercapacitors to compete with the commercially available carbon-supercapacitors. Also, our results recommend the use of ecofriendly aqueous electrolytes in boosting the performance of carbonaceous supercapacitors.

3.5. References

(1) González, A.; Goikolea, E.; Barrena, J. A.; Mysyk, R. Review on Supercapacitors: Technologies and Materials. *Renew. Sustain. Energy. Rev.* **2016**, *58*, 1189-1206.

(2) Conway, B. E. Transition from "Supercapacitor" to "Battery" Behavior in Electrochemical Energy Storage. *J. Electrochem. Soc.* **1991**, *138*, 1539.

(3) Jha, P. K.; Singh, S. K.; Kumar, V.; Rana, S.; Kurungot, S.; Ballav, N. High-Level Supercapacitive Performance of Chemically Reduced Graphene Oxide. *Chem* **2017**, *3*, 846-860.

(4) Hwang, J. Y.; El-Kady, M. F.; Li, M.; Lin, C.-W.; Kowal, M.; Han, X.; Kaner, R. B. Boosting the Capacitance and Voltage of Aqueous Supercapacitors Via Redox Charge Contribution from Both Electrode and Electrolyte. *Nano Today* **2017**, *15*, 15-25.

(5) Mourad, E.; Coustan, L.; Lannelongue, P.; Zigah, D.; Mehdi, A.; Vioux, A.; Freunberger, S. A.; Favier, F.; Fontaine, O. Biredox Ionic Liquids with Solid-Like Redox Density in the Liquid State for High-Energy Supercapacitors. *Nat. Mater.* **2016**, *16*, 446-453.

(6) Zhong, C.; Deng, Y.; Hu, W.; Qiao, J.; Zhang, L.; Zhang, J. A Review of Electrolyte Materials and Compositions for Electrochemical Supercapacitors. *Chem. Soc. Rev.* **2015**, *44*, 7484-7539.

(7) Cheng, X.; Pan, J.; Zhao, Y.; Liao, M.; Peng, H. Gel Polymer Electrolytes for Electrochemical Energy Storage. *Adv. Energy Mater.* **2018**, *8*, 1702184.

(8) Ferrari, A. C.; Robertson, J. Interpretation of Raman Spectra of Disordered and Amorphous Carbon. *Phys. Rev. B* **2000**, *61*, 14095-14107.

(9) Chua, C. K.; Pumera, M. The Reduction of Graphene Oxide with Hydrazine: Elucidating Its Reductive Capability Based on a Reaction-Model Approach. *Chem. Commun.* **2016**, *52*, 72-75.

(10) Abdelkader, A. M.; Vallés, C.; Cooper, A. J.; Kinloch, I. A.; Dryfe, R. A. W. Alkali Reduction of Graphene Oxide in Molten Halide Salts: Production of Corrugated Graphene Derivatives for High-Performance Supercapacitors. *ACS Nano* **2014**, *8*, 11225-11233.

(11) Moon, I. K.; Lee, J.; Ruoff, R. S.; Lee, H. Reduced Graphene Oxide by Chemical Graphitization. *Nat. Commun.* **2010**, *1*, 73.

(12) Fan, Z.-J.; Kai, W.; Yan, J.; Wei, T.; Zhi, L.-J.; Feng, J.; Ren, Y.-m.; Song, L.-P.; Wei, F. Facile Synthesis of Graphene Nanosheets Via Fe Reduction of Exfoliated Graphite Oxide. *ACS Nano* **2011**, *5*, 191-198.

(13) Groen, J. C.; Peffer, L. A. A.; Pérez-Ramírez, J. Pore Size Determination in Modified Micro- and Mesoporous Materials. Pitfalls and Limitations in Gas Adsorption Data Analysis. *Micropor. Mesopor. Mat.* **2003**, *60*, 1-17.

(14) Chua, C. K.; Pumera, M. Chemical Reduction of Graphene Oxide: A Synthetic Chemistry Viewpoint. *Chem. Soc. Rev.* **2014**, *43*, 291-312.

(15) Casero, E.; Parra-Alfambra, A. M.; Petit-Domínguez, M. D.; Pariente, F.; Lorenzo, E.; Alonso, C. Differentiation between Graphene Oxide and Reduced Graphene by Electrochemical Impedance Spectroscopy (EIS). *Electrochem. Commun.* **2012**, *20*, 63-66.

(16) Wu, Z.-S.; Sun, Y.; Tan, Y.-Z.; Yang, S.; Feng, X.; Müllen, K. Three-Dimensional Graphene-Based Macro- and Mesoporous Frameworks for High-Performance Electrochemical Capacitive Energy Storage. *J. Am. Chem. Soc.* **2012**, *134*, 19532-19535.

(17) Li, Z.-F.; Zhang, H.; Liu, Q.; Sun, L.; Stanciu, L.; Xie, J. Fabrication of High-Surface-Area Graphene/Polyaniline Nanocomposites and Their Application in Supercapacitors. *ACS Appl. Mater. Interfaces* **2013**, *5*, 2685-2691.

(18) Chen, Y.; Zhang, X.; Zhang, D.; Yu, P.; Ma, Y. High Performance Supercapacitors Based on Reduced Graphene Oxide in Aqueous and Ionic Liquid Electrolytes. *Carbon* **2011**, *49*, 573-580.

(19) Kim, J.-Y.; Kim, K.-H.; Yoon, S.-B.; Kim, H.-K.; Park, S.-H.; Kim, K.-B. In Situ Chemical Synthesis of Ruthenium Oxide/Reduced Graphene Oxide Nanocomposites for Electrochemical Capacitor Applications. *Nanoscale* **2013**, *5*, 6804-6811.

(20) Mhamane, D.; Unni, S. M.; Suryawanshi, A.; Game, O.; Rode, C.; Hannoyer, B.; Kurungot, S.; Ogale, S. Trigol Based Reduction of Graphite Oxide to Graphene with Enhanced Charge Storage Activity. *J. Mater. Chem.* **2012**, *22*, 11140-11145.

(21) Lin, Z.; Liu, Y.; Yao, Y.; Hildreth, O. J.; Li, Z.; Moon, K.; Wong, C.-p. Superior Capacitance of Functionalized Graphene. *J. Phys. Chem. C* **2011**, *115*, 7120-7125.

(22) Wu, Q.; Sun, Y.; Bai, H.; Shi, G. High-Performance Supercapacitor Electrodes Based on Graphene Hydrogels Modified with 2-Aminoanthraquinone Moieties. *Phys. Chem. Chem. Phys.* **2011**, *13*, 11193-11198.

(23) Yadav, P.; Banerjee, A.; Unni, S.; Jog, J.; Kurungot, S.; Ogale, S. A 3D Hexaporous Carbon Assembled from Single-Layer Graphene as High Performance Supercapacitor. *ChemSusChem* **2012**, *5*, 2159-2164.

(24) Xu, Y.; Lin, Z.; Huang, X.; Liu, Y.; Huang, Y.; Duan, X. Flexible Solid-State Supercapacitors Based on Three-Dimensional Graphene Hydrogel Films. *ACS Nano* **2013**, *7*, 4042-4049.

(25) Bard, A. J., Faulkner, Larry R. *Electrochemical Methods : Fundamentals and Applications* Wiley: New York, 1980.

(26) Kötz, R.; Carlen, M. Principles and Applications of Electrochemical Capacitors. *Electrochim. Acta* **2000**, *45*, 2483-2498.

(27) Miller, J. R.; Burke, A. F. Electrochemical Capacitors: Challenges and Opportunities for Real-World Applications. *Electrochem. Soc. Interface* **2008**, *17*, 53.

(28) Gao, W.; Alemany, L. B.; Ci, L.; Ajayan, P. M. New Insights into the Structure and Reduction of Graphite Oxide. *Nat. Chem.* **2009**, *1*, 403.

(29) Yao, X.; Zhao, Y. Three-Dimensional Porous Graphene Networks and Hybrids for Lithium-Ion Batteries and Supercapacitors. *Chem* **2017**, *2*, 171-200.

(30) Chua, C. K.; Pumera, M. Reduction of Graphene Oxide with Substituted Borohydrides. *J. Mater. Chem. A* **2013**, *1*, 1892-1898.

(31) Wang, Y.; Chen, J.; Cao, J.; Liu, Y.; Zhou, Y.; Ouyang, J.-H.; Jia, D. Graphene/Carbon Black Hybrid Film for Flexible and High Rate Performance Supercapacitor. *J. Power Sources* **2014**, *271*, 269-277.

(32) Chen, S.; Ma, W.; Xiang, H.; Cheng, Y.; Yang, S.; Weng, W.; Zhu, M. Conductive, Tough, Hydrophilic Poly(Vinyl Alcohol)/Graphene Hybrid Fibers for Wearable Supercapacitors. *J. Power Sources* **2016**, *319*, 271-280.

(33) Bard, A. J.; Faulkner, L. R. *Electrochemical Methods: Fundamentals and Applications, 2nd Edition*. John Wiley & Sons: 2000.

(34) Lin, Z.; Goikolea, E.; Balducci, A.; Naoi, K.; Taberna, P. L.; Salanne, M.; Yushin, G.; Simon, P. Materials for Supercapacitors: When Li-Ion Battery Power Is Not Enough. *Mater. Today* **2018**, *21*, 419-436.

(35) Yan, J.; Yang, L.; Cui, M.; Wang, X.; Chee, K. J.; Nguyen, V. C.; Kumar, V.; Sumboja, A.; Wang, M.; Lee, P. S. Aniline Tetramer-Graphene Oxide Composites for High Performance Supercapacitors. *Adv. Energy Mater.* **2014**, *4*, 1400781-1400788.

Chapter 4

Reduction of Graphene Oxide by CuCl for Supercapacitor Applications

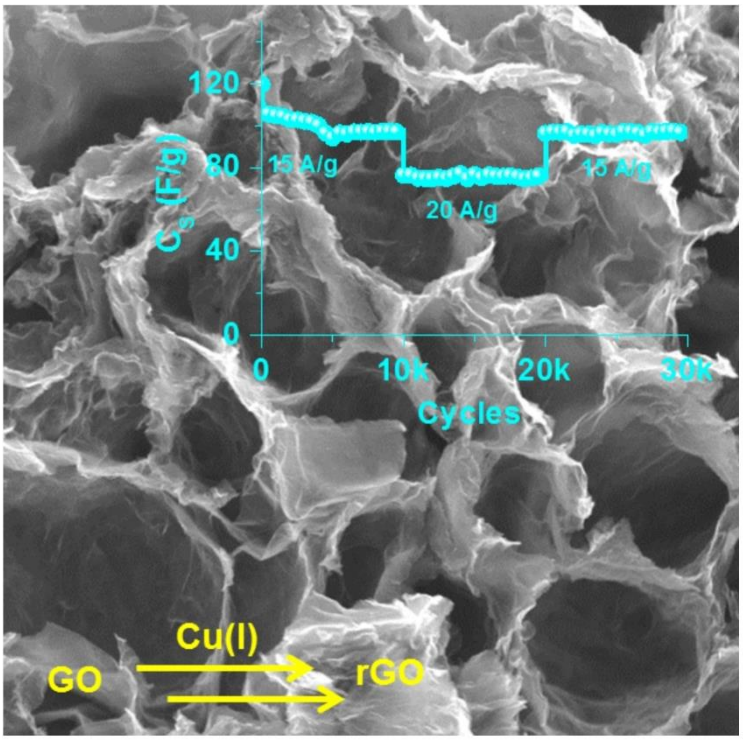

4.1. Introduction

In previous chapters (2 and 3), redox systems – Fe(III)/Fe(II) and Mn(III)/Mn(II) were explored for the production of rGO with remarkable electrochemical performance.

In this chapter, other period IV transition metal salts were screened. On the basis of their standard reduction potential (E°) – Co(III)/Co(II) (1.92 V), Ni(III)/Ni(II) (1.7 V), and Cu(II)/Cu(I) (0.159 V), all of them can, in fact, reduce graphene oxide (GO).[1] However, the higher oxidation state of Co(II) and Ni(II) is relatively less favourable compared to Cu(I).[2] Therefore, we have selected copper(I) chloride (CuCl) salt and employed for the reduction of GO for the first time. The extracted rGOs were used as an active material and fabricated all solid-state supercapacitors in 10 and 20 wt% PVA-H_2SO_4 gel polymer electrolyte (GPE) showed remarkable performance. The detail investigation of rGO unveiled the interesting physicochemical properties responsible for its remarkable electrochemical performance.

4.2. Materials and Method

GO synthesis is already explained in chapter 2. Before reduction, GO was centrifuged at 1000 rpm for 5 min to remove the multilayers.

About 0.9 g CuCl was dispersed in 150 mL MQ water and mixed with 150 ml GO (~1 mg/mL) in 1 L round bottom flask and stirred at 94 °C for 24 hr. Light green precipitate thus formed is filtered and washed with water/methanol and dried under vacuum at 150 °C for ~10 hr. About 250 mg grey-light green powder was then mixed in 50 mL 0.5 M HCl and stirred for ~48 hr at room temperature (RT), followed by washing with water/acetone and vacuum drying at 70 °C for ~12 hr.

For HF treatment, ~250 mg grey-light green powder was soaked in 4 M HF solution (50 mL) and continuously stirred for 24 hr at RT. The black precipitate was washed with water and acetone/methanol and vacuum dried for 12 hr at 70 °C.

10 and 20 wt% H_2SO_4 in PVA-H_2SO_4 Gel Preparation is as described in chapter 2 and 3. Fabrication of all solid-state supercapacitors is as described in chapter 2. Active mass loading of materials were 1 mg/cm^2.

4.3. Results and Discussion

After the reduction with Cu(I), a light green colored powder was obtained which was vacuum heated for ~10 hr at 150 °C and finally grey-light green powder was treated with 0.5 M HCl to remove the other unwanted copper complex (detail is explained below and in experimental section as well) and rGO was isolated (Figure 4.1).

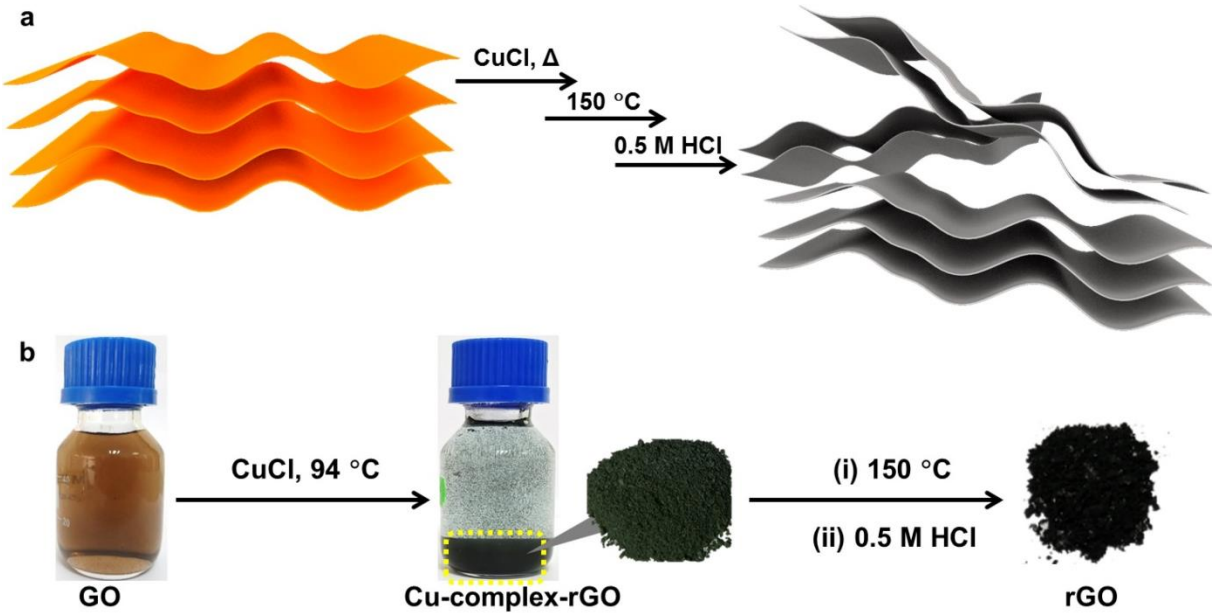

Figure 4.1. *(a-b) Schematic illustration and optical photographs of GO to rGO production.*

The X-ray photoelectron spectroscopy (XPS) of GO and rGO are shown in Figures 4.2a, b. C1s XPS spectrum of GO showed (Figure 4.2a) peaks at ~284.8, ~287.0, and ~288.4 eV corresponding to the presence of C-C, -C-OH/-C-O and -COO^- functional groups, respectively. For rGO, the peak intensity at ~287.0 of –C-OH/-C-O shifted towards lower binding energy ~286.3 eV and decreased significantly which actually depicts the removal of –C-OH/-C-O functional group during reduction process. Also, peak maxima for rGO at ~288.2 eV decreased compared to GO suggesting that the reduction process could also reduce -COO^- functional group. Finally, peak at around 284.8 eV of -C-C- functional group increased, altogether suggesting recouping of van der Wall interaction and π-electron clouds on graphene networks (Figure 4.2b).[3-6] Further, FTIR spectra were collected on the pressed KBr pellets and the presence of peaks at ~1062, ~1225, ~1564, ~1723, and ~3401/1361 cm^{-1} referring to -C-O, -C-O-C-, -C=C-, -C=O, and -C-OH functional groups in GO revealed the successful oxidation of Gr to GO (Figure 4.2c).

Interestingly, in the case of rGO, peaks corresponding to -C-O, -C-O-C-, and -C=O reduced heavily. Noticeably, the peak at ~3401/1361 cm^{-1} of -C-OH functional group for rGO, disappeared complimenting the XPS data, whereas, peak intensity at ~1564 cm-1 of -C=C- functional group intensified compared to GO suggesting the increased number of π-conjugation in rGO material (Figure 4.2c).[5-6]

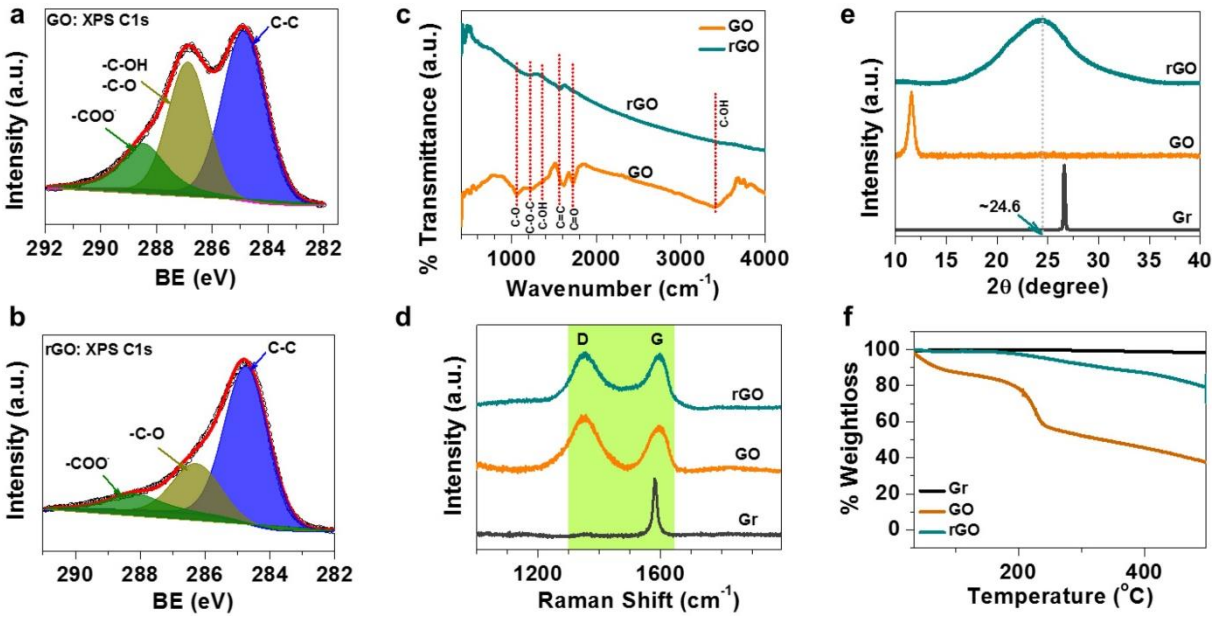

Figure 4.2. *(a) C1 XPS data of GO. (b) C1 XPS data of rGO. (c) FTIR spectra of GO and rGO. (d) Raman spectra of Gr, GO, and rGO. (e) PXRD patterns of Gr, GO, and rGO and (f) TGA plots of GR, GO, and rGO.*

In order to support the XPS and FTIR data, we have performed Raman measurements on Gr, GO, and rGO and in all the samples, characteristic D (defect band) and G band (graphene peak) appeared at ~1352 cm^{-1} and 1583-1596 cm^{-1} (Figure 4.2d). For Gr, a small hump of D band and a sharp peak of G band indicates the presence of majorly sp^2 hybridized carbon networks (Figure 4.2d). GO possess sp^2 as well as sp^3 hybridised carbon networks as evidenced from the Raman spectrum where both D and G bands are present. For rGO, the characteristic G band increased compared to GO suggesting that the reduction of functional groups and recouping of π-conjugations due to increased sp^2 carbon networks (Figure 4.2d).[7] In PXRD, the graphitic (002) plane at 26.6° (d ~0.34 nm) shifted towards a lower 2θ value of 11.2° (~0.77 nm) after the oxidation, where oxygen functionality on the basal and the peripheral carbons repelled each other apart. Furthermore, the reduction of GO can be noticed with (002) peak shifting towards higher 2θ (~24.6°) value, however, the broadening of the peak of rGO indicates the non-

crystalline nature of rGO (Figure 4.2e).[4,8] The thermal gravimetric analysis (TGA) showed the thermal stability of rGO upto 200 K without any weight loss (already discussed in chapter 2) (Figure 4.2f).[4]

The morphology of rGO was analysed through FESEM and TEM which showed thin graphene sheets assembled like Lotus seed pods with very large channel size (Figures 4.3a, b). Such morphology is usually observed in the case of freeze dried rGO gel leading to its high capacitance.[3,9-10] In our approach, the careful removal of Cu-complex from the rGO benefited to generate the large sized pores all over the material. Reduction of GO to rGO resulted in simultaneous oxidation of Cu(I) to Cu(II) which then formed a complex with OH^- and Cl^- ions having octahedron like morphology which is probably strongly bound to the rGO networks. The controlled reduction followed by elimination of Cu-complex from the rGO matrix lead to the formation of larger pores and avoided the massive stacking of sheets which generally happens due to strong π-π interactions between the rGO sheets. The EDXS and XPS data showed almost negligible amount of Cu (Figures 4.3c, d).

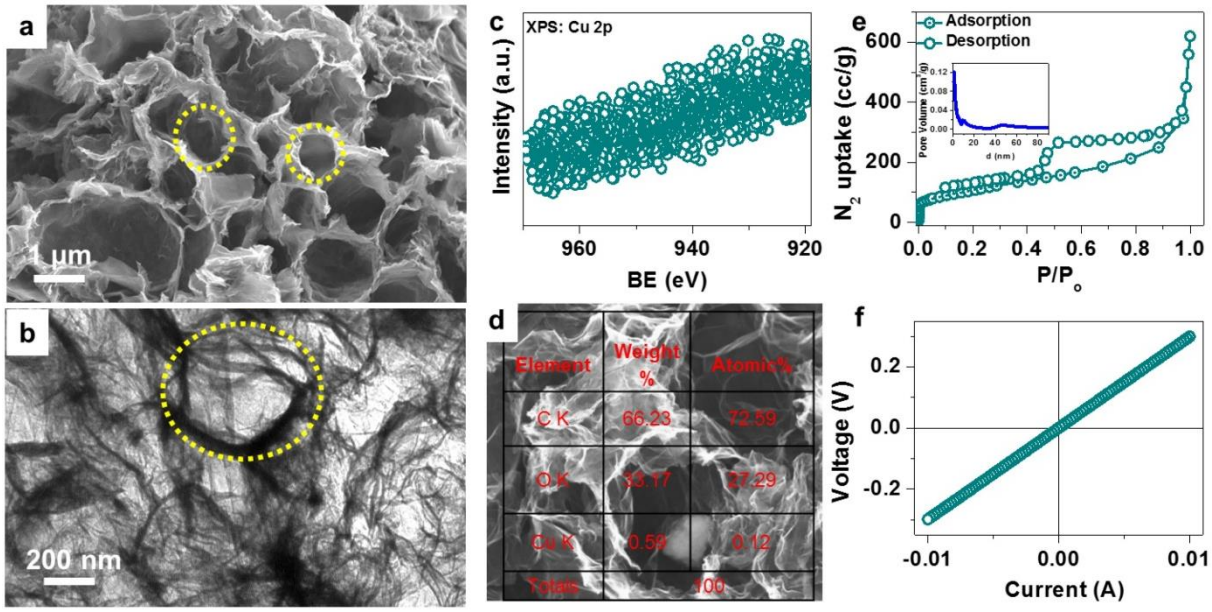

Figure 4.3. *(a-b) FESEM and TEM images of rGO. (c) Cu 2p XPS data of rGO. (d) EDXS of rGO. (e) N_2 adsorption-desorption isotherms of rGO at 77 K and (f) DC current-voltage (I-V) characteristics of rGO.*

To extract the surface area of rGO, N_2 adsorption-desorption isotherms were recorded at 77 K where BET surface area of rGO was estimated to be around 362 m^2/g (Figure 4.3e). The hysteresis in the graph indicates mesoporous behaviour usually observed for porous graphene-based materials.[11] The average pore diameter of the rGO produced, was found to be ~8.7 nm (Figure 4.3e, inset). Such a high surface area and pore diameter of our rGO could be very useful for high energy storage applications. The DC electrical conductivity measurements done on the pressed films of rGO by four probe revealed the value to be ~1.5 S/cm which is comparable to the rGOs reported in the literature, synthesised chemically by conventional reducing agents (Figure 4.3f).[12] Overall, our method of GO reduction do have potential to generate highly porous and conducting rGO which is otherwise rarely observed in the domain of chemically synthesised rGO.

Such high porosity along with electrical conductivity influenced us to examine the rGO for supercapacitor application. An all solid state supercapacitors of rGO in 10 wt% of PVA-H_2SO_4 gel polymer electrolyte (GPE) were fabricated (Figure 4.5a) and subjected to electrochemical measurements through cyclic voltammetry (CV), galvanic charge-discharge (CD), and electrochemical impedance spectroscopy (EIS) techniques and extracted the information regarding EDLC characteristics, specific capacitance (C_S), equivalent series resistance (R_S), energy density (E_d), power density (P_d), and cycle stability (Figures 4.4, 4.5 and 4.6). Briefly, to configure all solid-state supercapacitors, rGO ink was drop-casted on grafoil sheet and two similar electrodes were sandwiched together using Celgard 3501 separator and 10 wt% PVA-H_2SO_4 GPE (Figure 4.5a).

The CV of rGO supercapacitor recorded from 10-500 mV/s scan rate and partial rectangular curves depicting electrical double layer (EDL) formation between electrode and electrolyte which is generally observed for pure graphene based materials (Figure 4.4a).[13] The curve feature was almost maintained even at high scan rate of 500 mV/s, indicating the facile ions' percolation through the channels of the material. The CD measurements from 1-10 A/g corroborated with the CV plots where triangular curves at lower current density with negligible IR drop (V = IR, I = current, R = resistance) revealed the fast percolation of electrolyte into the channels (Figure 4.4c). At higher current density of 10 A/g we have observed a very small IR drop (~0.1V) which proposes the high power capacity of the material due to the lower resistance of the ions during the percolation process (Figures 4.4c). This low resistance is also visible in the EIS analysis (frequency range from 120 kHz -10 mHz) where the curve edge at

high frequency showed equivalent series resistance (R_S) of the device to be as low as ~1.22 Ω (Figure 4.5d, inset). This low internal resistance is possibly due to the facile mobility of electrolytic ions inside the pores of the rGO.[4,13-14] Nyquist plot at the low frequency region is nearly perpendicular to the x-axis indicating the EDL characteristics, complementing CV and CD data (Figure 4.5d).[4,14] The capacitance of rGO was calculated from CD and plotted against current density (*J*) (Figure 4.5e). The maximum specific capacitance (C_S) value of rGO was found to be around ~240 F/g at a current density of 1 A/g, also at very high current density of 10 A/g the capacitance was found to be ~90 F/g (Figure 4.5e). Such remarkable capacitance has been observed earlier, either in freeze dried rGO gel or other rGOs synthesized using conventional reducing agents after etching to generate porous morphology, altogether, our value stands either comparable or higher (Table 4.1).

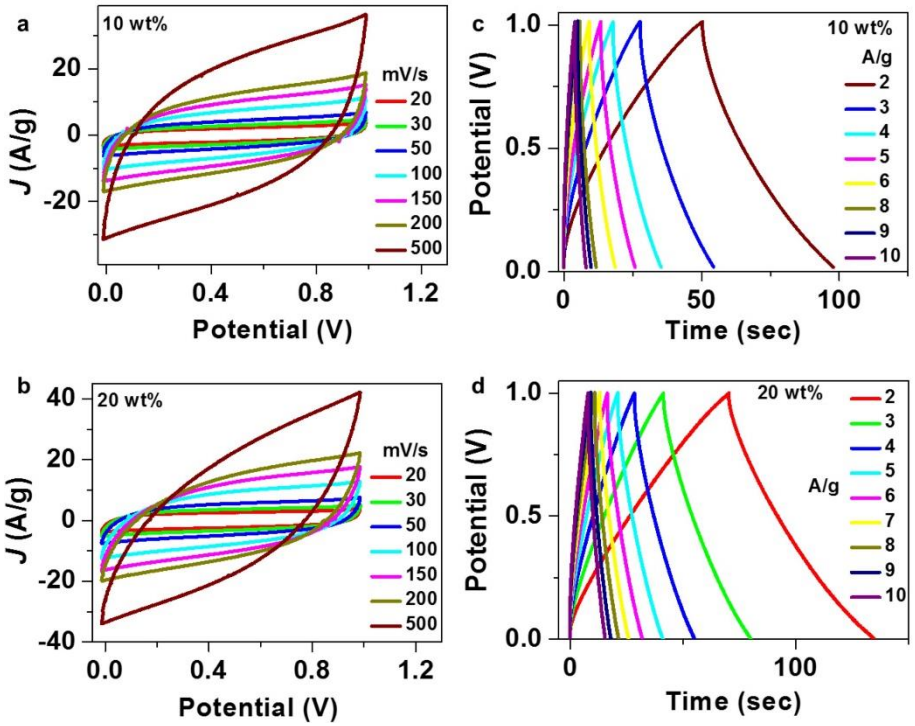

Figure 4.4. *(a-b) CV and (c-d) CD of rGO all solid-state supercapacitor in 10 and 20 wt% H_2SO_4 in PVA-H_2SO_4 GPE.*

From Bode phase plot (not given here), the time constant of rGO was calculated to be ~1 sec (T=1/f_o, f_o=1 Hz at ~45° phase angle) which is, in fact, very low for rGO based materials (not given here). The time independent capacitance of rGO was obtained after exploring the following formula, $C = k_1 + k_2 v^{-1/2}$ (where, C = capacitance, k_1 = rate-independent component attributing for EDLC, $k_2 v^{-1/2}$ represents long-T capacitance data) and the value

observed is ~112 F/g after extrapolating the curve to $discharge\ time^{1/2}$ = 0, which is noteworthy (Figure 4.5f).[15-16]

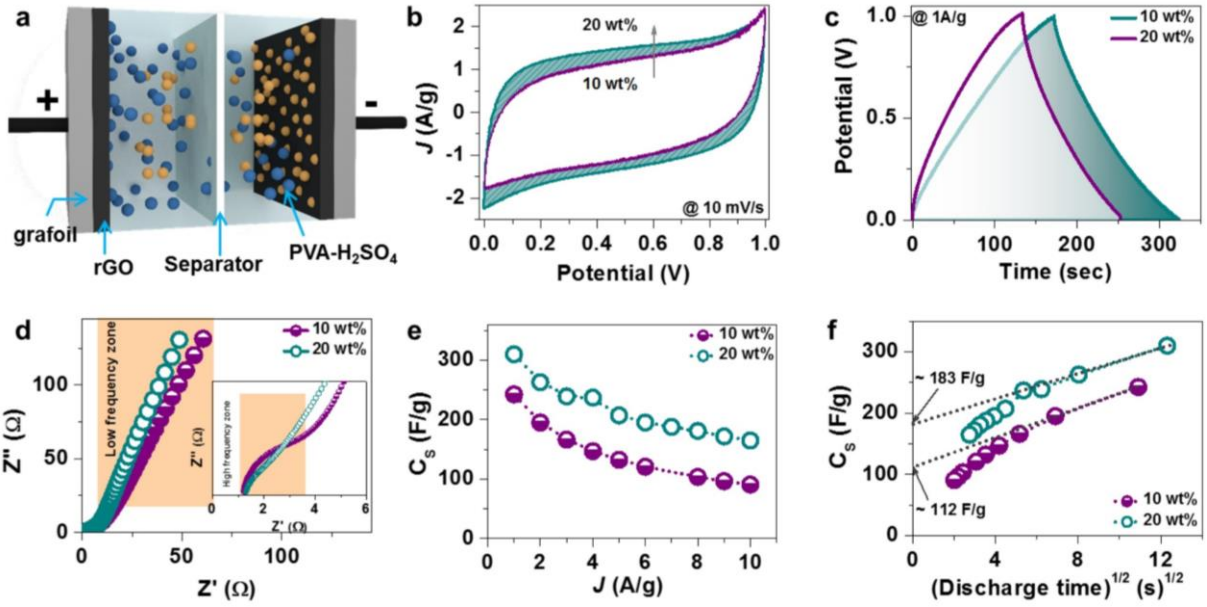

Figure 4.5. *(a) Schematic presentation of all solid-state supercapacitor. (b-d) CV, CD, and Nyquist plots, (e) C_S versus current density (J) plots and (f) C_S versus $(discharge)^{1/2}$ plots, of rGO all solid-state supercapacitors in 10 and 20 wt% H_2SO_4 in PVA-H_2SO_4 GPE.*

In energy storage devices, ultimately E_d and P_d values decide the final performance for commercial applications.[17] It is noticeable that the E_d of symmetric supercapacitor can be enhanced either by increasing the capacitance value or by expanding the voltage window by employing non-aqueous electrolyte.[13] Recent reports on rGO based supercapacitor strongly suggests to avoid the use of organic electrolytes in the view of eco-friendly operation.[18] Thus, only option to boost the E_d value in aqueous electrolyte is to increase the capacitance itself in the symmetric two electrodes rGO all solid-state supercapacitor setup. Therefore, a non-conventional reducing agent (CuCl) to reduce the GO to rGO with optimally balanced physicochemical properties and appealing morphology was realised to be better choice in terms of synthesizing template mediated rGO materials.

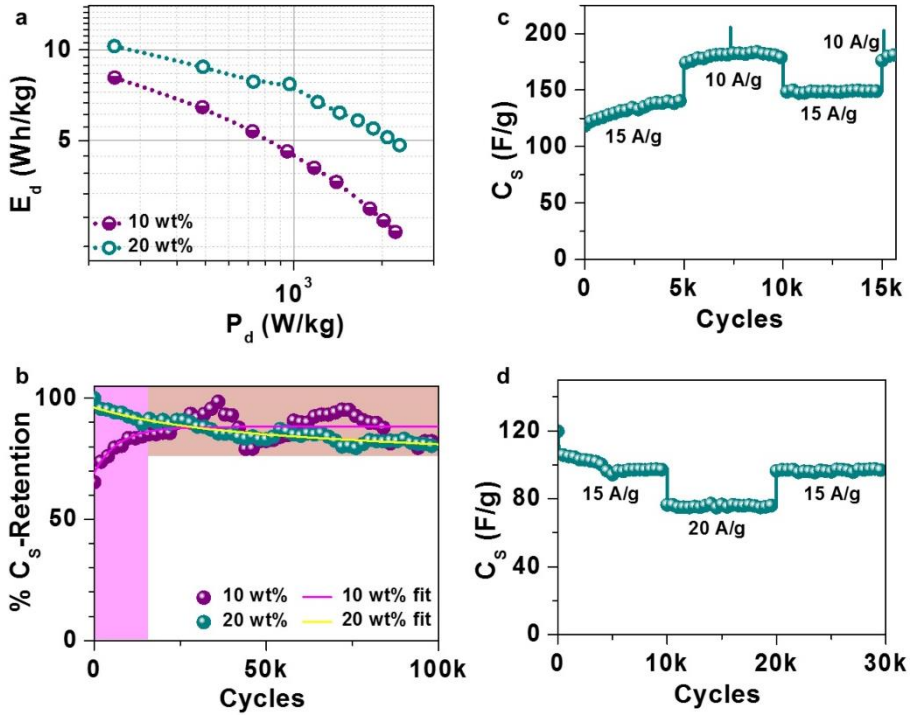

Figure 4.6. *(a) E_d and P_d, (b) Durability cycles at a current density of 20 A/g, (c-d) Durability cycles at different current densities (switching of J consecutively after 5000 (c) and 10000 (d) cycles), of rGO all solid-state supercapacitors in 20 wt% H_2SO_4 in PVA-H_2SO_4 GPE.*

The specific energy and power densities (E_d and P_d) of rGO were calculated from the CD values and remarkable values of ~8 Wh/kg and ~245 W/kg respectively were found at a current density of 1 A/g (Figure 4.6a). Further increment in the current density of rGO to 10 A/g, boosted the P_d value beyond 2.2 kW/kg maintaining the E_d value at ~2.5 Wh/kg (Figure 4.6a). The calculated E_d and P_d values of our synthesised rGO were comparable or higher than other reported chemically synthesised rGOs (Table 4.1). Due to daily energy consumption, supercapacitors have to charge and discharge multiple times, hence long term sustainability of active materials is very crucial. In previous reports, we observed that the high capacitive materials such as metal oxides and conducting polymers are unable to seek significant attention due to their poor durability (Table 4.1). On the other hand, graphene based materials exhibit long life cycle, however, they are mostly unable to fulfil the criteria of high capacitance and long term durability (Table 4.1). As our synthesised rGO showed very high capacitance value, second criteria of long durability must follow-up for the industrial application. In order to test the durability, 100 k continued CD cycles were performed at a high current density of 20 A/g. Remarkably, after 100 k cycles the capacitance retention of rGO was found to be more than 80% which, in fact, strongly validates the high stability of the rGO materials (Figure 4.6b).

Overall, controlled synthesis and careful removal of template, produced rGO with desirable channel size and higher accessible surface for electrolytic ions, as well as the high electrical conductivity which altogether enhanced the electrochemical performance.

In chapter 3, we have introduced the concept of systematic variation of H_2SO_4 (from 10 to 50 wt%) in PVA-H_2SO_4 GPE for the enhancement of capacitance values. Here, we have employed the similar approach and fabricated all solid-state supercapacitor of rGO in 20 wt% H_2SO_4 in PVA-H_2SO_4 GPE and compared the electrochemical performance with 10 wt% PVA-H_2SO_4 GPE. To determine the electrochemical performance, CV, CD, EIS, and cycling stability of rGO were recorded in 20 wt% H_2SO_4 in PVA-H_2SO_4 GPE. The CV and CD were collected at scan rates ranging from 10 to 500 mV/s and current densities from 1 to 10 A/g, respectively. The EDL formation between electrode and GPE was realised by partial rectangular CV and triangular CD plots (Figures 4.4c, d). In CV, the current density of rGO increased upon increasing the GPE concentration from 10 to 20 wt% which indicates the higher charge accumulation in the material simply by increasing the H^+ and SO_4^{2-} concentration in the electrolyte (Figure 4.5b). Further, the discharge time is also increased for 20 wt% H_2SO_4 in PVA-H_2SO_4 in CD complementing the CV curve (Figure 4.5c). From Nyquist plot, we have gathered information about R_S, charge transfer resistance (R_{CT}), and capacitive behaviour of rGO supercapacitor. The R_S of rGO was found to be ~1.29 Ω which suggests that the higher concentration of electrolytic ions are not affecting the equivalent series resistance (Figure 4.5d). However, imperceptible semicircle in high frequency region indicates the consequence of higher H^+ and SO_4^{2-} ions concentration in 20 wt% H_2SO_4 in PVA-H_2SO_4, that is, the concentration of ions per unit volume reducing the charge transfer resistance and accelerating the ions' percolation inside the channels of rGO (Figure 4.5d, inset). Moreover, at low frequency region, real Z values of rGO in 20 wt% H_2SO_4 in PVA-H_2SO_4 GPE are lower than that of 10 wt% PVA-H_2SO_4 indicating the superior capacitive behaviour of rGO in 20 wt% H_2SO_4 in PVA-H_2SO_4 (Figure 4.5d). The capacitance of rGO was calculated from CD curves and plotted against current density (*J*) (Figure 4.5e). Noticeably, the capacitance value of rGO in 20 wt% H_2SO_4 in PVA-H_2SO_4 was increased >1.3 times as compared to that in 10 wt% PVA-H_2SO_4. At low and high current densities of 1 and 10 A/g, the capacitance values were calculated to be ~310 F/g and ~165 F/g, respectively, which is highest amongst chemically synthesised rGO reported in literature (Table 4.1).

We have calculated the time independent capacitance value from aforementioned formula and estimated it to be ~185 F/g which is higher compared to that in 10 wt% PVA-H_2SO_4 GPE (Figure 4.5f). The E_d value of rGO in 20 wt% H_2SO_4 in PVA-H_2SO_4 is calculated to be ~10.5 Wh/kg which is increased by a factor of 1.3 as compared to the value calculated for 10 wt% PVA-H_2SO_4, however the P_d value was unaffected (Figure 4.6a). To examine the stability of rGO in comparatively higher concentrations of PVA-H_2SO_4, we have carried out 100 k continued CD cycles at a current density of 20 A/g. Remarkably, even after 100 k cycles more than 80% capacitance retention was observed which indicates that the increased concentration of GPE does not affect the material stability at all, in fact, it increased the energy storage capacity of the rGO (Figure 4.6b). The sustainability of supercapacitors depends on the response of material at every switchable current input. The rGO supercapacitor was subjected for beyond 15k and 30k cycles at different current densities. After first set of 5 k cycles at 15 A/g, capacitance retention was 100% which was continued for next 5k cycles at 10 A/g. Interestingly, when current density was switched back to 15 A/g for 5k cycles and 10 A/g for next 500 cycles, capacitance value came to its initial value, overall suggesting that the sudden variation of current density could not alter the capacitive performance of rGO materials (Figure 4.6c). Similar observation was realised when rGO supercapacitors was subjected for longer cycles at different current densities of 15 →20→15 A/g (Figure 4.6d).

Plenty of literatures on rGO based materials are aiming to enhance the energy density since the cycle life is already high. However, most of them realised the imbalance of capacitance and durability where high capacitive materials showed low cycle life and vice versa. The introduction of metal ions' additives inside the graphene layers was comprehended to bind two layers and contribute towards the overall enhancement of energy storage efficiency. However, most of the rGO-metal oxide composites are not able to sustain in acidic medium for longer time and collapsed because of the metal etching by the acid. To address this issue, functional groups of rGO could be utilised in making hybrid materials, hence supercapacitors, where suitable metal ions can be chemically attached (already discussed in chapter 1).

We have changed the acid from HCl (0.5 M) to HF (4 M) for etching and analysed the material for all solid-state supercapacitor application. After thorough investigation of the material by XPS, PXRD, Raman, approximately 5% of Cu(II) species probably as Cu_xO_y was observed, which was then named as Cu-rGO (Figures 4.7, 4.8a). Cu-rGO was then drop casted on grafoil and all solid-state supercapacitor was fabricated in 10 as well as 20 wt% H_2SO_4 in PVA-H_2SO_4

GPE. The capacitance of rGO in 10 wt% was found to be around 160 F/g at a current density of 1 A/g which was then increased to ~265 F/g in 20 wt% GPE (Figure 4.8b). Also, the increment was observed in E_d and P_d values of Cu-rGO in 20 wt% H_2SO_4 in PVA-H_2SO_4 as compared to 10 wt% (Figure 4.8c). Finally, we have performed 670 k cycles in 10 wt% PVA-H_2SO_4 and 301 k cycles in 20 wt% H_2SO_4 in PVA-H_2SO_4 GPE at relatively higher current density of 20 A/g and observed outstanding stability (Figures 4.8d, e). The capacitance of Cu-rGO in both the GPEs was found to be 100% retained which is noteworthy (Figures 4.8d, e). So, overall insertion of small quantity of Cu(II) species not only enhanced the overall capacitance, E_d, and P_d values but also imparted rigidity to the graphene network to sustain longer life cycle.

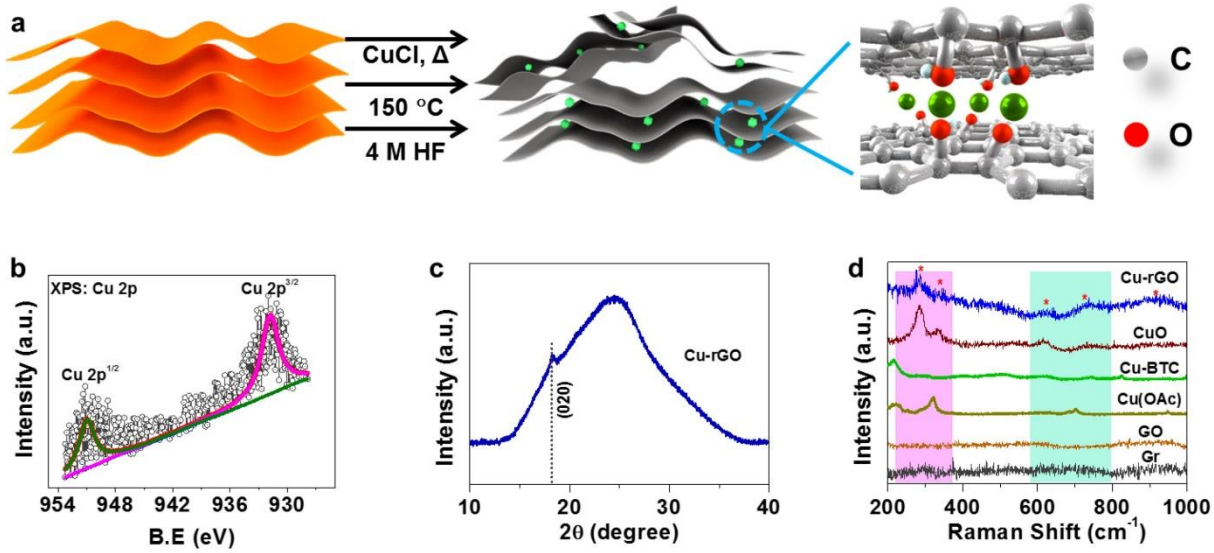

Figure 4.7. *(a) Schematic presentation of Cu-rGO synthesis. (b) Cu 2p XPS of Cu-rGO. (c) PXRD of Cu-rGO and (d) Raman spectra of Gr, GO, and Cu-rGO, compared with copper(II) oxide (CuO), copper-1, 3, 5-benzenetricarboxylic acid (Cu-BTC), copper(II) acetate (Cu(OAc)).*

To confirm the retention and sustainability of Cu-rGO, we have recorded the CD cycles at different current densities consecutively, at 15 A/g, 20 A/g and again at 15 A/g again, for 25 k cycles each. After first set of 25 k cycles at 15 A/g, capacitance retention was 100% which was then switched to 20 A/g and continued for next 25 k cycles, where only <5% loss of capacitance was observed. Interestingly, when current density was switched back to 15 A/g for next 25 k cycles, capacitance value came to its initial value, overall suggesting that the sudden variation of current density could not alter the capacitive performance of Cu-rGO materials (Figure 4.8f).

At this stage, we could say that the balanced concentration of suitable additives could drastically enhance the electrochemical performance of rGO based materials.

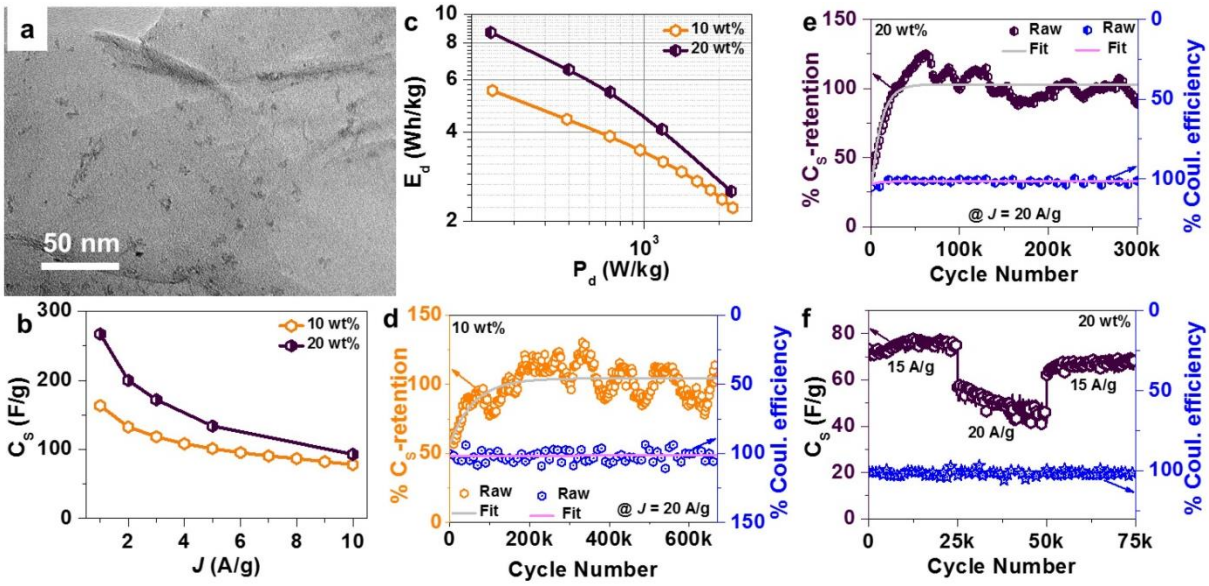

Figure 4.8. *(a) TEM image of Cu-rGO. (b) C_S versus current density (J) plots, and (c) E_d and P_d, plots of rGO all solid-state supercapacitors in 10 and 20 wt% H_2SO_4 in PVA-H_2SO_4 GPE (d-e) Durability cycles at a current density of 20 A/g, of rGO all solid-state supercapacitors in 10 wt% and 20 wt% H_2SO_4 in PVA-H_2SO_4 GPE respectively and (f) Durability cycles at different current densities (switching of J consecutively after 25000 cycles), of rGO all solid-state supercapacitors in 10 wt% PVA-H_2SO_4 GPE.*

Table 4.1. *Comparative assessments of rGO and Cu-rGO with the reported literatures.*

Materials	[R]*	M**	C_S***	Electrolyte	Cycles	Ret.	Max. E_d	Max. P_d	Refs.
rGO	**CuCl**	**1 mg/cm²**	**240 F/g @ 1 A/g**	**10 wt% PVA-H_2SO_4**	**100k @ 20 A/g**	**>80%**	**8.1 Wh/kg**	**2.2 kW/kg**	**Our Work**
rGO	**CuCl**	**1 mg/cm²**	**310 F/g @ 1 A/g**	**20 wt% PVA-H_2SO_4**	**100k @ 20 A/g**	**>80%**	**10.3 Wh/kg**	**2.3 kW/kg**	
Cu-rGO	**CuCl**	**1 mg/cm²**	**161 F/g @ 1 A/g**	**10 wt% PVA-H_2SO_4**	**>650k @ 20 A/g**	**100%**	**5.5 Wh/kg**	**2.3 kW/kg**	
Cu-rGO	**CuCl**	**1 mg/cm²**	**267 F/g @ 1 A/g**	**20 wt% PVA-H_2SO_4**	**>300k @ 20 A/g**	**100%**	**8.7 Wh/kg**	**2.2 kW/kg**	
rGO	$FeCl_2$	0.9 mg/cm²	171 F/g @ 1 A/g	10 wt% PVA-H_2SO_4	100k @ 22 A/g	>80%	6.2 Wh/kg	5.7 kW/kg	[4]
rGO	Li in molten LiCl-KCl	~6 mg		6 M KOH	2k @ 0.5 A/g	97%	---	---	[19]

			203 F/g @ 0.2 A/g						
Porous graphene frameworks	$NaBH_4$	---	186 F/g @ 1 A/g	6 M KOH	5k @ 10 A/g	97%	3.4 Wh/kg	4.6 kW/kg	20
rGO	Ascorbic acid	0.2 mg/cm^2	181.3 F/g @ 1A/g	10 wt% PVA-H_3PO_4	-----	----	6.3 Wh/kg	70.8 kW/kg	3
3D porous rGO-1		0.2 mg/cm^2	284.2 F/g @ 1A/g				9.9 Wh/kg	282 kW/kg	
3D porous rGO-2		0.41 mg/cm^2	265.5 F/g @ 1A/g				9.2 Wh/kg	135 kW/kg	
3D porous rGO-5		1.02 mg/cm^2	241.5 F/g @ 1A/g				8.3 Wh/kg	58.3 kW/kg	
Graphene hydrogel films	Ascorbic acid	~2 mg/cm^2	186 F/g @ 1 A/g	10 wt% PVA-H_2SO_4	10k @ 10 A/g	92%	0.61 Wh/kg	0.67 kW/kg	21
PVA-Graphene	HI	---	124 F/g @ 1 A/g	10 wt% PVA-H_2SO_4	1k @ 1 A/g	85%	5.32 mW h g-1	23.9 mW g-1	22
rGO/CB	N2H4	~1-2 mg	110 F/g @ 5 mV/s	10 wt% PVA-H_2SO_4	5k @ 0.58 A/g	96%	---	---	23
Porous graphene on carbon cloth	H_2 thermal reduction	---	184.36 F/g @ 5 mV/s	10 wt% PVA-H_2SO_4	1k @ 2 A/g	>95%	1.64 Wh/kg	670.0 W/kg	24
Holey graphene frameworks	sodium ascorbate	~1 mg/cm2	201 F/g at 1 A/g	10 wt% PVA-H_2SO_4	10k @ 10 A/g	90%	---	---	25
rGO	N_2H_4	5.0–7.0 mg cm^2	41.5 F/g @ 0.1 A/g	6 M KOH	---	---	1.3 Wh/kg	2.8 kW/kg	26
Graphene	N_2H_4	1.0 mg/cm2	203~192 @ 0.1 A/g	1 M H_2SO_4	50k @ 100 A/g	90%	7.05~8.87 Wh/kg	---	27
Graphene-paper	N_2H_4	~0.3-0.4 mg	136 F/g @ 10 mV/s	6 M KOH	2k @ 10 A/g	96%	4.8 Wh/kg	5.1 kW/kg	28
Graphene-gel	Vitamin C	~0.35 mg/cm^2	45.6 mF/cm^2 @ 0.67 mA/cm^2	5M KOH	10k @10 mA/cm^2	90%	---	---	29
rGO	N_2H_4	~0.5 mg/cm2	110 F/g @ 0.5 A/g	1M $LiPF_6$	---	---	---	---	30

MR-GO	Thermal reduction	~0.5 mg/cm2	210 F/g @ 0.5 A/g	1M $LiPF_6$	20k @ 2 A/g	96%	Between 7-15 Wh/kg	10^3 W/kg	
f-rGO	N_2H_4	---	118.5 F/g @ 1 A/g	Nafion-H_2SO_4	1k @ 1 A/g	>80%	---	---	[31]
Graphene-sheet	Zn powder	---	86 F/g @ 1 A/g	6 M KOH	5k @ 5 A/g	112%	---	---	[32]
Graphene-sheet	N_2H_4	10 mg/cm^2	~140 F/g @ 1 A/g	1M H_2SO_4	10k @ 0.5 A/g	95 %	---	---	[33]
			~160 F/g @ 1 A/g	6 M KOH	10k @ 0.5 A/g	95 %	---	---	
Chemically modified graphene	N_2H_4	Whole electrode weight 7.5 mg	135 F/g @ 10mA	5.5 M KOH	---	---	4.69 Wh/kg	1.78 kW/kg	[34]

4.4. Conclusions

In conclusions, for the first time, high-quality rGO was successfully produced by wet chemical synthesis of GO using CuCl as a reducing agent. The high surface area (~360 m^2/g) and electrical conductivity (150 S/m) of rGO fulfilled the criteria to be a supercapacitive material, thus, persuaded us to fabricate all solid-state supercapacitors in 10 as well as 20 wt% H_2SO_4 in 10 wt% PVA (PVA-H_2SO_4 GPE). Remarkably, the C_S values of rGO in 10 and 20 wt% were found to be as high as ~240 F/g and ~310 F/g at a current density of 1 A/g, respectively. Durability (>100000 cycles with >80% C_S retention) of rGO supercapacitors was realised to be impressive. Sustainability of rGO device was estimated after recording the multiple CD cycles (>30k) by switching the current density from 15→20→15 A/g and C_S retention was found to be 100% in each case. Our results recommend the use of ecofriendly aqueous electrolytes in boosting the performance of carbonaceous supercapacitors.

4.5. References

(1) Bard, A. J., Faulkner, Larry R. *Electrochemical Methods: Fundamentals and Applications*. Wiley: New York, 1980.

(2) Cotton, F. A.; Wilkinson, G. *Advanced Inorganic Chemistry*. Wiley: New York, 1972.

(3) Shao, Y.; El-Kady, M. F.; Lin, C. W.; Zhu, G.; Marsh, K. L.; Hwang, J. Y.; Zhang, Q.; Li, Y.; Wang, H.; Kaner, R. B. 3D Freeze-Casting of Cellular Graphene Films for Ultrahigh-Power-Density Supercapacitors. *Adv. Mater.* **2016**, *28*, 6719-6726.

(4) Jha, P. K.; Singh, S. K.; Kumar, V.; Rana, S.; Kurungot, S.; Ballav, N. High-Level Supercapacitive Performance of Chemically Reduced Graphene Oxide. *Chem* **2017**, *3*, 846-860.

(5) Chua, C. K.; Pumera, M. The Reduction of Graphene Oxide with Hydrazine: Elucidating Its Reductive Capability Based on a Reaction-Model Approach. *Chem. Commun.* **2016**, *52*, 72-75.

(6) Chua, C. K.; Pumera, M. Reduction of Graphene Oxide with Substituted Borohydrides. *J. Mater. Chem. A* **2013**, *1*, 1892-1898.

(7) Ferrari, A. C.; Robertson, J. Interpretation of Raman Spectra of Disordered and Amorphous Carbon. *Phys. Rev. B* **2000**, *61*, 14095-14107.

(8) Moon, I. K.; Lee, J.; Ruoff, R. S.; Lee, H. Reduced Graphene Oxide by Chemical Graphitization. *Nat. Commun.* **2010**, *1*, 73.

(9) Jung, S. M.; Mafra, D. L.; Lin, C.-T.; Jung, H. Y.; Kong, J. Controlled Porous Structures of Graphene Aerogels and Their Effect on Supercapacitor Performance. *Nanoscale* **2015**, *7*, 4386-4393.

(10) Sun, X.; Cheng, P.; Wang, H.; Xu, H.; Dang, L.; Liu, Z.; Lei, Z. Activation of Graphene Aerogel with Phosphoric Acid for Enhanced Electrocapacitive Performance. *Carbon* **2015**, *92*, 1-10.

(11) Groen, J. C.; Peffer, L. A. A.; Pérez-Ramírez, J. Pore Size Determination in Modified Micro- and Mesoporous Materials. Pitfalls and Limitations in Gas Adsorption Data Analysis. *Micropor. Mesopor. Mat.* **2003**, *60*, 1-17.

(12) Chua, C. K.; Pumera, M. Chemical Reduction of Graphene Oxide: A Synthetic Chemistry Viewpoint. *Chem. Soc. Rev.* **2014**, *43*, 291-312.

(13) Conway, B. E. *Electrochemical Supercapacitors: Scientific Fundamentals and Technological Applications*. Springer Science & Business Media: 2013.

(14) Casero, E.; Parra-Alfambra, A. M.; Petit-Domínguez, M. D.; Pariente, F.; Lorenzo, E.; Alonso, C. Differentiation between Graphene Oxide and Reduced Graphene by Electrochemical Impedance Spectroscopy (EIS). *Electrochem. Commun.* **2012**, *20*, 63-66.

(15) Augustyn, V.; Come, J.; Lowe, M. A.; Kim, J. W.; Taberna, P.-L.; Tolbert, S. H.; Abruña, H. D.; Simon, P.; Dunn, B. High-Rate Electrochemical Energy Storage through Li^+ Intercalation Pseudocapacitance. *Nat. Mater.* **2013**, *12*, 518-522.

(16) Lin, T.; Chen, I.-W.; Liu, F.; Yang, C.; Bi, H.; Xu, F.; Huang, F. Nitrogen-Doped Mesoporous Carbon of Extraordinary Capacitance for Electrochemical Energy Storage. *Science* **2015**, *350*, 1508-1513.

(17) Gogotsi, Y.; Simon, P. True Performance Metrics in Electrochemical Energy Storage. *Science* **2011**, *334*, 917-918.

(18) Hwang, J. Y.; El-Kady, M. F.; Li, M.; Lin, C.-W.; Kowal, M.; Han, X.; Kaner, R. B. Boosting the Capacitance and Voltage of Aqueous Supercapacitors Via Redox Charge Contribution from Both Electrode and Electrolyte. *Nano Today* **2017**, *15*, 15-25.

(19) Abdelkader, A. M.; Vallés, C.; Cooper, A. J.; Kinloch, I. A.; Dryfe, R. A. W. Alkali Reduction of Graphene Oxide in Molten Halide Salts: Production of Corrugated Graphene Derivatives for High-Performance Supercapacitors. *ACS Nano* **2014**, *8*, 11225-11233.

(20) Yuan, K.; Xu, Y.; Uihlein, J.; Brunklaus, G.; Shi, L.; Heiderhoff, R.; Que, M.; Forster, M.; Chassé, T.; Pichler, T., *et al.* Straightforward Generation of Pillared, Microporous Graphene Frameworks for Use in Supercapacitors. *Adv. Mater.* **2015**, *27*, 6714-6721.

(21) Xu, Y.; Lin, Z.; Huang, X.; Liu, Y.; Huang, Y.; Duan, X. Flexible Solid-State Supercapacitors Based on Three-Dimensional Graphene Hydrogel Films. *ACS Nano* **2013**, *7*, 4042-4049.

(22) Chen, S.; Ma, W.; Xiang, H.; Cheng, Y.; Yang, S.; Weng, W.; Zhu, M. Conductive, Tough, Hydrophilic Poly (Vinyl Alcohol)/Graphene Hybrid Fibers for Wearable Supercapacitors. *J. Power Sources* **2016**, *319*, 271-280.

(23) Wang, Y.; Chen, J.; Cao, J.; Liu, Y.; Zhou, Y.; Ouyang, J.-H.; Jia, D. Graphene/Carbon Black Hybrid Film for Flexible and High Rate Performance Supercapacitor. *J. Power Sources* **2014**, *271*, 269-277.

(24) Wang, S.; Pei, B.; Zhao, X.; Dryfe, R. A. W. Highly Porous Graphene on Carbon Cloth as Advanced Electrodes for Flexible All-Solid-State Supercapacitors. *Nano Energy* **2013**, *2*, 530-536.

(25) Xu, Y.; Chen, C.-Y.; Zhao, Z.; Lin, Z.; Lee, C.; Xu, X.; Wang, C.; Huang, Y.; Shakir, M. I.; Duan, X. Solution Processable Holey Graphene Oxide and Its Derived Macrostructures for High-Performance Supercapacitors. *Nano lett.* **2015**, *15*, 4605-4610.

(26) Lei, Z.; Christov, N.; Zhao, X. S. Intercalation of Mesoporous Carbon Spheres between Reduced Graphene Oxide Sheets for Preparing High-Rate Supercapacitor Electrodes. *Energy Environ. Sci.* **2011**, *4*, 1866-1873.

(27) Yang, X.; Cheng, C.; Wang, Y.; Qiu, L.; Li, D. Liquid-Mediated Dense Integration of Graphene Materials for Compact Capacitive Energy Storage. *Science* **2013**, *341*, 534-537.

(28) Wang, G.; Sun, X.; Lu, F.; Sun, H.; Yu, M.; Jiang, W.; Liu, C.; Lian, J. Flexible Pillared Graphene-Paper Electrodes for High-Performance Electrochemical Supercapacitors. *Small* **2012**, *8*, 452-459.

(29) Chen, J.; Sheng, K.; Luo, P.; Li, C.; Shi, G. Graphene Hydrogels Deposited in Nickel Foams for High-Rate Electrochemical Capacitors. *Adv. Mater.* **2012**, *24*, 4569-4573.

(30) Lee, J. H.; Park, N.; Kim, B. G.; Jung, D. S.; Im, K.; Hur, J.; Choi, J. W. Restacking-Inhibited 3d Reduced Graphene Oxide for High Performance Supercapacitor Electrodes. *ACS Nano* **2013**, *7*, 9366-9374.

(31) Choi, B. G.; Hong, J.; Hong, W. H.; Hammond, P. T.; Park, H. Facilitated Ion Transport in All-Solid-State Flexible Supercapacitors. *ACS Nano* **2011**, *5*, 7205-7213.

(32) Liu, Y.; Li, Y.; Zhong, M.; Yang, Y.; Yuefang, W.; Wang, M. A Green and Ultrafast Approach to the Synthesis of Scalable Graphene Nanosheets with Zn Powder for Electrochemical Energy Storage. *J. Mater. Chem.* **2011**, *21*, 15449-15455.

(33) Fan, L.-Z.; Liu, J.-L.; Ud-Din, R.; Yan, X.; Qu, X. The Effect of Reduction Time on the Surface Functional Groups and Supercapacitive Performance of Graphene Nanosheets. *Carbon* **2012**, *50*, 3724-3730.

(34) Stoller, M. D.; Park, S.; Zhu, Y.; An, J.; Ruoff, R. S. Graphene-Based Ultracapacitors. *Nano Lett.* **2008**, *8*, 3498-3502.

Chapter 5

Reduced Graphene Oxide-Polyaniline Nanocomposites for Supercapacitor Applications

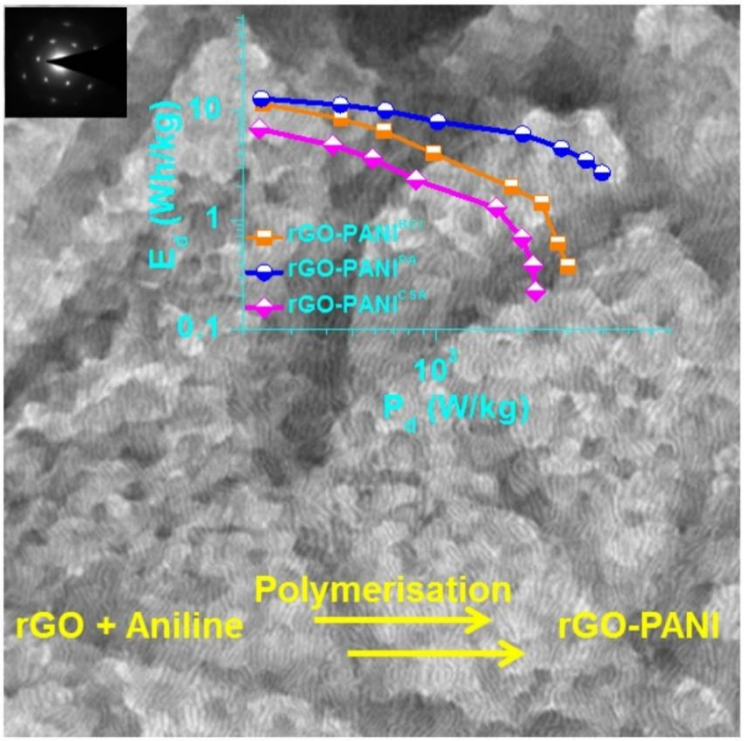

5.1. Introduction

Conducting polymers are so-called organic polymers that can conduct electricity. Among conducting polymers – polyaniline (PANI), polypyrrole (PPy), polyacetylene (PAc), poly(3,4-ethylenedioxythiophene) (PEDOT) etc., it is PANI which is highly acclaimed to the scientific community due to its multiple redox states, high conductivity, and ambient stability.[1-3] Theoretically, PANI could exhibit specific capacitance value ~2000 F/g, however, the poor cycle stability restricted its practical application at industrial scale.[4-8] On the other hand, pure reduced graphene oxide (rGO) could be stable over long cycle (>100000), yet comparatively low capacitance values (<150 F/g) still needs a special attention to amplify its overall performance.[9] There are numerous methods/approaches to enhance the supercapacitive performance of both the candidates, where one highly acceptable approach is the blending of PANI and rGO.[10] Therefore, blending of materials could boosts the supercapacitor performance along with durability due to the synergistic effect. Though, recent literatures of rGO-PANI composites demonstrated synergism, both stability and high capacity of rGO-PANI materials at the same time is still a major challenge (Table 5.1).

In this chapter, we have demonstrated the supercapacitance performance of two PANI based system: (1) PANI emeraldine salt (ES)[6], which was isolated from nanocrystals of Pb(II) ion and PANI ES[11] nanocomposite and (2) Hybrid of rGO-PANI, which was synthesised through in-situ polymerisation of aniline in the presence of rGO.

Firstly, a detail study on EB-Pb and ES preparations can be found in references 6 and 11.

Secondly, the rGO-PANI nanocomposites were synthesised based on the following analysis: PANI salt and rGO both have π-conjugation, thus, both could directly interact during the self-assembly. However, the next coming layers of PANI supposed to be interacting comparatively more with first PANI layers rather to rGO, in order to form self-assembled nanowire arrays. We anticipated that only first few layers of PANI must directly influenced by the π-conjugated rGO sheets whereas rest PANI layers may be acting as a bulk. This could be the reason behind PANI degradation on continuous charge-discharge cycles over time and reduction of the overall capacitance performance.[12] The rGO prepared in chapter 2 was harmonized with PANI and investigate the electrochemical performance.

The upper layers of PANIs of rGO-PANI composites are not strongly bound to the surface, hence can pose a negative impact during durability cycles. Therefore, rGO-PANI powders were dispersed in DMSO via ultra-sonication and centrifuged to remove the loosely bound PANI. The rGO-PANI composites were doped with different inorganic and organic acids – hydrochloric acid (HCl), camphor sulfonic acid (CSA), and phytic acid (PA), intrinsically and extrinsically. A detailed study of PANI concentration and doping of acids in rGO-PANI composites revealed an interesting fact about the pursuance of both on electrochemical performance.

5.2. Materials and Method

Aniline, ammonium persulfate (APS), (1S)-(+)-10-camphorsulfonic acid (CSA), polyaniline emeraldine base (EB; M_w = 50000), and lead nitrate ($Pb(NO_3)_2$) were purchased from Sigma-Aldrich, where aniline was further distilled and others used without any modifications. Ammonia solution, MeOH, DMSO, and HCl were purchased from RANKEM (India). Phytic acid (PA) purchased from TCI chemicals. 18.2 MΩ Millipore (MQ) water was used.

To prepare EB-Pb, EB (~102 mg) was dispersed in DMSO (12-14 ml) and diluted with MeOH (80 ml). In another conical flask about 1.41 gm $Pb(NO_3)_2$ was dissolved in 80 ml of MQ water. Both solution were mixed together and left undisturbed for 24 hr. The precipitates was collected, washed with MeOH until the blue colour disappeared, vacuum dried at 70 °C, and named EB-Pb. Further, EB-PB powder was exposed with HCl vapour in order to remove the Pb(II) ions and doping with H^+ ions and resulted powder was named as ES1. For control EB was directly exposed with HCl favour and named as ES2.

GO and rGO synthesis is described in chapter 1. The pre-dried black residue of rGO re-dispersed in water. All protonic acid doped rGO-PANI nanocomposites were synthesised in similar reaction condition. About 10 ml aqueous rGO (~4 mg/mL) dispersion was mixed with 250 µl aniline and acids (HCl ~ 90 µL, CSA ~640 mg, and PA ~2.49 ml) and stirred for ~6 hr on ice bath (T<5 °C). About 600 mg APS was dispersed in 2 mL MQ H_2O, and left undisturbed for 1 hr at room temperature. After ~6 hr, APS solution was added dropwise into the mixture and stirred for next 24 hr at same condition (T<5 °C). The green colour residues were filtered, washed with H_2O/MeOH, and 50 ml of 0.5 M respective acids, finally, ringed with water and vacuum dried at 100 °C for 10 hr.

To remove un-bounded/loosely bounded PANI, rGO-PANI nanocomposites were re-dispersed in DMSO and sonicated, centrifuged for several times until the supernatant became colourless (indication of the removal of all the unwanted PANI). The residues were thoroughly washed with water, Methanol and vacuum dried at 70 °C for 10 hr. The black powders were soaked in 1 M respective acids and stirred for 12 hr at RT. The protonic acid doped nanocomposites were named as rGO-PANI^{acid} (acid = HCl, CSA, and PA) were well characterised and then subjected for supercapacitor testing.

The slurry of EB, ES1, and ES2 (in NMP) were drop casted on Toray carbon paper and dried under IR lamp for 12-15 hr. Electrochemical performance was evaluated in 0.5 M H_2SO_4 electrolyte solution using two electrode setup.[6]

10 wt% PVA-H_2SO_4 Gel Preparation is as described in chapter 2. Fabrication of all solid-state supercapacitors for rGO-PANI nanocomposites is as described in chapter 2. The loading of all active materials were ~1 mg/cm^2.

5.3. Results and Discussion

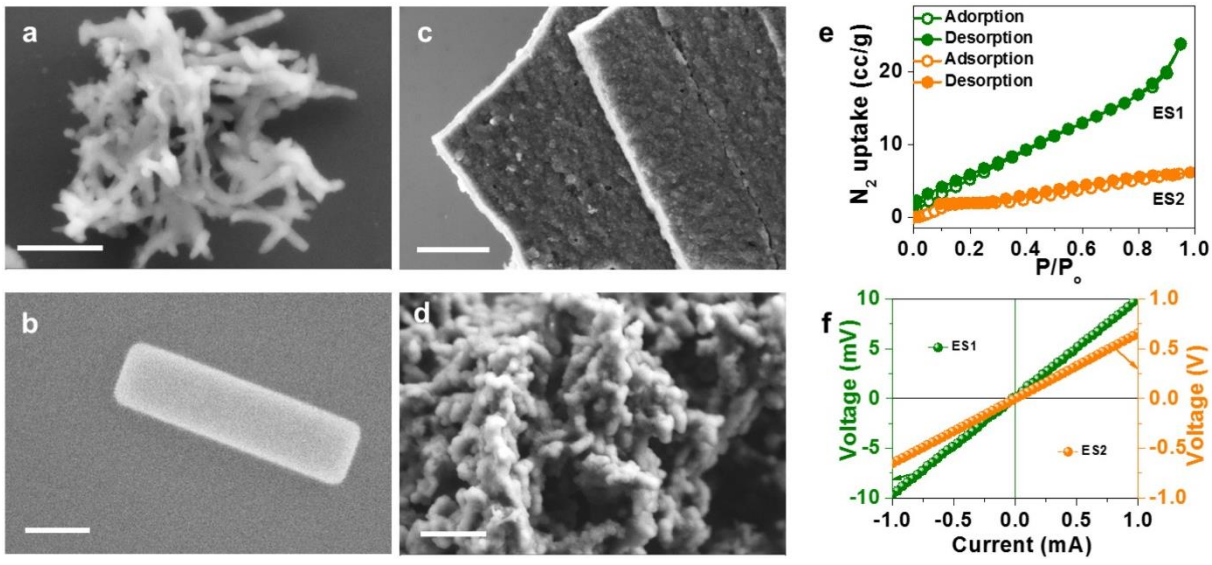

Figure 5.1. *(a-d) FESEM images of EB, EB-PB, ES1, and ES2. Scale bars are 500 nm, 1 µm, 100, and 200 nm, respectively. (e) N_2 adsorption-desorption isotherms of ES1 and ES2 at 77 K and (f) DC I-V plots of ES1 and ES2.*

The discussion of EB-PB, ES1, and ES2 can be found in references 6 and 11. The Pb(II) ions are acting as template in EB-Pb. The adopted methodology of slow exposure of HCl vapour to EB-Pb nanomaterial generated ES1 with unique morphology, porosity and electrical conductivity. The FESEM images of EB, EB-Pb, ES1, and ES2 is shown in Figure 5.1. EB has fibre like morphology (Figure 5.1a) which after binding with Pb(II) forms hierarchical self-assembly with Pb(II) ions and transformed into nanocuboid structure (Figure 5.1b). The exposer of HCl vapour successfully removed Pb(II) ions, left behind relatively larger layered ES1 backbone (Figure 5.1c). ES2 showed a globular morphology (Figure 5.1d). The BET surface area (Figure 5.1e) and electrical conductivity (Figure 5.1f) of ES1 were found to be ~30 m^2/gm (average pore diameter ~ 10 Å) and 0.1 S/cm, respectively, which were found to be larger than ES2 and comparable to or higher than other reported PANI materials.[6]

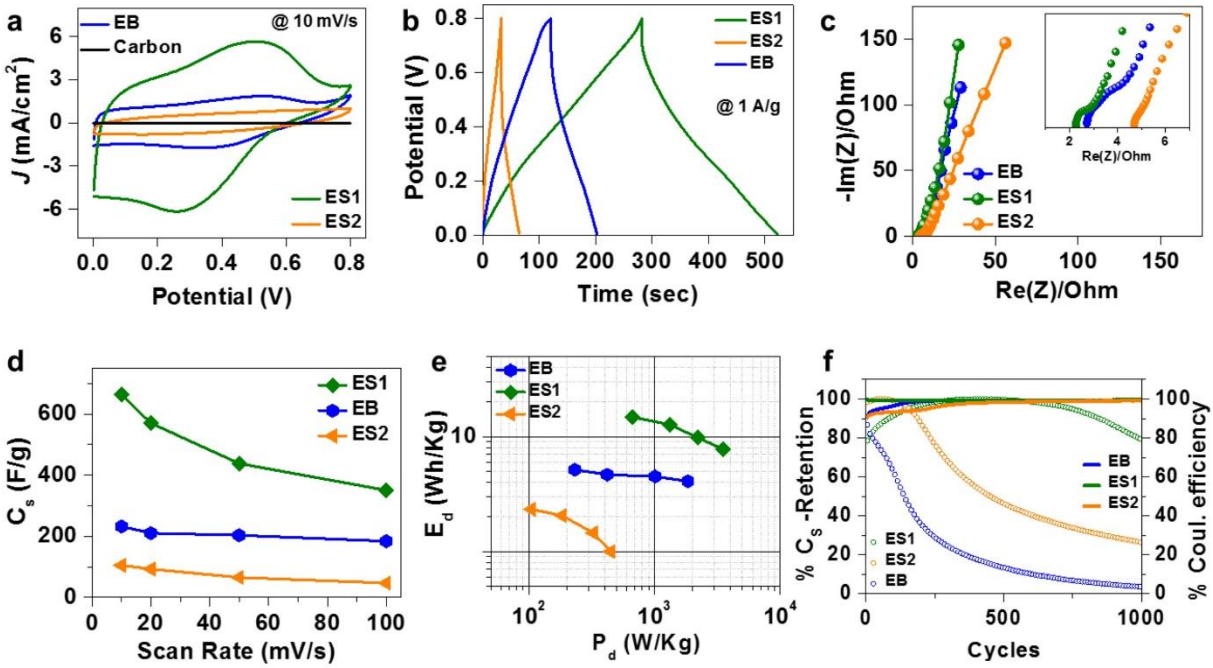

Figure 5.2. *(a-c) CV, CD, and Nyquist (inset: zoomed in Nyquist plot) plots of EB, ES1, and ES2. (d-f) C_S against scan rate, Ragone plot, and durability at a current density of 5 A/g, of EB, ES1, and ES2.*

The electrochemical performance of EB, ES1, and ES2 were evaluated from cyclic voltammetry (CV), charge-discharge (CD), and impedance spectroscopy (EIS) techniques (Figure 5.2). The CV was recorded from 10 to 100 mV/s (not shown here), where at a scan rate of 10 mV/s, charge storage in ES1 realised to be highest compared to other two EB and ES2 (Figure 5.2a). The oxidation-reduction peaks in CV actually validating the pseudocapacitive behaviour of PANI backbones. CD characterisation also corroborating with CV (Figure 5.2b).

From Nyquist the R_S (~2.2 Ω) of ES1 at high frequency found to be smaller compared to EB and ES2, whereas R_{CT} of ES1 (~0.6 Ω) observed to be similar to that of ES2 and smaller than EB (Figure 5.2c). The specific capacitance of all the materials (C_S) were calculated from scan rate. Remarkably, ES1 showed very high capacitance value to be around 660 F/g at a scan rate of 10 mV/s which was retained more than 50% at higher scan rate of 100 mV/s (Figure 5.2d). The maximum energy density (E_d) and powder density (P_d) of ES1 calculated to be around 14.8 Wh/kg and 3.5 kW/kg respectively (Figure 5.2e). Finally, all the materials were subjected for 1100 continuous CD cycles at a current density of 5 A/g and interestingly, for ES1 ~80% C_S retention was observed (Figure 5.2f). Altogether, the electrochemical performance of ES1 was found to be higher in compared to EB and ES2 and comparable/ higher than other reported PANI materials. Although PANI (ES2) showed remarkable capacitive performance, the cycle stability still could be a disadvantage. Therefore, blending of PANI with rGO could boost the durability along with high capacitance value, synergistically.[12-13]

Here used rGO was already synthesised and tested spectroscopically, microscopically, and electrochemically in the chapter 2. The in-situ chemical polymerisation of aniline was realised in presence of rGO.

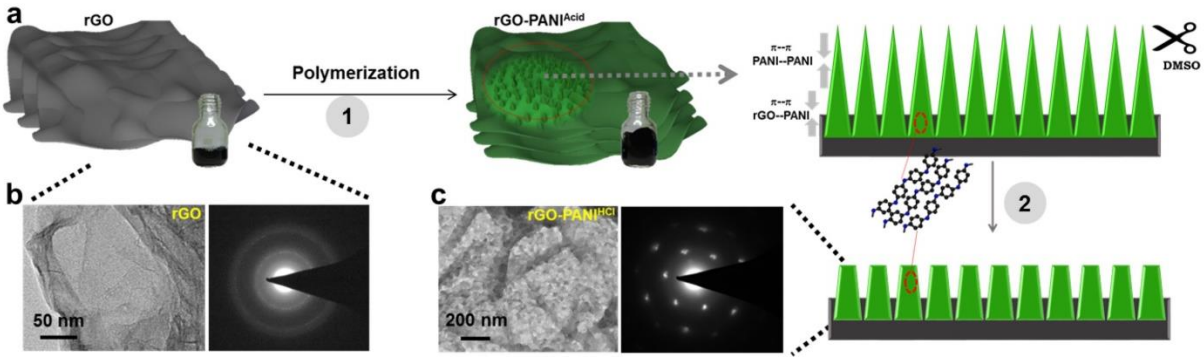

Figure 5.3. *(a) Schematic of rGO-PANI nanocomposites synthesis (1) and DMSO treatment (2), and (b,c) TEM images and SAED patterns of rGO and rGO-PANI^{HCl} material.*

The concentration of aniline directly affects the competition of nanowire formation and random polymerisation on the graphene substrate. On dilute aniline concentration, highly active nucleation sites will be generated which in turn reduce the interfacial energy barrier between solid and bulk solution for the advancement of aligned PANI on the substrate.[12]

Here, we have employed a very low concentration of aniline (~0.25 M) to obtain a high quality and aligned PANI layers on rGO template. Moreover, the rGO-PANI composites were thoroughly washed with polar solvents in order to remove the unwanted and weakly bounded (weak π-π between PANI-PANI) PANI from the rGO-PANI nanocomposites. Afterwards, the rest attached PANI to the rGO sheets validates the hierarchical self-assembly of nanocomposites due to strong π-π interaction among PANI chains and with rGO sheets (Figure 5.3). FESEM images of rGO-PANI^{acid} nanocomposites revealed homogeneously distributed PANI nanowire arrays over the rGO template (Figures 5.4a-c) which was further complemented by the TEM image in the case of rGO-PANI^{HCl}, where a very thin PANI nanowires can be visible (Figure 5.4d). In TEM image, a patterned self-assembled rGO sheets emphasizing the control blending approach of the nanocomposite synthesis. Interestingly, hexagonal spots can be observed in the selected area electron diffraction (SAED) of rGO-PANI^{HCl} nanocomposite suggests a semi-crystalline nature of the material (Figure 5.3c). The EDX mapping of rGO-PANI nanocomposites clearly showed the homogeneous distribution of all the elements – Cl, S, and P of acid backbones (Figures 5.4e-g).[12,14]

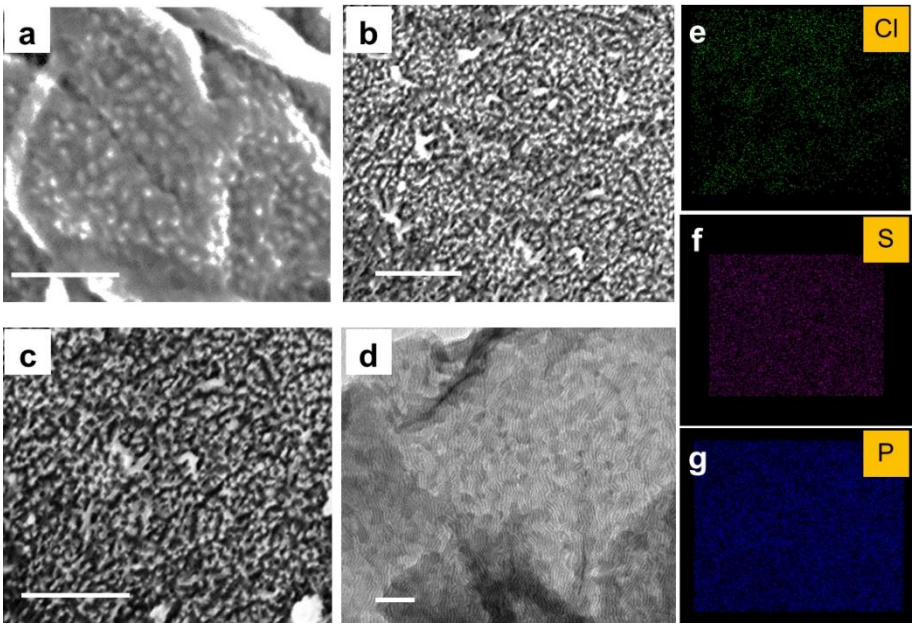

Figure 5.4. *(a-c) FESEM images of rGO-PANI^{HCl}, rGO-PANI^{CSA}, and rGO-PANI^{PA} nanocomposites. Scale bars are 0.5, 1, and 1 μm respectively. (d) TEM image of rGO-PANI^{HCl}. Scale bar is 100 nm and (e-g) EDX mapping of rGO-PANI^{HCl}, rGO-PANI^{CSA}, and rGO-PANI^{PA} nanocomposites show presence of Cl, S, and P element, respectively.*

PXRD of composites were collected for further analysis of semi-crystalline character of nanocomposites. Remarkably, in all nanocomposites, peaks can be observed at multiple diffraction angles – a signature of crystallinity (Figure 5.5a). The rGO was amorphous in nature as can be seen from SAED analysis (Figure 5.3b) and as is discussed in chapter 2.[1,15]

It has already been seen in many literatures as well as our prepared PANI salt (ES) that the PANI generally stands as an amorphous materials. However, two amorphous materials, when in-situ combined together able to self-assembled, in such a way that the product originated as a crystalline character. We anticipated, perhaps due to the control concentration of reactants and polymerisation, PANI stitches few rGO sheets together in ordered fashion. Further, FTIR, and Raman measurements were performed to affirm the presence of PANI, acids, and rGO in rGO-PANI nanocomposite (Figure 5.5). The FTIR of all composites were recorded on pressed KBr pellet. For PANI, the characteristic C=C stretching vibrations of quinoid and benzenoid appeared at ~1573 and ~1484 cm^{-1} respectively. The C-H out of plane bending of benzene can be observed at ~ 800 cm^{-1}. Also, peaks at ~1295, ~1238 and 1170 cm^{-1} are the C-N, C=N, and C-H stretching vibrations in the polarons. In case of rGO, along with sp^2 hybridised carbon other oxygenated groups are present which can be observed at ~1656, ~1735, ~1388, and ~1224 cm^{-1} for -C=C, -C=O, -C-OH, and -C-O-C- stretching vibrations. Furthermore, a characteristic peak of polyaniline salt for $–NH^+=$ group was found to be at ~3460 cm^{-1} (Figure 5.5b). The characteristic Raman peaks for PANI can be seen at ~1187, ~1237, ~1320, ~1477, and ~1620 cm^{-1} of C-H bending of quinoid ring, C-N stretching, $C\text{-}N^+$ stretching in bipolaron, C=N stretching in quinoid ring, and C=C stretching of benzenoid ring respectively. Two important broad peaks at ~1350 and ~1595 cm^{-1} can be assigned as D (defect band) and G (graphene band) bands of rGO, validates the presence of rGO backbone (Figure 5.5c). Overall, successful blending of rGO and PANI was achieved and the isolated powders were proceeded for further analysis. As mentioned in the chapter 1, porosity, electrical conductivity, morphology, and elemental composition altogether could boost the performance of supercapacitor. The porosity was extracted from the N_2 adsorption-desorption isotherm at 77 K, whereas, electrical conductivity was confirmed by four probe electrical conductivity measurement on pressed nanocomposites pellets. The electrical conductivity of rGO-PANI showed a trend as $PANI^{CSA}$ (~0.013 S/cm) < $rGO\text{-}PANI^{HCl}$ (~0.05 S/cm) < $rGO\text{-}PANI^{PA}$ (~0.21 S/cm) (Figure 5.5d).

On the other hand, the BET surface area of rGO-PANI nanocomposite followed the trend as rGO-PANI^{CSA} (~13 m^2/g) < rGO-PANI^{PA} (~26 m^2/g) < rGO-PANI^{HCl} (~33 m^2/g) (Figure 5.5e).[12,16-17] The BET surface area of rGO-PANI nanocomposites are comparable to some of the other reported rGO-PANI composite materials. Overall, electrical conductivity and porosity of the rGO-PANI materials really differs when doped with different protonic acids at similar conditions (Figure 5.5f).

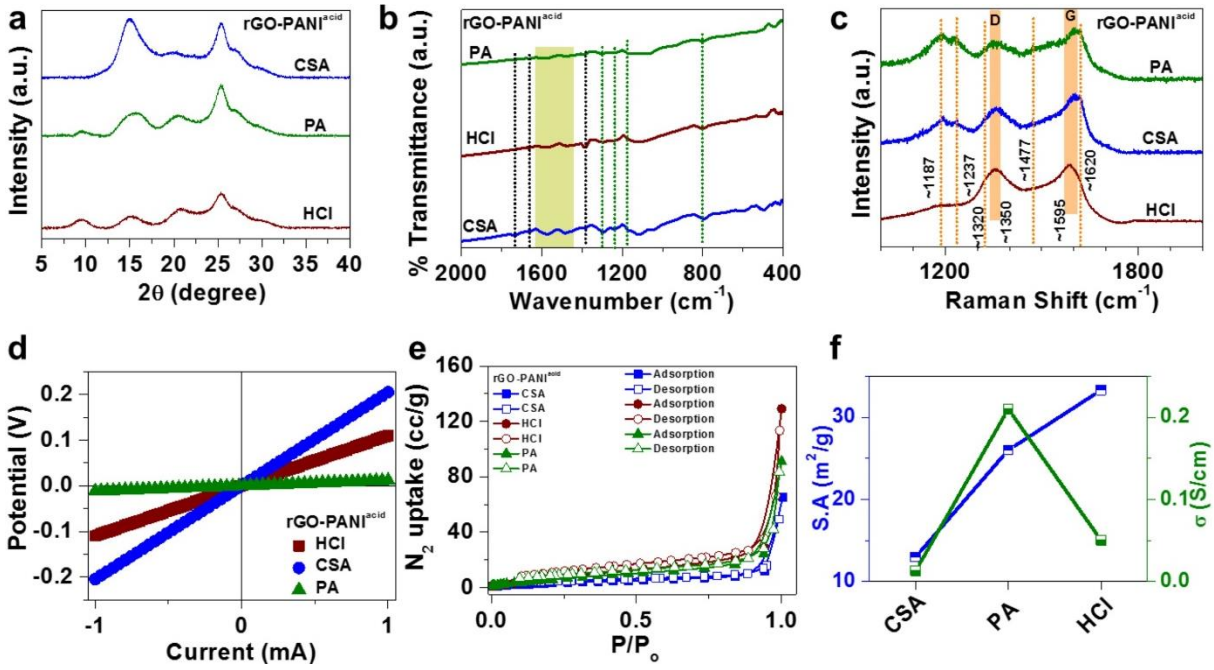

Figure 5.5. *(a-f) PXRD, FTIR, Raman, DC I-V characteristics, N_2 adsorption-desorption at 77 K, and surface area (S.A) and electrical conductivity plots of rGO-PANI nanocomposites.*

Supercapacitors made of rGO-PANI based active materials are called as a hybrid supercapacitors, because of the symbiotic contribution from EDLC (rGO) and pseudocapacitor (PANI).[18] The all solid-state supercapacitor device of rGO-PANI nanocomposites were fabricated and electrochemically characterised through CV, CD, and EIS techniques (Figure 5.6). The CV of rGO-PANIs were recorded from 5-200 mV/s scan rate (Figure 5.6a). Due to the pseudocapacitive nature[18] of PANI, oxidation and reduction peaks corresponding to leucoemeraldine (LE) → Emeraldine (E) → Pernigraniline (P), and P → E → LE, respectively, can be observed. The broader curves feature of CV at 5 mV/s in all three composites indicates the higher amount of charge storage synergistically by means of EDLC and pseudocapacitor.[6] Interestingly, CV showed different charge storage capacity of all three composites which perhaps can be explained in terms of conductivity and porosity.[14]

The electron mobility and accessible surface area of rGO-PANI nanocomposites clearly suggests the comparatively higher of same in the case of PA and HCl doped rGO-PANI, probably a reason of increased current density. CD of nanocomposites was recorded from 1-25 A/g and non-triangular curve feature suggests the pseudocapacitive characteristics, also corroborating to CV data (Figure 5.6b).[18-19]

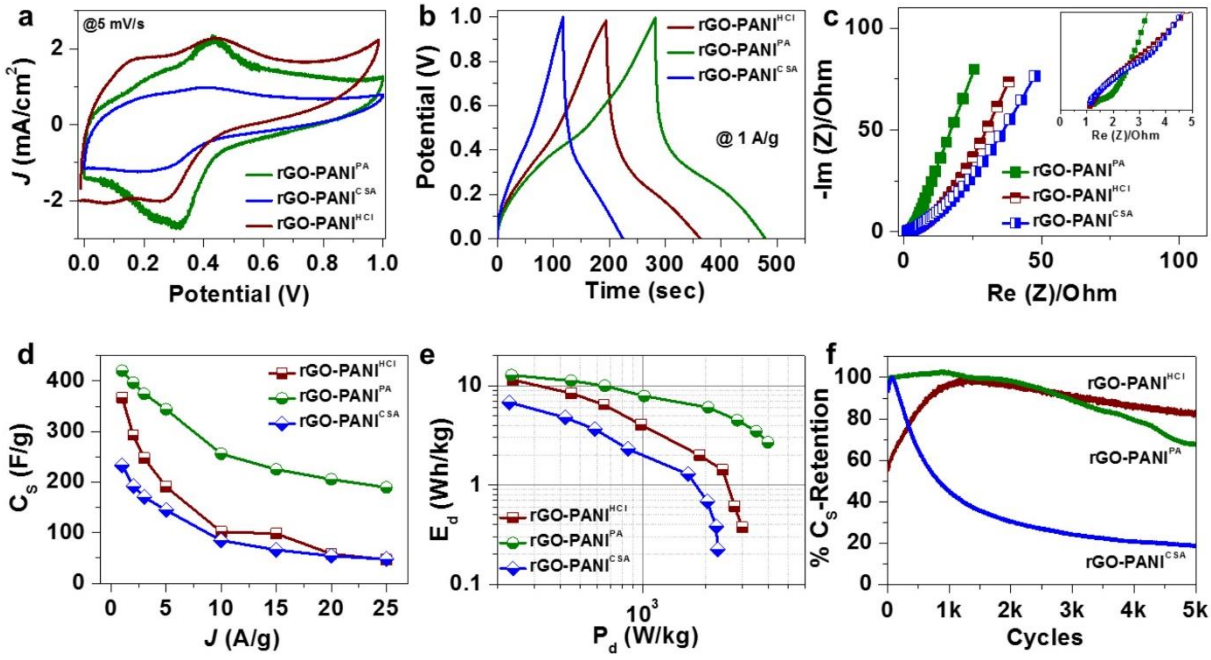

Figure 5.6. *Comparative assessment: (a-c) CV, CD, and Nyquist plots (inset: zoomed in plot). (d) C_S versus current density, (e) E_d versus P_d, and (f) Durability cycle at a current density of 5 A/g, of rGO-PANI nanocomposites.*

The charge-discharge time at a current density of 1 A/g, of rGO-PANI^{PA} is higher among all, suggest the materials accommodating higher charge onto the surface (Figure 5.6b). Also the IR drop of composites is very small, clearly indicated that the materials can have very high power density and small internal (R_S)/charge transfer (R_{CT}) resistances. From Nyquist plot (Figure 5.6c) the R_S of all the composites found to be similar [rGO-PANI^{PA} (1.27 Ω), rGO-PANI^{HCl} (1.12 Ω), and rGO-PANI^{CSA} (1.12 Ω)], however, the R_{CT} realised to be different for different composite which follow the trend as: rGO-PANI^{PA} (~0.8 Ω) < PANI^{HCl} (2.5 Ω) < rGO-PANI^{CSA} (~3.5 Ω). The ideal capacitive behaviour for rGO-PANI^{PA} is more than PANI^{HCl} and rGO-PANI^{CSA}. From Nyquist plot it is quite clear that the supercapacitive performance of PA doped can be better than the HCl doped followed by CSA doped nanocomposites. The specific capacitance (C_S) of all the materials were calculated and plotted against different current

density (*J*) (Figure 5.6d). The C_S at a current density of 1 A/g for rGO-PANI^{PA} calculated to be around 420 F/g, which is lesser for rGO-PANI^{HCl} to be ~365 F/g and comparatively very lower in the case of rGO-PANI^{CSA} to be ~230 F/g (Figure 5.6d). At higher current densities, rGO-PANI^{PA} nanocomposite performed superior than other two materials which were looked to be almost similar as soon the current density increased beyond 10 A/g. The better performance of PA doped rGO is mainly due to a balance electrical conductivity and porosity value (Figure 5.5f). Altogether, the capacitance performance of our synthesised composite found to be either comparable or higher than other reported rGO-PANI based materials (Table 5.1). Further, the energy density (E_d) and power density (P_d) were extracted from CD data (Figure 5.6e). The maximum E_d of rGO-PANI^{PA}, PANI^{HCl}, and rGO-PANI^{CSA} was calculated to be around 12.8, 11.5, and 6.8 Wh/kg, respectively, and the maximum P_d found to be around 4, 3, and 2.3 kW/kg respectively. The max E_d and P_d of rGO-PANI^{PA} is higher than other two nanocomposites as well as other reported rGO-PANI based composites. Finally, to examine the durability, all nanocomposites were subjected for 5000 CD cycles at a current density of 5 A/g. Interestingly, C_S retention of HCl doped rGO-PANI composite found to be more than 80% followed by PA doped material (~75%), however, CSA doped material degraded rapidly beyond 500 cycles (Figure 5.6f). Thus, our approach of producing high capacitive and durable rGO-PANI nanocomposites realised to be highly effective.

5.4. Conclusions

We have deigned a methodology of polyaniline salt (ES2) preparation for supercapacitor performance. The max. C_S, Ed, and P_d of ES2 found to be ~660 F/g, 14.8 Wh/kg, and 3.5 kW/kg, respectively, which are higher than other PANI based supercapacitors.[11] Even at high current density of 5 A/g, ES2 could sustain 1100 cycles with >80% C_S retention. Hybrid of rGO and PANI was synthesised through in-situ polymerisation of aniline, in order to enhance the cycle stability of rGO-PANI based system without losing much energy density in comparison to ES2. The max C_S of rGO-PANIs were found to be ~420 F/g (PA doped), ~365 F/g (HCl doped), and ~265 F/g (CSA doped) with respective energy density of ~12.8, 11.5, and 6.8 Wh/kg. All rGO-PANI nanocomposites were subjected for 5k cycles and only PA and HCl doped materials found to be >70% stable. Interestingly, HCl doped rGO-PANI could sustain >70% for 10k cycles. Our approach of removing unbound (weak π bond) PANI from rGO-PANI nanocomposite could produce high capacitive and durable material.

Table 5.1. *Comparative assessment of rGO-PANI nanocomposites with reported literatures.*

S.N.	Materials	Elec-rode Setup	Electrolyte	Cs	Cycles	Stability	Ref.
1	rGO-PANI^{PA}	**2**	10 wt% PVA-H_2SO_4	~420 F/g @ 1 A/g	5000 @ 5 A/g	~75 %	Our Work
2	rGO-PANI^{HCl}			~365 F/g @ 1 A/g		~80%	
3	rGO-PANI^{CSA}			~230 F/g @ 1 A/g		~20 %	
4	PANI-rGO	2	1 M H_2SO_4	~325 F/g @ 0.5 A/g	2000 @1A/g	92%	[12]
5	PANI/graphene	2	PVA-H_3PO_4	~261 F/g @ 0.38 A/g	1000 @ 1A/g	89%	[20]
6	PANI-GNR	2	1 M H_2SO_4	~340 F/g @ 0.25 A/g	4200 @ 1A/g	90%	[16]
7	rGO/PANI	2	1 M H_2SO_4	~439 F/g @ 0.5 A/g	2000 @ 4A/g	76.5%	[21]
8	G-PNF30	2	1 M H_2SO_4	~210 F/g @ 0.3 A/g	800 @ 3 A/g	74%	[17]
9	PANI derived-graphene	2	2 M H_2SO_4	~400 F/g @ 5 mV/s	---	---	[22]
10	3D-RGO/PANI	2	1 M H2SO4	~385 F/g @ 0.5 A/g	5000 @ 5 A/g	88%	[14]
11	HCS-PANI-74	2	2 M H_2SO_4	~467 F/g @ 0.1 A/g	1000 @1 A/g	73%	[23]
12	MSG/PANI-4h	2	10 wt% PVA-H_2SO_4	~120 F/g @ 1 A/g	5000 @ 10 A/g	90%	[24]
13	rGO/PANI	2	10 wt% PVA-H_2SO_4	~424 F/g @ 0.5 A/g	2000 @ 7 mA/cm^2	80%	[25]

5.5. References

(1) Li, D.; Huang, J.; Kaner, R. B. Polyaniline Nanofibers: A Unique Polymer Nanostructure for Versatile Applications. *Acc. Chem. Res.* **2008**, *42*, 135-145.

(2) Heeger, A. J. Semiconducting and Metallic Polymers: The Fourth Generation of Polymeric Materials (Nobel Lecture). *Angew. Chem. Inter. Ed.* **2001**, *40*, 2591-2611.

(3) Ćirić-Marjanović, G. Recent Advances in Polyaniline Research: Polymerization Mechanisms, Structural Aspects, Properties and Applications. *Synth. Met.* **2013**, *177*, 1-47.

(4) Chen, W.; Rakhi, R. B.; Alshareef, H. N. Morphology-Dependent Enhancement of the Pseudocapacitance of Template-Guided Tunable Polyaniline Nanostructures. *J. Phys. Chem. C* **2013**, *117*, 15009-15019.

(5) Inzelt, G. *Conducting Polymers: A New Era in Electrochemistry*. Springer Science & Business Media: 2012.

(6) Jha, P. K.; Singh, S. K.; Gatla, S.; Mathon, O.; Kurungot, S.; Ballav, N. Pb^{2+}—N Bonding Chemistry: Recycling of Polyaniline–Pb Nanocrystals Waste for Generating High-Performance Supercapacitor Electrodes. *J. Phys. Chem. C* **2016**, *120*, 911-918.

(7) Mike, J. F.; Lutkenhaus, J. L. Recent Advances in Conjugated Polymer Energy Storage. *J. Polym. Sci., Part B: Polym. Phys.* **2013**, *51*, 468-480.

(8) Li, H.; Wang, J.; Chu, Q.; Wang, Z.; Zhang, F.; Wang, S. Theoretical and Experimental Specific Capacitance of Polyaniline in Sulfuric Acid. *J. Power Sources* **2009**, *190*, 578-586.

(9) Shao, Y.; El-Kady, M. F.; Lin, C. W.; Zhu, G.; Marsh, K. L.; Hwang, J. Y.; Zhang, Q.; Li, Y.; Wang, H.; Kaner, R. B. 3d Freeze-Casting of Cellular Graphene Films for Ultrahigh-Power-Density Supercapacitors. *Adv. Mater.* **2016**, *28*, 6719-6726.

(10) Wang, G.; Zhang, L.; Zhang, J. A Review of Electrode Materials for Electrochemical Supercapacitors. *Chem. Soc. Rev.* **2012**, *41*, 797-828.

(11) Jha, P. K.; Dhara, B.; Ballav, N. Nanofibers to Nanocuboids of Polyaniline by Lead Nitrate: Hierarchical Self-Assembly with Lead Ions. *RSC Adv.* **2014**, *4*, 9851-9855.

(12) Xu, J.; Wang, K.; Zu, S.-Z.; Han, B.-H.; Wei, Z. Hierarchical Nanocomposites of Polyaniline Nanowire Arrays on Graphene Oxide Sheets with Synergistic Effect for Energy Storage. *ACS Nano* **2010**, *4*, 5019-5026.

(13) Cong, H.-P.; Ren, X.-C.; Wang, P.; Yu, S.-H. Flexible Graphene–Polyaniline Composite Paper for High-Performance Supercapacitor. *Energy Environ. Sci.* **2013**, *6*, 1185-1191.

(14) Meng, Y.; Wang, K.; Zhang, Y.; Wei, Z. Hierarchical Porous Graphene/Polyaniline Composite Film with Superior Rate Performance for Flexible Supercapacitors. *Adv. Mater.* **2013**, *25*, 6985-6990.

(15) Jha, P. K.; Singh, S. K.; Kumar, V.; Rana, S.; Kurungot, S.; Ballav, N. High-Level Supercapacitive Performance of Chemically Reduced Graphene Oxide. *Chem* **2017**, *3*, 846-860.

(16) Li, L.; Raji, A.-R. O.; Fei, H.; Yang, Y.; Samuel, E. L. G.; Tour, J. M. Nanocomposite of Polyaniline Nanorods Grown on Graphene Nanoribbons for Highly Capacitive Pseudocapacitors. *ACS Appl. Mater. Interfaces* **2013**, *5*, 6622-6627.

(17) Wu, Q.; Xu, Y.; Yao, Z.; Liu, A.; Shi, G. Supercapacitors Based on Flexible Graphene/Polyaniline Nanofiber Composite Films. *ACS Nano* **2010**, *4*, 1963-1970.

(18) Conway, B. E. *Electrochemical Supercapacitors: Scientific Fundamentals and Technological Applications*. Kluwer Academic/Plenum,: New York, USA, 1999; p p. 366.

(19) Bard, A. J., Faulkner, Larry R. *Electrochemical Methods: Fundamentals and Applications*. Wiley: New York, 1980.

(20) Xie, Y.; Liu, Y.; Zhao, Y.; Tsang, Y. H.; Lau, S. P.; Huang, H.; Chai, Y. Stretchable All-Solid-State Supercapacitor with Wavy Shaped Polyaniline/Graphene Electrode. *J. Mater. Chem. A* **2014**, *2*, 9142-9149.

(21) Hong, X.; Zhang, B.; Murphy, E.; Zou, J.; Kim, F. Three-Dimensional Reduced Graphene Oxide/Polyaniline Nanocomposite Film Prepared by Diffusion Driven Layer-by-Layer Assembly for High-Performance Supercapacitors. *J. Power Sources* **2017**, *343*, 60-66.

(22) Basnayaka, P. A.; Ram, M. K.; Stefanakos, E. K.; Kumar, A. Supercapacitors Based on Graphene–Polyaniline Derivative Nanocomposite Electrode Materials. *Electrochim. Acta* **2013**, *92*, 376-382.

(23) Lei, Z.; Chen, Z.; Zhao, X. S. Growth of Polyaniline on Hollow Carbon Spheres for Enhancing Electrocapacitance. *J. Phys. Chem. C* **2010**, *114*, 19867-19874.

(24) Zheng, X.; Yu, H.; Xing, R.; Ge, X.; Sun, H.; Li, R.; Zhang, Q. Multi-Growth Site Graphene/Polyaniline Composites with Highly Enhanced Specific Capacitance and Rate Capability for Supercapacitor Application. *Electrochim. Acta* **2018**, *260*, 504-513.

(25) Hu, R.; Zhao, J.; Zhu, G.; Zheng, J. Fabrication of Flexible Free-Standing Reduced Graphene Oxide/Polyaniline Nanocomposite Film for All Solid-State Flexible Supercapacitor. *Electrochim. Acta* **2018**, *261*, 151-159.